

Department of Earth and Environmental Sciences (DISAT)

PhD program in Chemical, Geological and Environmental Sciences  
XXXIV Cycle

Curriculum in Geological Sciences

# **GROUNDWATER-SURFACE WATER INTERACTION IN ALPINE CATCHMENT**

Perico Roberta

Registration number 735780

Supervisor: Prof. Paolo Frattini

Tutor: Prof. Giovanni Battista Crosta

Coordinator: Prof. Marco Giovanni Malusà

**ACADEMIC YEAR 2020/2021**

# Contents

Summary .....	4
---------------	---

## **Chapter 1: Introduction**

1.1. Context and motivation .....	7
1.2. Scope and Structure of the current research .....	10
1.3. References .....	12

## **Chapter 2: Hydrostratigraphic characterisation and modelling of the Valtellina floodplain**

2.1. Introduction .....	16
2.2. Geological and geomorphological setting .....	18
2.3. Climatic and Hydrological setting .....	21
2.3.1. Monitoring network.....	23
2.4. Hydro-stratigraphic reconstruction .....	29
2.4.1. Methods.....	29
2.4.1.1. Domain.....	29
2.4.1.2. Sub-Domain characterization .....	29
2.4.2. Analysis and results.....	31
2.5. Rivers characterization.....	36
2.5.1. Methods.....	36
2.5.2. Results.....	37
2.6. Steady-state Groundwater flow model .....	39
2.6.1. Methods.....	39
2.6.1.1. Numerical model: Feflow.....	39
2.6.1.2. Boundary conditions .....	40
2.6.1.3. Calibration of the Hydrogeological parameters: PEST .....	41
2.6.2. Results.....	44
2.7. Conclusion.....	48
2.8. Appendix 1 .....	49
2.9. References .....	52

### **Chapter 3: Water balance in Alpine catchments by Sentinel data**

3.1.	Introduction .....	58
3.2.	Methods.....	60
3.2.1.	Groundwater storage dynamics.....	60
3.2.2.	Evapotranspiration.....	62
3.2.3.	Snow Water Equivalent.....	64
3.3.	Analysis and Results.....	67
3.3.1.	Evapotranspiration estimation .....	67
3.3.2.	Snow water equivalent estimation .....	70
3.3.3.	Quantification of groundwater storage dynamics.....	74
3.4.	Discussion.....	76
3.4.1.	Water dynamics .....	76
3.4.2.	Evaluation of ET and SWE products.....	77
3.4.3.	Spatio-temporal resolution.....	78
3.5.	Conclusions .....	80
3.6.	References .....	81

### **Chapter 4: Groundwater-Surface Water modelling**

4.1.	Introduction .....	87
4.2.	Methods.....	89
4.2.1.	Gw-sw modelling strategy .....	89
4.2.1.1.	Climate change scenarios.....	90
4.2.2.	Hydrologic Modelling.....	90
4.2.3.	Groundwater flow Modelling.....	93
4.3.	Results and discussion .....	95
4.3.1.	Surface water .....	95
4.3.2.	Groundwater.....	99
4.3.3.	Climate Change scenarios results .....	101
4.4.	Conclusion.....	103
4.5.	Appendix 2 .....	104

### **Chapter 5: Conclusions**

4.6.	References .....	108
5.1.	Summary of main contributions .....	112
5.2.	Perspectives for future research.....	113



## Summary

The recognized evidence of global warming demands assessment of the present and future water cycle in Europe and worldwide. Recently, evidence of modified hydrological regime in the Alps under climate change has been documented. However, according to the IPCC Fifth Assessment Report, it is still necessary to deepen our understanding of the impact of climate change and land use on groundwater storage in the alpine catchment areas. A major limitation to the analysis of the surface water-groundwater interaction in alpine terrain are the difficulty of data acquisition as well as the limited presence of meteorological stations. These two factors considerably increase the uncertainty of a holistic representation of the hydrological processes and a reliable estimation of groundwater recharge.

The aim of this research work is to improve the current knowledge on the interaction between surface water and shallow aquifers and to define a method for an integrated modelling of the main components of the water cycle at the catchment scale to be used as input for groundwater modelling. The collection and use of data and methods that allow for the maximum discretisation of the heterogeneity of the elements involved is the guiding thread of this work.

The scientific approach is demonstrated for a complex case study, the Valtellina valley (northern Italy), to investigate the interaction among the components of hydrogeologic cycle and their future projections according to climate dynamics. This valley could be considered a perfect case study because it is characterized by an active system that rapidly reacts to meteorological and climatic variations. This is visible by the fluctuation of the groundwater and of the main river, Adda River, during extreme precipitation events and with snow melts during the spring/summer periods.

The thesis is divided into three main sections.

The first provides a description of hydro-stratigraphy of the Valtellina valley floodplain. This section includes the groundwater flow model in a steady state condition, developed by using FeFlow 7.2, and the relative automatic calibration process for the hydrogeologic parametrization.

The second shows the quantification of seasonal groundwater storage volume according to the residual water budget method for two hydrologic years. For the estimation of the main components (Precipitation, Evapotranspiration and Snow water equivalent), new promising satellite-based database and methods are tested.

The last one describes the transient groundwater flow model developed with dynamic boundary conditions obtained from satellite-based methods. Finally, the flow model was used to evaluate the impact on groundwater of possible climate change scenarios.

## **Keywords**

Surface water and groundwater interactions

Alpine Catchment

Numerical modelling

Remote Sensing

Discretization

# Chapter 1: Introduction

## 1.1. Context and motivation

Mountainous regions cover a quarter of the Earth's surface but, disproportionately, represent the main water resource for about 40% of the world's population, also contributing to the water availability of downstream/semi-arid areas (Kapos et al., 2000; Viviroli et al. 2020; Hayashi et al., 2020; Somers et al. 2020). Indeed, mountainous areas are characterised by a high-water potential resulting from global water cycle. Due to orographic precipitation and water stored as snow and/or ice at the high altitude, mountainous regions provide huge volumes of water to the lowland areas (Somers et al., 2020). Furthermore, due to the climatic and vegetation conditions that occur at high altitudes, evapotranspiration does not heavily influence water supply (Knowles et al., 2015).

It is well known that global warming is occurring at the global level and that, by 2050, it will lead to an increasing in temperature of 1.5°C compared to the pre-industrial era (IPCC, 2019, 2021). In mountains, it is predicted that warming will occur faster and that mountain water regimes will be dramatically altered (IPCC, 2019; Vuille et al., 2018; Barnett et al., 2005; Immerzeel et al., 2010). Several studies show that the increase in temperatures will lead to a reduction in the total area covered by snow and glaciers and, consequently, a development of vegetation. This will result in a decrease in runoff and an increase in evapotranspiration (Meixner et al., 2016; Goulden et al., 2014, Wegner et al. 2017).

In mountainous regions, the important function of groundwater storage has long been neglected due to the nature of the aquifers and the steep slopes. Instead, aquifers in mountain headwaters may have the capacity to buffer the effects of global warming on the seasonality of river flow by temporarily storing meltwater and releasing it over a long time (Liu et al., 2004; Hayashi et al. 2020). For this reason, the interaction between groundwater and the surface water in mountainous areas has become a topic of great importance in recent decades.

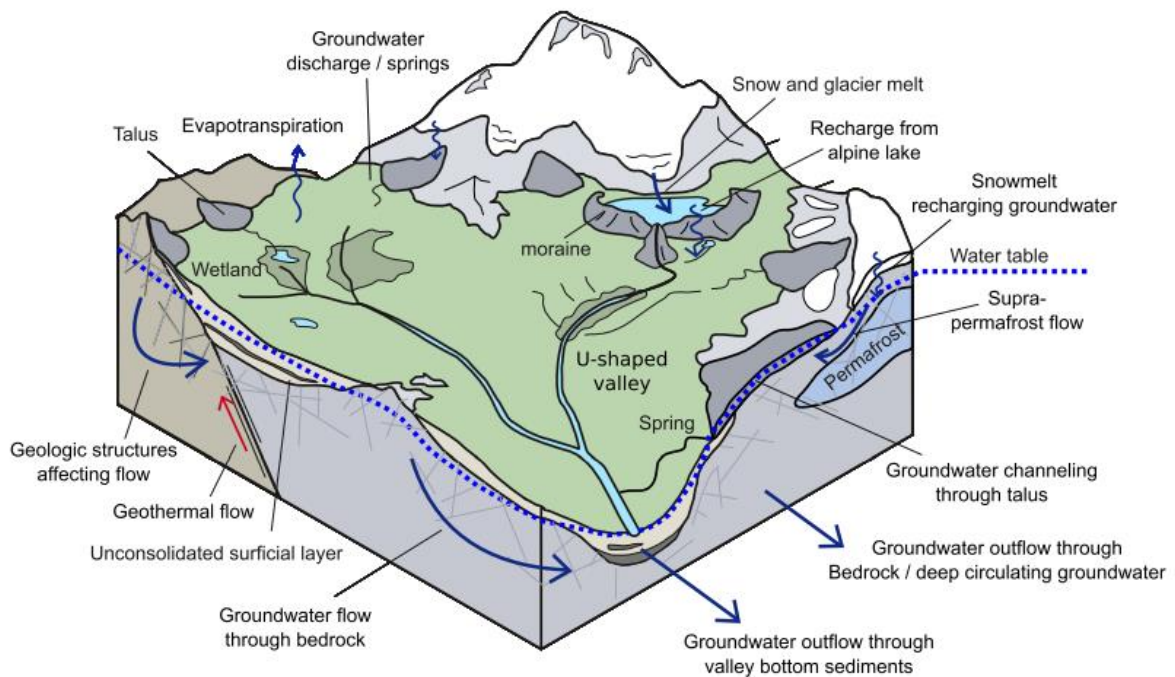


Figure 1.1: Conceptual model of high mountain hydrogeological processes including groundwater flow through subsurface features, such as talus slopes, moraines, valley bottom sediments, and bedrock, and the influence of permafrost and geological structures. from Somers et al. (2020)

The relationship between hydrological inputs and groundwater in Alpine watersheds is determined by the size of individual aquifers and the geomorphological and geological contexts (Rogger et al. 2017; Glas et al. 2018) (**Figure 1.1**). Two main categories of aquifers can be distinguished in mountain basins: rock aquifers and aquifers in unconsolidated deposits. Rock aquifers contribute to the flow of the basin's streams and central valley aquifers through fractured and weathered shallow rock or, in the case of karst aquifers, through conduits. Coarse deposits in high mountain regions include talus slopes, alluvial fans, debris fans, alluvium and some moraines (Somers et al. 2020). Apart moraines, these deposits are generally characterised by coarse materials with high permeability and porosity, such as pebbles, gravel and sand. Generally, the aquifer in coarse deposits shows a rapid recession of runoff after the recharge season (e.g., snowmelt) or rainfall events, followed by a slow recession that sustains runoff for a long period. In fact, their hydrological and sedimentological properties allow for potentially significant groundwater storage. In particular, most of the groundwater flow through the basin is channelled through alluvial aquifers at the valley floor which, at larger scales, play the role of the main reservoir. In addition, wetlands and grasslands are often identified among the geomorphic features. These

are poorly draining substrates with low permeability and high porosity. Because of their property, they are considered important for their capacity to slow down the movement of water from high to low altitudes (Mosquera et al., 2015) and attenuate high flows (Buytaert et al., 2011).

Most of the studies about the interaction between surface water and groundwater focus on the relationship between rivers and aquifers. This interaction occurs in the hyporeic zone: a type of ecotone represented by the volume of sediments, of which there is no universally accepted quantitative definition (Brunner et al.; 2017) and in which the exchange of water

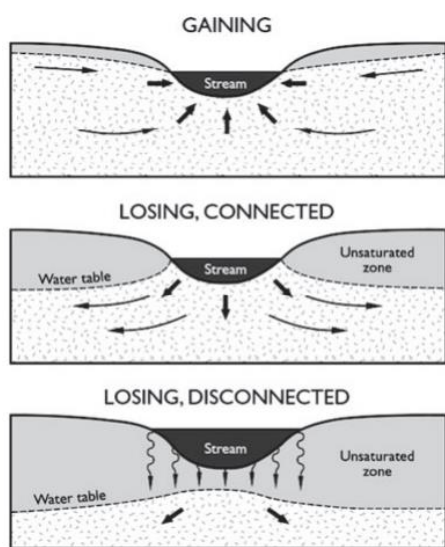


Figure 1.2: Different flow regimes between surface water and groundwater (figure based on Winter et al. 1998)

between the open channel and the water carriage occurs as a result of streambed pressure gradients and hydraulic conductivity (Tonina et al.; 2009). From a qualitative point of view, the hyporeic zone can be characterized by gaining stream, losing stream and losing-disconnected stream (Meinzer et al., 1923) (Figure 1.2). In a gaining stream, the stream drains the aquifer, while in a losing connected system water flows from the stream to the aquifer. In both cases, the flow between the stream and the groundwater remains completely saturated. In a losing-disconnected system, an unsaturated zone occurs between the river and

groundwater in which, despite a low infiltration rate, changes in the water table and river height are not directly linked (Brunner et al., 2010). However, the interaction should not be considered as permanent in time and space (Tang et al., 2019; Gleeson et al.; 2018; Winter et al.; 1999).

There are a wide variety of methods for the quantitative and qualitative analysis of the interactions between ground and surface waters. Understanding and characterising the heterogeneity of mountain systems remains a major challenge (Barthel et al., 2016, Brunner et al., 2017, Somers et al., 2020). This issue has a fundamental importance because climatic, meteorological, geological heterogeneity has a great impact in quantifying the volumes at stake for both surface and groundwater resources. However, the greatest limitation is related to data availability (Cochand et al., 2019, Candela et al. 2014; Refsgaard et al. 2010; Zhou and

Li 2011). Indeed, data for different parameters are collected heterogeneously in space and time and type of parameter (Candela et al. 2014). Moreover, in many cases, they were collected by different agencies, with different objectives and at different times and is consequently highly inconsistent (Berthel et al., 2016).

Therefore, a specific challenge facing the analysis of the Alpine region on the SW-GW interaction for this case is the collection and use of information and methods for the maximum discretisation of the problem.

## 1.2. Scope and Structure of the current research

The present work aims at analysing the interaction between surface and groundwater in large Alpine basins. The collection and use of data and methods that allow for the maximum discretisation of the heterogeneity of the elements involved is the guiding thread of this work. In particular, the focus is to implement a framework for integrated flow modelling by considering the spatial and temporal heterogeneity of each component. This has been achieved by adopting recent innovative methods able to compensate the low density of field data with good accuracy, such as: i) geostatistical and numerical inversion techniques for the development of the geological model to be used in groundwater flow modelling; ii) satellite data with high spatial and temporal resolution for the characterization of basin-scale hydrological processes. The scientific approach is demonstrated for a complex case study, the Valtellina valley (northern Italy), in order to investigate the interaction among the components of hydrogeologic cycle.

The research framework has been developed in three sections:

- The first section provides methodology for the characterisation and development of hydrostratigraphic models of valley floor aquifers in a floodplain. This section includes the geostatistical interpretation of available soft and hard data and the related process of automatic calibration of hydrological parameters. Together with the geomorphological and geological study of the area, these analyses allowed to obtain detailed conceptual models with a reasonable agreement with the water monitoring data.
- The second section shows the quantification of the seasonal groundwater storage volume according to the residual water balance method for two hydrological years.

For this purpose, recent promising methods and/or data based on satellite observations have been adopted for the main hydrological processes involved (precipitation, snow water equivalent, and evapotranspiration). In addition, the uncertainties inherent in the use of these new data at the residual water balance has been assessed.

- The last section describes a loosely coupled model that allows to couple the groundwater flow model with the hydrological model. From the results of the previous chapters, the interaction of the models occurs at a high temporal frequency and spatial resolution. The developed model was also used to simulate future projected scenarios characterized by a surface water resource reduction.

### 1.3. References

- Barnett, T. P., Adam, J. C., & Lettenmaier, D. P. (2005). Potential impacts of a warming climate on water availability in snow-dominated regions. *Nature*, 438(7066), 303-309.
- Barthel, R., & Banzhaf, S. (2016). Groundwater and surface water interaction at the regional-scale—a review with focus on regional integrated models. *Water resources management*, 30(1), 1-32.
- Brunner, P., Cook, P. G., & Simmons, C. T. (2011). Disconnected surface water and groundwater: from theory to practice. *Groundwater*, 49(4), 460-467.
- Brunner, P., Therrien, R., Renard, P., Simmons, C. T., & Franssen, H. J. H. (2017). Advances in understanding river-groundwater interactions. *Reviews of Geophysics*, 55(3), 818-854.
- Buytaert, W., Cuesta-Camacho, F., & Tobón, C. (2011). Potential impacts of climate change on the environmental services of humid tropical alpine regions. *Global Ecology and Biogeography*, 20(1), 19-33.
- Candela, L., Elorza, F. J., Tamoh, K., Jiménez-Martínez, J., & Aureli, A. (2014). Groundwater modelling with limited data sets: the Chari–Logone area (Lake Chad Basin, Chad). *Hydrological Processes*, 28(11), 3714-3727.
- Cochand, M., Christe, P., Ornstein, P., & Hunkeler, D. (2019). Groundwater storage in high alpine catchments and its contribution to streamflow. *Water Resources Research*, 55(4), 2613-2630.
- Glas, R., Lautz, L., McKenzie, J., Mark, B., Baraer, M., Chavez, D., & Maharaj, L. (2018). A review of the current state of knowledge of proglacial hydrogeology in the Cordillera Blanca, Peru. *Wiley Interdisciplinary Reviews: Water*, 5(5), e1299.
- Goulden, M. L., & Bales, R. C. (2014). Mountain runoff vulnerability to increased evapotranspiration with vegetation expansion. *Proceedings of the National Academy of Sciences*, 111(39), 14071-14075.
- Immerzeel, W. W., Van Beek, L. P., & Bierkens, M. F. (2010). Climate change will affect the Asian water towers. *science*, 328(5984), 1382-1385.
- Intergovernmental Panel on Climate Change (IPCC). (2018). Summary for policymakers. *Global Warming of 1.5C. An IPCC Special Report on the impacts of global warming of 1.5C above pre-industrial levels and related global greenhouse gas emission pathways (in the context of strengthening the global response to)*.
- Intergovernmental Panel on Climate Change (IPCC). (2019). Special Report: The Ocean and cryosphere in a changing climate (final draft). *IPCC Summary for Policymakers: Vol. TBD (Issue TBD)*. Retrieved from <https://www.ipcc.ch/srocc/>
- Intergovernmental Panel on Climate Change (IPCC). (2021).

- Kapos, V., Rhind, J., Edwards, M., Price, M. F., & Ravilious, C. (2000). Developing a map of the world's mountain forests. *Forests in sustainable mountain development: a state of knowledge report for 2000*. Task Force on Forests in Sustainable Mountain Development., 4-19.
- Knowles, J. F., Harpold, A. A., Cowie, R., Zeliff, M., Barnard, H. R., Burns, S. P., ... & Williams, M. W. (2015). The relative contributions of alpine and subalpine ecosystems to the water balance of a mountainous, headwater catchment. *Hydrological Processes*, 29(22), 4794-4808.
- Liu, F., Williams, M. W., & Caine, N. (2004). Source waters and flow paths in an alpine catchment, Colorado Front Range, United States. *Water Resources Research*, 40(9).
- Meinzer, O. E. (1923). The occurrence of ground water in the United States with a discussion of principles (Vol. 50, No. 846). University of Chicago.
- Meixner, T., Manning, A. H., Stonestrom, D. A., Allen, D. M., Ajami, H., Blasch, K. W., ... & Walvoord, M. A. (2016). Implications of projected climate change for groundwater recharge in the western United States. *Journal of Hydrology*, 534, 124-138.
- Mosquera, G. M., Lazo, P. X., Célleri, R., Wilcox, B. P., & Crespo, P. (2015). Runoff from tropical alpine grasslands increases with areal extent of wetlands. *Catena*, 125, 120-128.
- Refsgaard, J. C., Storm, B., & Clausen, T. (2010). Système Hydrologique Européen (SHE): review and perspectives after 30 years development in distributed physically-based hydrological modelling. *Hydrology Research*, 41(5), 355.
- Rogger, M., Chirico, G. B., Hausmann, H., Krainer, K., Brückl, E., Stadler, P., & Blöschl, G. (2017). Impact of mountain permafrost on flow path and runoff response in a high alpine catchment. *Water Resources Research*, 53(2), 1288-1308.
- Somers, L. D., & McKenzie, J. M. (2020). A review of groundwater in high mountain environments. *Wiley Interdisciplinary Reviews: Water*, 7(6), e1475.
- Tang, Q., Schilling, O. S., Kurtz, W., Brunner, P., Vereecken, H., & Hendricks Franssen, H. J. (2018). Simulating Flood-Induced Riverbed Transience Using Unmanned Aerial Vehicles, Physically Based Hydrological Modeling, and the Ensemble Kalman Filter. *Water resources research*, 54(11), 9342-9363.
- Tonina, D., & Buffington, J. M. (2009). Hyporheic exchange in mountain rivers I: Mechanics and environmental effects. *Geography Compass*, 3(3), 1063-1086.
- Viviroli, D., Kummu, M., Meybeck, M., Kallio, M., & Wada, Y. (2020). Increasing dependence of lowland populations on mountain water resources. *Nature Sustainability*, 3(11), 917-928.
- Vuille, M., Carey, M., Huggel, C., Buytaert, W., Rabatel, A., Jacobsen, D., ... & Sicart, J. E. (2018). Rapid decline of snow and ice in the tropical Andes—Impacts, uncertainties and challenges ahead. *Earth-Science Reviews*, 176, 195-213.
- Wagner, T., Themeßl, M., Schüppel, A., Gobiet, A., Stigler, H., & Birk, S. (2017). Impacts of climate change on stream flow and hydro power generation in the Alpine region. *Environmental Earth Sciences*, 76(1), 1-22.

Winter, T. C. (1999). Ground water and surface water: a single resource (Vol. 1139). Diane Publishing.

Zhou, Y., & Li, W. (2011). A review of regional groundwater flow modeling. *Geoscience frontiers*, 2(2), 205-214.

Zipper, S. C., Dallemagne, T., Gleeson, T., Boerman, T. C., & Hartmann, A. (2018). Groundwater pumping impacts on real stream networks: Testing the performance of simple management tools. *Water Resources Research*, 54(8), 5471-5486.

# Chapter 2:

## Hydrostratigraphic characterisation and modelling of the Valtellina floodplain

## 2.1. Introduction

Mountain areas play a key role in the global water supply, as they are the place of greatest input to the water balance (Somers et al., 2020). In these environments, generally, the primary focus of studies is on surface resources, such as snow or rivers. Climate change is having a strong impact on these resources in northern environments (Cochand et al., 2020) and groundwater is becoming a potential primary water supply resource. However, the relationship between surface water (SW) and groundwater (GW) is very close, especially for unconfined surface aquifers such as valley floors. Therefore, it is necessary to deepen the knowledge of groundwater vulnerability (Singleton and Moran, 2010).

The realistic characterisation of the aquifer geometry pattern represents a fundamental point for the management of the groundwater resources (De Carvalho et al., 2017; Strebelle, 2002). In particular, it is widely accepted that it is necessary to consider the valley floor aquifers as a set of highly heterogeneous sedimentary bodies that act as storage reservoirs and/or conduits for groundwater (Comunian et al., 2011; Martin et al., 2020, Somers et al., 2020; Tang et al. 2019). In particular, in mountainous regions, the variety of alluvial and glacial depositional processes lead to a very complex surface stratigraphy (Cairns, 2014). However, due to the complexity of characterising the heterogeneity of bodies, these environments are often simplified or neglected (Dochartaigh et al., 2019).

Several previous studies have shown different methods for geometry characterisation and hydraulic parameterization. For example, Bayer (2011) and Comunian (2011) reconstructed the 3D internal heterogeneity of each sedimentological structure in the fluvio-glacial valley of the Rhine River. They applied multiple point statistics with a simple conceptual model, obtained from field activities, as a training image. In addition, several multidisciplinary approaches were presented: Dochartaigh (2019) reconstructed the 3D geological model of the Eddleston Water catchment in Scotland (UK). Through the combination of geophysical data (EM, GPR, and ERT), well data and hydrogeological data, alluvial, fluvio-glacial, and low-permeability lens deposits were differentiated. Likewise, Martin (2020) combined geological, geophysical, and geochemical techniques to identify Quaternary and Holocene aquifers separated by low-permeability clays in the Ammer floodplain (southwest Germany).

In the present work, the Valtellina valley floor was selected as a case study for the characterisation of an extensive valley floor aquifer. Here, limited information is reported in the literature on groundwater systems and their seasonal fluctuations or historical trends. In fact, the water supply in Valtellina has always been mostly based on the surface spring water sources. However, due to the impact of climate change and increased water exploitation, surface water will not be able to fully supply the demand and it is therefore necessary to increasingly focus on groundwater resources. After a detailed geological, geomorphological, and climatic setting and the collection of hydrological data of the area, the geometries and hydrogeological parameters of the aquifer were carried out. As illustrated in **Figure 2.1**, a workflow to obtain a tool for GW-SW resource modelling is described in this paper. It involves two main steps: I) the hydro-stratigraphic reconstruction and parametrization; II) the calibration of the hydraulic parameters honouring the field observations.

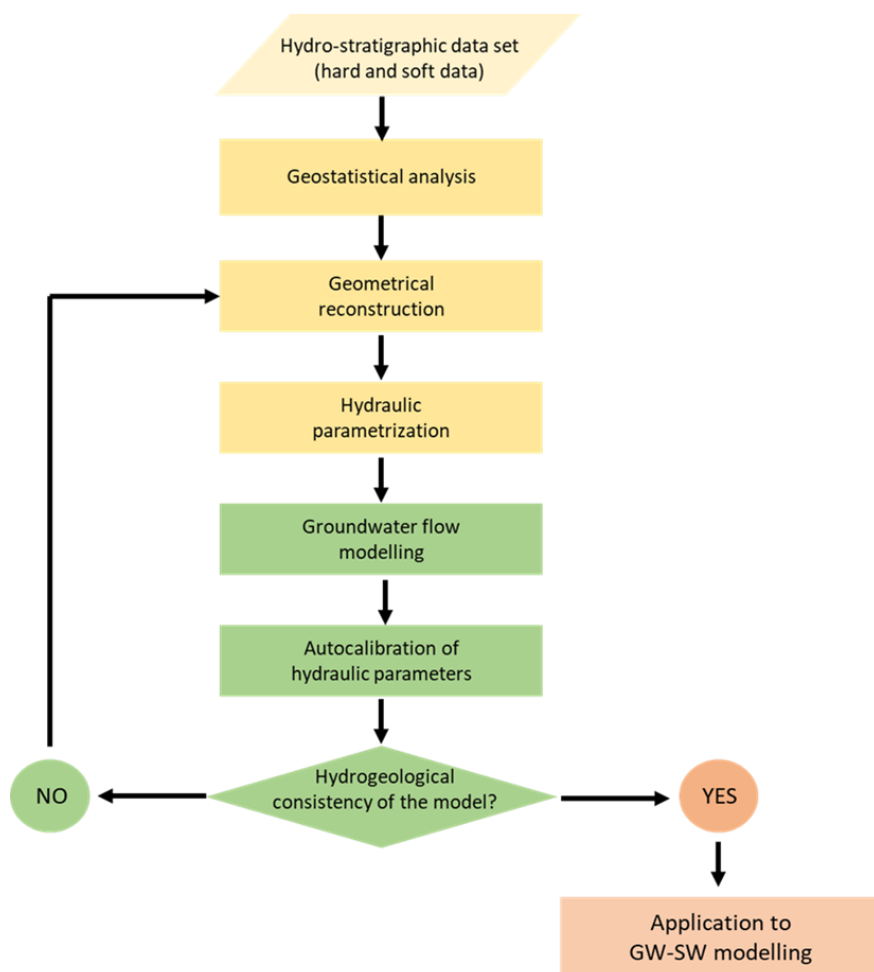


Figure 2.1: The workflow proposed in the present work. It combines hydro-stratigraphic data interpretation and parametrization with mathematical modelling to obtain a tool for the study of the GW-SW interaction.

## 2.2. Geological and geomorphological setting

The study was conducted in the alpine catchment of Valtellina Valley, Italy, between longitude 46° 08'00E and 46° 29'00E, and latitude 9° 31' 00N and 10° 22'00N, Errore. L'origine riferimento non è stata trovata..

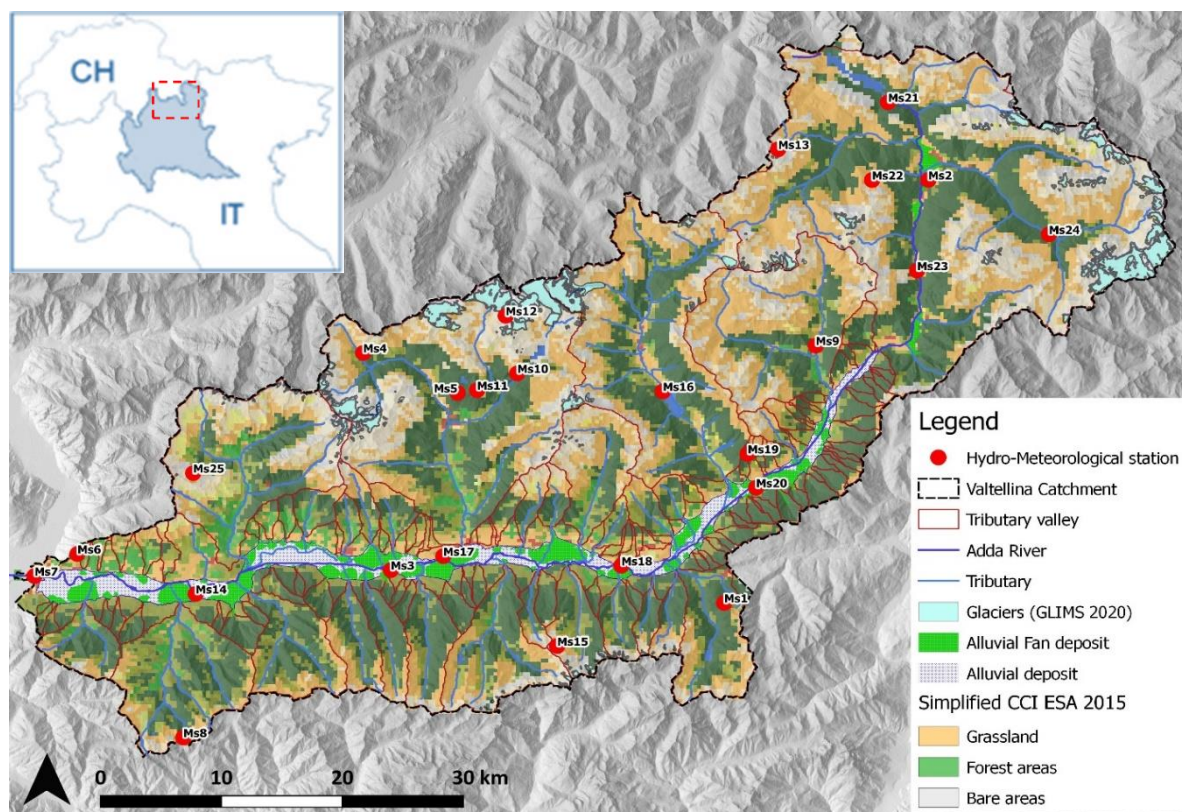


Figure 2.2: Overview of the study area.

Valtellina valley stretches along the Adda River that flows to the Lake Como through a flat alluvial plain. The valley covers 2,600 km<sup>2</sup> and is characterized by high peaks (up to 4000 m a.s.l.), high local relief and relatively steep topography, all progressively decreasing moving towards the south (Agliardi et al. 2013; Crippa et al. 2021). The area is mostly characterized by grassland on the valley floor and broad-leaved/coniferous forest and bare rocks on the slopes. Considerable glacial areas (5 % of the total catchment) are located in three lateral valleys (Val Masino, Valmalenco and Valfurva valleys). The last available survey of glaciers by photointerpretation is from 2017, produced by DST UNIMI (Laboratorio Fotogeologia) and accessible through the Global Land Ice Measurements from Space in 2020 (GLIMS) database. The sources of the Adda river are located near the Alpisella pass (2.285 m). The hydrographic network includes several tributaries, including some of relatively large size, such as Frodolfo

(24 km long), Poschiavino (27 km long), Mallero (27 km long), Masino (22 km long) and Tartano (22 km long).

Valtellina is an east-west-trending valley superimposed on the Insubric Line (named Tonale Line in Valtellina), a steep E-W trending fault zone active during Oligo-Miocene (Schmid 2017) that separates the N-verging Austroalpine and Penninic units from the S-verging Southalpine units (**Figure 2.3**). Penninic units include oceanic lithosphere remnants and outcrop in the Valmalenco valley. Overlying Austroalpine units mainly consist of continental lithosphere of the Apulian margin, including metamorphic basement, intrusives and Mesozoic sedimentary successions (Florineth and Froitzheim 1994; Schmid 2017). They extend from Valmalenco to

the eastern part of Valtellina and they are intruded by a major Tertiary tonalitic and granodioritic bodies outcropping in Val Masino (Masino-Bregaglia). Southalpine units, south of the Insubric Line, form a fold-and-thrust belt made, from N to S, of a Variscan metamorphic basement, Permian volcanoclastic and sedimentary successions and Mesozoic sedimentary

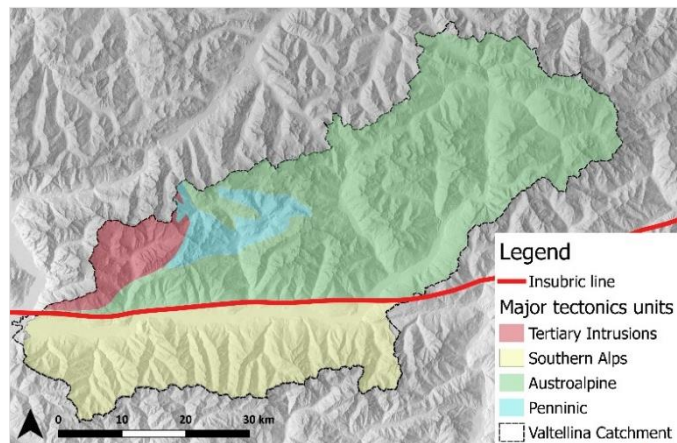


Figure 2.3: Tectonic scheme of the study area.

succession including carbonate and terrigenous rocks (Schmid, 2017). These rocks are expected to form the seismic bedrock of the inferred Adda buried valley.

The floodplain is mainly filled with continental fluvial and fluvio-glacial deposits, accumulated since the late Pliocene (Cavallin et al. 1997). During the Last Glacial Maximum (LGM; Ivy-Ochs et al. 2008; Grämiger et al. 2017), a thick ice sheet covered the Alpine axial sector with ice thickness reaching 2800 m a.s.l. (Bini et al. 2009), feeding important valley glaciers that carved out the topography defining a U-shaped profile for the Valtellina valley. De Franco et al. 2009 and Mele et al. 2021 reported the reconstruction of the basement geometry along two sections (**Figure 2.4**). In the first study, the limit between the sedimentary sequence and the bedrock was reconstructed from the seismic reflection profile obtained at the Teglio site, in the eastern part of Valtellina, and calibrated with a lithological borehole log down to 200 m b.g.s. At the Teglio site, the upper limit of the bedrock confirms a U-shape and shows a

thickness of 200-250 m at flanks of the valley and of 550 m along the axis of the valley (**Figure 2.4c**). Mele et al. 2021 applied the Horizontal-to-Vertical Spectral Ratio (HVSr) passive seismic technique to define the base of the Adda sedimentary deposits at the Fuentes site, in the western margin of Valtellina. The interpretation of the collected data was performed considering the velocity obtained at the analogous Teglio site by De Franco et al. 2009, local borehole logs, and surface geological and geomorphological constraints. At the Fuentes site, the bedrock is overlain by indistinct low-velocity sedimentary sequences approximately 300 m thick (**Figure 2.4b**).

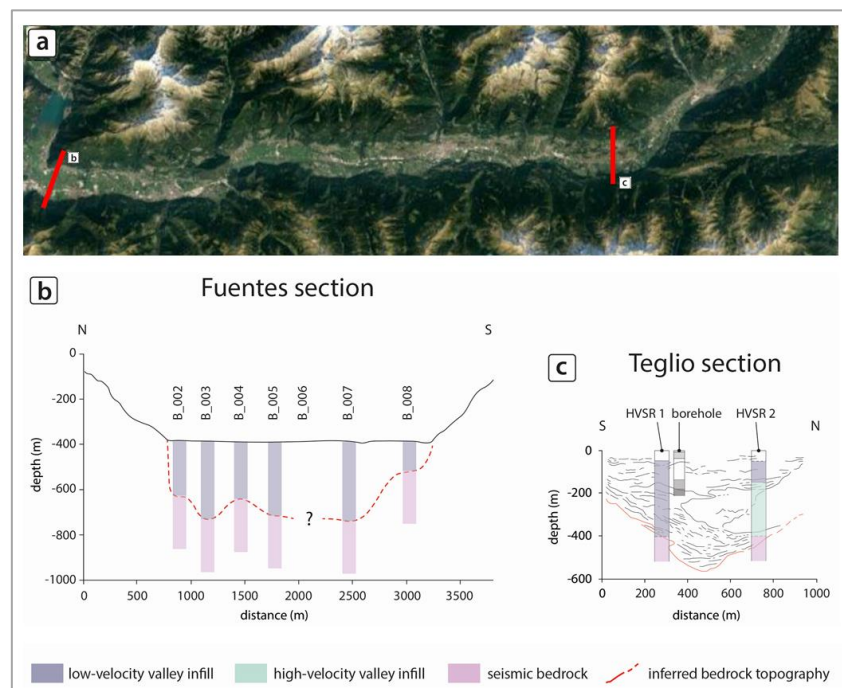


Figure 2.4: 2D sections of the Fuentes (b) and Teglio (c) sites modified from Mele et al. (2021) and De Franco et al. (2009) and their location in the valley floor (a). The red line delimits the boundary between the seismic bedrock and the fill deposits.

The Post-LGM deglaciation caused major stress and hydrological perturbations that triggered paraglacial slope response and progressive failure (Grämiger et al. 2017; Riva et al. 2018, Spreafico et al. 2020). These activities, still active in some cases, contributed to the formation of alluvial fans in Valtellina (Ryder, 1971; Crosta et al., 2004; De Finis et al., 2017) (**Figure 2.1**). According to Crosta et al. (2004), Jarman et al. (2011), and De Finis et al. (2018), alluvial fans can be grouped into two groups based on the dominant primary processes and the resultant composite fan morphology through the analysis of the surface fan morphology, sedimentary deposits, and the historical documentation of flood events. The first group includes the allometric fans, built incrementally through depositional processes and showing a size

remarkably proportionate to the area of their basin. In particular, among these fans we distinguish type-I, derived from fluvial processes (e.g., sheet-floods), and type-II, connected to sediment-gravity (e.g., rock falls, debris flows) flow. The second group is formed by anomalous fans, characterised by an excessive volume with respect to conventional incremental processes, with a genesis that can be attributed to one or more catastrophic events. The anomalous fans strongly affect the stratigraphy of the floodplain because they act often as landslides dams, causing silting processes in the lake-basins upstream the fans. Unfortunately, the high degree of urbanization and the limited availability of information on actual geometry and lithotextures make it challenging to characterize some of these quaternary deposits (De Finis et al., 2017). However, in agreement with the classification of Crosta et al. (2004), Valtellina presents mainly fans of the first group with fluvial genesis, such as the Sondrio and Morbegno fans and others linked to debris-flow events, such as Tartano and Postalesio fans. Moreover, some extensive anomalous fans, such as Sernio, Rhon, and Migiondo fans, are detected along the floodplain (Crosta et al., 2004; De Finis et al., 2014).

### 2.3. Climatic and Hydrological setting

Due to the wide range of altitude and slope aspect, a strong climatic variability with seasonal thermal contrasts characterizes the Valtellina Valley. Generally, the climate of the area is continental Alpine, with cold winter and moderate summer and the seasonal snow cover starting from 1000 m a.s.l. (e.g., Bocchiola and Rosso, 2007; Bocchiola et al., 2010; Bocchiola and Groppelli, 2010, Alii et al., 2019). However, according to the Köppen–Geiger scheme (e.g., Peel et al., 2007; Beck et al., 2018), the valley floor presents a warm temperate climate (Cfa) with hot summers and no dry season on the floodplain, and, on the slopes, a climate classified as a tundra climate (ET) or as fully-humid snow climate (Dfa-Dfb), based on the timber line (**Figure 2.5**).

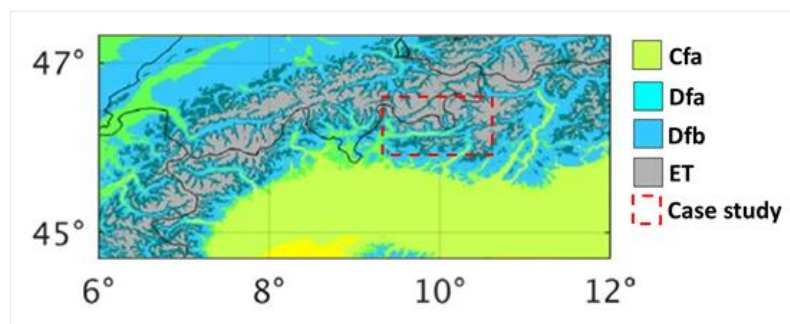


Figure 2.5: Köppen-Geiger classifications maps for the case study in the European Alps. (Modified by Beck, (2018))

Moreover, considering the high spatial variability in terms of total annual values and seasonal distribution of precipitation (rainfall and snowfall) the area could be partitioned in three sub-regions (Ceriani and Carelli, 2000; Scotti et al., 2014). In the northernmost mountain range, annual precipitation ranges locally from 790 to 1200 mm, with a winter minimum in February and a single summer maximum in August. In the southernmost mountain range two precipitation peaks in June and October and a higher annual precipitation value, ranging from 1620 to 1770mm, can be observed. Furthermore, the temperatures in this sub-region are strongly influenced by the northern exposure of the slopes, leading to less sunlight especially during the autumn-winter period. Finally, the central-northern area, located at an intermediate latitude, exhibits a seasonal distribution of the precipitation similar to that of the southern area, but with a lower total annual value, in a range of 1210–1370 mm.

Like in other large alpine valleys, the groundwater flow in the floodplain is characterized by a relatively shallow system, in which an active circulation and a rapid response to changes in discharge and recharge are observed. At the highest altitudes, the resource is mainly superficial, characterised by diffuse springs and streams fed by runoff. At the catchment scale, the recharge is mostly controlled by spring snowmelt and by rainfall in early fall.

Moreover, the system is highly influenced by the large hydropower production in the twenty-seven hydropower dams (from the biggest plants, such as Cancano, Alpe Gera and San Giacomo di Fraele, to the smallest ones, such as Ganda and Moledana) (D'Agata et al., 2018). In fact, these large artificial reservoirs act as water reserves that are exploited to partially compensate the summer periods of water shortage in the valleys, and as regulators of floods, with a significant effect for the main river.

Recently, several studies, such as Beck et al. (2018) and Rubel et al. (2017), are showing that in the European Alps global warming is increasingly influencing the climate and hydrologic pattern. The rising of the temperature and the high frequency of large-scale heavy precipitation and related floods are moving in 2076–2100 in warmer climatic classes, forcing into small areas the typical Alpine climate (ET) in the best-case scenario of the projections. This is confirmed by the data recorded in the last years and in the projected based on the CMIP5 models (Rubel et al., 2017).

### 2.3.1. Monitoring network

In the last ten years, meteorological and hydrological datasets have been collected continuously and made available online by the Environmental Protection Agency of Lombardia Region (ARPA-Lombardia) but some large areas, inevitably, remain unmonitored. In Appendix 1, the database characteristics for the present study is illustrated.

The meteorological data collected in the whole catchments consists of 24 pluviometric stations: 16 are located in mountain areas and also record snow thickness and 8 are located in the valley floor. In the Arpa database, observations of evapotranspiration measured in a direct way (e.g., by lysimeters, evaporimeters or eddy covariance stations) are not available. However, potential evapotranspiration was derived indirectly with the Penman – Monteith equation (Allen, et al., 1998), thanks to the data of temperature, wind speed, humidity and global radiation data collected in 6 meteorological stations (Ms02, Ms03, Ms14, Ms17, Ms20, Ms22). For the estimation at the catchment scale, these data were analysed by the CROPWAT 8.0 software for each meteorological station during the hydrological year. Then, the estimated values were interpolated with deterministic method on the whole area. Moreover, the evapotranspiration maps were adjusted according to crop type (coefficient K). For the definition of the K, the land use and land cover map, from the DUSAF (agricultural and forest land use) geographical database (2018), was considered.

Regarding the water resource, the surface water and the groundwater are monitored in different way. The river stage is recorded continuously at 4 hydro-meteorological stations located along the Adda river. For 3 of these points, the Adda consortium provides discharge data, through the discharge scaling method, for which a biunivocal empirical relationship is defined between discharge and stream stage, as the result of a statistically sufficient number of measurements. The spatial and temporal frequency of measurement of the Adda River enables the identification of inter-annual and daily variation. For the tributary valley, the data of stream stage and discharge are available only for the Swiss Poschiavo valley (Poschiavino river Ms16, <https://www.hydrodaten.admin.ch/it/2078.html>). Along the flood plain, the groundwater level is monthly monitored by Arpa in 12 locations, with hourly data in 2 of them. Moreover, 8 pressure sensors have been installed by the integrated water service of Sondrio (SECAM Spa) since 2016, at wells designated for drinking water use.

As regards the monitoring network, starting from the analysis of the time series of meteorological and hydrological parameters, three main recharge phases of the hydrologic

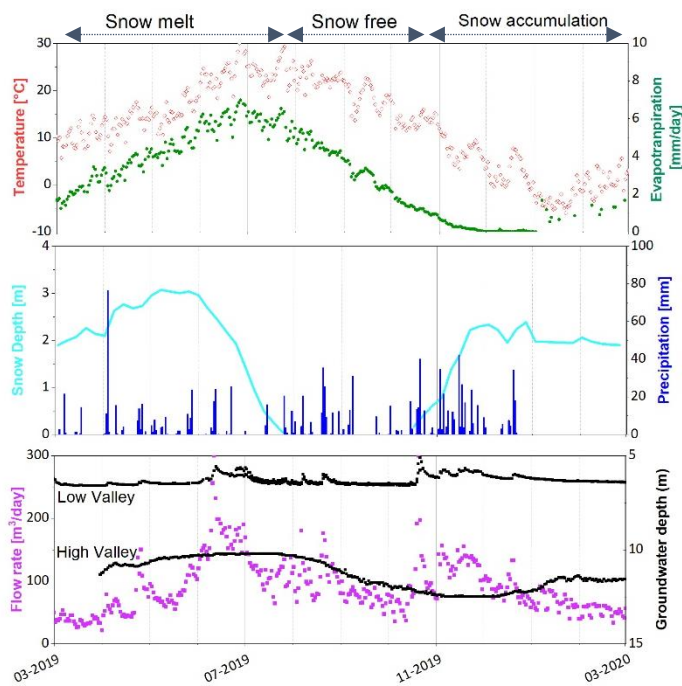


Figure 2.6: Time series of meteorological and hydrological parameters during a hydrologic year (March 2019-March 2020). The time series of the groundwater level (black) show a fluctuation directly linked to the surface water components during the three phases of the year.

year were identified (Figure 2.6). The first rising phase of the hydrograph occurs from the beginning of March to the end of July and is mainly driven by the snowmelt process. In fact, the snow cover usually disappears completely in the entire catchment by the beginning of August. Connected to this period, elevated discharge in the main rivers and an increase in the groundwater level can be observed. During the snow-free period, the recession of the hydrograph is characterized by sporadic and instantaneous peaks of discharge and groundwater level due

to heavy rainfall events until the end of November. With the beginning of the snow accumulation, the recession extends up until February with a minimal discharge of  $50 \text{ m}^3/\text{day}$  at the closing point of the catchment.

In order to improve the data about the inter-annual and intra-annual trend of the Valtellina aquifer and of the Adda River, a monitoring network has been set up by the group of Milano Bicocca University. During May 2019, an inspection was carried out with the purpose of verifying well characteristics, such as the coordinates, the depth, the accessibility, and the available in the database of Province. 18 points have been selected along the Adda River to measure the stream stage of the Adda during the monitoring campaign. A topographic survey on these points was carried out with rapid-static method in RTK mode, using post-processing bases on the network of fixed stations of the GNSS Inter-regional Positioning Service of Piedmont and Lombardy. A GW monitoring network of 54 wells located on the valley floor (from Lovero to Fuentes, Figure 2.8) and owned by private industries and citizens or by the

integrated water service of Sondrio (SECAM Spa) has been set up. The network was monitored with quarterly monitoring campaigns and with continuous data acquisition by 13 pressure sensors installed by University of Milano Bicocca, ARPA and SECAM Spa. Three monitoring campaigns were carried out in June 2019, October 2019, and January 2020. Due to the sanitary situation, the fourth monitoring campaign of the hydrological years, planned for April 2020, could not be carried out. However, the continuous data was collected for the following two years. The piezometric maps obtained from the monitoring campaigns are shown in the **Figure 2.8**. A NE-SW direction of the flow with a hydraulic gradient of 0.01 was detected, with hydraulic head values ranging from 500 to 200 m a.s.l. and a fluctuation in values of 2 m. Moreover, a gradient increase (0.015) was observed at three geomorphological points of interest: the Sernio alluvial fan, the Rhon alluvial fan and the Talamona alluvial fan (**Figure 2.7**).

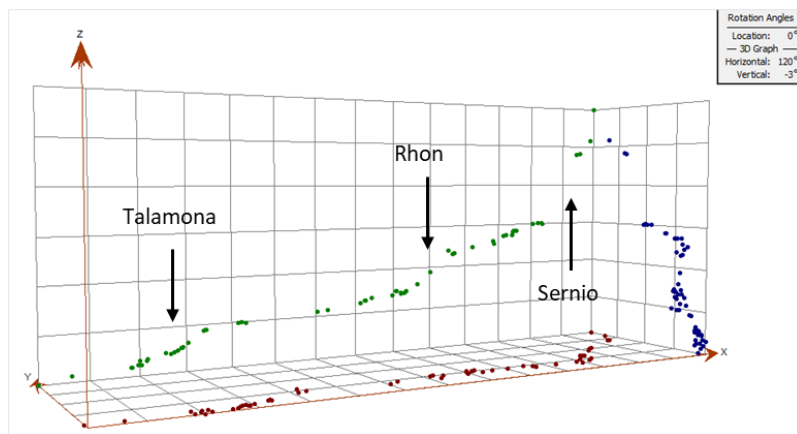


Figure 2.7: Trend analysis of piezometric data along the valley floor in the E-W direction (green dots) and in the N-S direction (blue dots). The figure shows the locations where a change in the hydraulic gradient occurs.

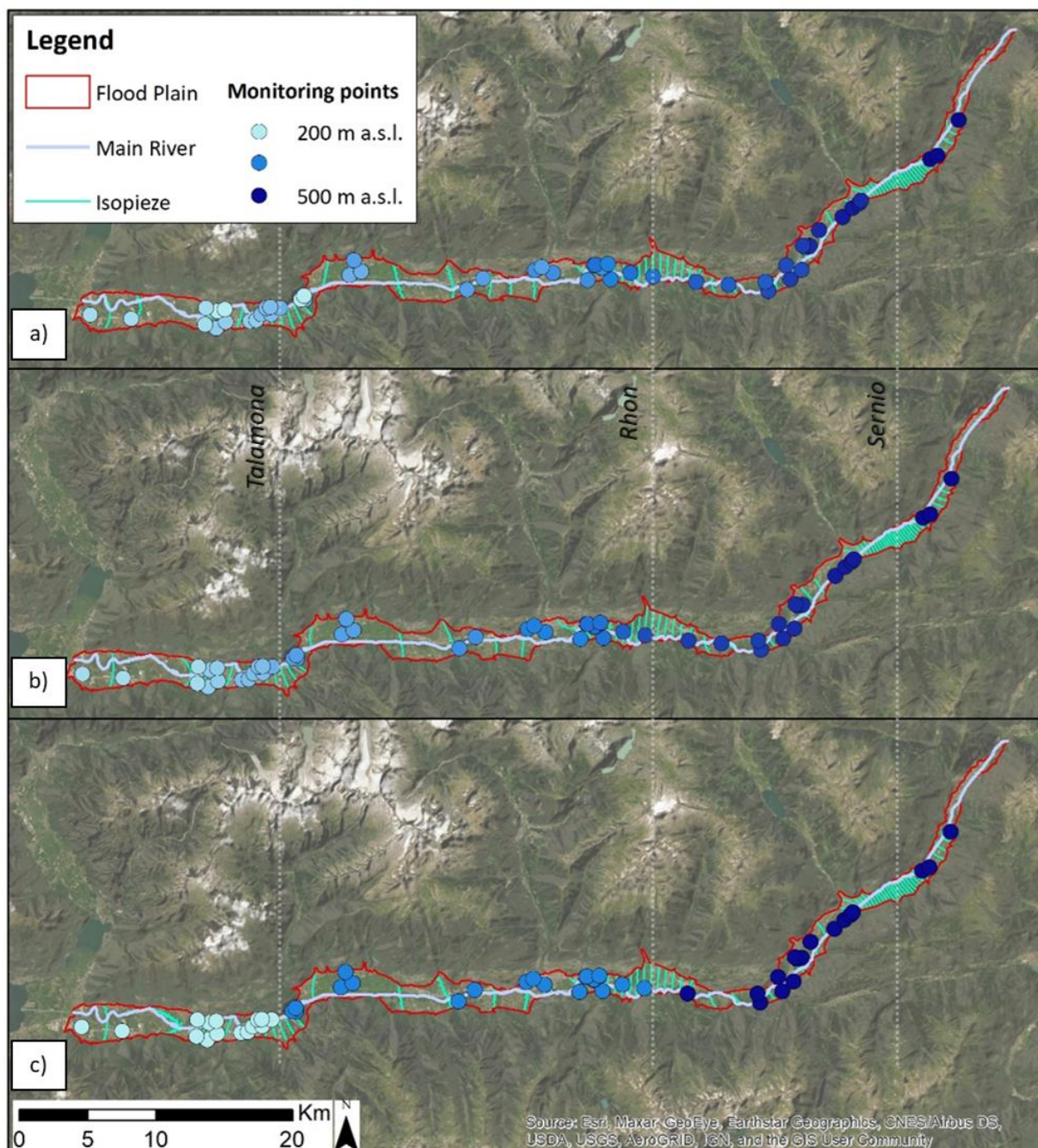


Figure 2.8: Piezometric maps obtained from data collected in the groundwater-monitoring network (dots) during the three monitoring campaigns in June 2019 (a), October 2019 (b), and January 2020 (c). The dashed grey lines indicate the 3 locations with a variation in hydraulic gradient.

As can be observed from the continuous data (**Figure 2.6**), the June campaign corresponds to the top of the aquifer recharge phase, the October campaign to the days before the autumn rainy period, while the January campaign to the recession phase. However, even if the dominant trend is characterised by a minimum value of the groundwater level in October, it is not possible to distinguish a homogeneous seasonal trend along the whole valley floor. In particular, a subset of piezometers, located upstream of the valley floor and at the outlets of

the main tributary valleys, show a different behaviour. Here, the minimum value of the water table was recorded in June. In fact, the first campaign coincides with the beginning of the recharging phase resulting from the melting of the last snow at high altitude and is therefore later than the other areas. In addition, thanks to the continuous data collected in the area further downstream, it was possible to observe that the connection between the main river and the water table is very close up to a maximum distance of 500 m from the Adda. In fact, a delay minor of 24 hours between the peaks of the hydrograms and groundwater head is recorded.

Finally, samples of groundwater and surface water have been collected during the fieldwork activities for the characterization of the physiochemical parameters and the definition of the solutes constituents. During each monitoring campaign, the sampling points were selected according to the location, the well structure, and consent of the owners. The physiochemical characteristics (Ph [-], temperature [°C], and electrical conductivity [ $\mu\text{S}/\text{cm}$ ]) were detected during the fieldwork by a multiparameter instrument. Sampling was carried out using clean 250 ml jars, which were then stored in a refrigerator until analysis, which took place in the laboratory of the Department of Environmental and Earth Sciences at the Milano-Bicocca University.

The alkalinity of the water and therefore the concentration of bicarbonates was determined by manual titration, while the concentrations of the main cations (Lithium, Sodium, Potassium, Magnesium, Calcium) and anions (Fluorides, Chlorides, Nitrates, Sulphates) were determined by ion exchange chromatography (Metrohm 883 Basic IC Plus chromatograph). During the three campaigns, a homogeneous pH value of 8 was recorded over the whole valley floor. Regarding the temperature, a slight trend can be detected during the year: in June and October, a spatially homogeneous temperature (10-15°C) was recorded, with an increase of the average temperature of about 1°C between the first and the second campaign, due to the summer heat storage. During the January campaign, a temperature gradient between surface water (3°C) and groundwater (11°C) can be distinguished. The electrical conductivity (EC) and the total alkalinity (Talk) values show a spatial variability. In the lower part of the valley, the surface water and the groundwater have a reduced geochemical dominance (with about 100  $\mu\text{S}/\text{cm}$  of EC and % of Talk), as they are strongly dependent on rainfall and snowfall. Whereas, in the upper part, the sampled groundwater shows a strong

geochemical dominance with values of about 250  $\mu\text{S}/\text{cm}$  of EC and  $^\circ\text{f}$  of Talk. However, from the analysis of the major constituents, all samples show a calcium-bicarbonate composition, as can be seen from the piper diagram in **Figure 2.9**. This composition is due to the dissolution of minerals from the deposits belonging to the Southalpine sedimentary series.

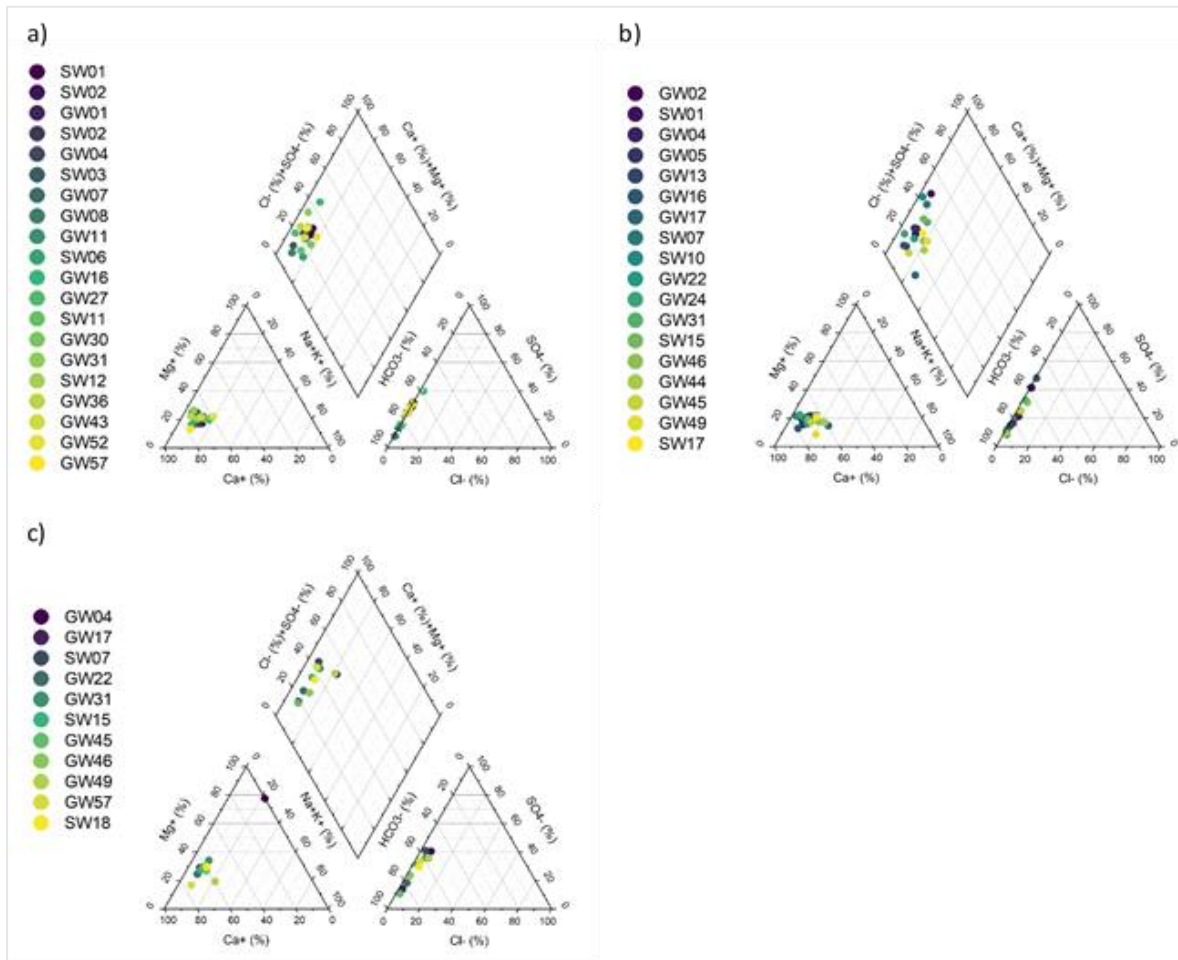


Figure 2.9: Piper diagram of samples collected during the monitoring campaign of June 2019 (a), October 2019 (b), and January 2020 (c). The samples are plotted with a colour scale ranging from blue in the upper valley to yellow in the lower valley.

## 2.4. Hydro-stratigraphic reconstruction

### 2.4.1. Methods

#### 2.4.1.1. Domain

The study domain was defined starting from the geomorphological information. For this phase of the analysis, the geomorphological map and the DTM of the Lombardy Region was used. The first map is the product of field surveys and photo-interpretative analysis for the definition of geomorphological processes, shapes and deposits. The second is a digital elevation model with 5 m resolution and an accuracy from 0.30 m in urban areas to 2 m in forest areas.

The superficial limit of the domain corresponds to the extent of alluvial deposits and alluvial fan deposits, corrected considering the altitude gradient along the contact between the valley floor and the slopes. Considering the bedrock detected by De Franco et al. (2009) and Mele et al. (2021), the lower surface of the modelling domain was derived through an extrapolation of the DTM underground. In particular, the northern and southern slopes were linearly extrapolated up to their junction below the fluvio-glacial deposits. This reconstruction was carried out for 46 cross-sections perpendicular to the axis of the valley by using the Move2017.2 software. Subsequently, the bedrock surface was obtained by interpolation with the Delaunay triangulation method.

#### 2.4.1.2. Sub-Domain characterization

The entire domain was internally subdivided by the analysis of hard and soft data. As for most hydrogeological modelling studies, field and subsurface data represent the starting point, but the scarcity and poor spatial distribution of data required the use of initial assumptions based on literature values.

##### 2.4.1.2.1. *Soft data: the Toglio seismic section*

The soft data consist of the Toglio seismic section. The acquisition was made in 2000 in the framework of the CARG (Geological CARTography) project for the new geological map of Italy. In particular, for the Toglio section, data were acquired using both reflection and refraction seismic methods (De Franco et al., 2009).

The seismic survey allows the representation of the subsurface using refracted or reflected waves produced by a controlled source and recorded at the surface by receivers. In general, reflection seismic allows detail down to considerable depths, while refraction is limited to the

upper part of the subsurface. Each type of material is characterised by a range of velocities, as follow:

$$V_1 = x/t \quad (2.01)$$

Where  $x$  is the position of each receiver and  $t$  is the time of the first arrival, and  $V$  is the slope of the dromochrone curve.

The reflection seismic data were acquired by using the standard roll-along procedure, with a sampling rate of 1 ms and record length of 1024 ms. With a 48-channel digital system, the receiver group spacing was 5 m and a group of two geophones with 30 Hz frequency was used. Instead, the reflection profile was acquired with a 24-channel digital system with 25 m geophone spacing.

The reprocessing of the data was carried out in collaboration with the applied geophysics laboratory of the Institute of Environmental Geology and Geoengineering (IGAG) of the National Research Council (CNR).

For each acquisition, the first arrivals were manually detected from the raw data. Subsequently, by applying a seismic refraction inversion technique in addition to the standard reflection processing, a high-resolution velocity model was produced and interpreted for the surface deposits.

#### 2.4.1.2.2. *Hard data: borehole logs*

The hard data consists of: I) 274 logs from the database of the Province of Sondrio, Natural Resources and Spatial Planning Sector Water and Energy Service (Province of Sondrio, 2018); II) 57 logs from the national archive of subsurface investigations, created by the Department for the Geological Survey of Italy - ISPRA. The depth of these logs ranges from 2 m to 208 m.

Within the stratigraphic database, each borehole log has been associated with a unique code and location information (coordinates in the WGS84 reference system, height, depth, and municipality). In addition, for each survey, the height of the top and bottom of the layers and their composition are reported. Where this information refers to an equipped well, the depth and thickness of the filter and the use of the well are also reported.

For the management of the stratigraphic information, the description of the layers of each borehole log was simplified in accordance with De Caro et al. 2020 and Bayer et al. 2011. An alphanumeric code was adopted representing abbreviations for lithofacies (G for gravel, S for

sand, F for silt/clay) in order to allow the identification of major sedimentary sequences. In particular, the lithological descriptions were codified considering only the main grain size and the subordinate components. The prevailing texture was deduced from the extended description according to the CNR-UNI and AGI method. The hydrologic parameter of the lithofacies was derived from hard-data measurements (e.g., pumping test and recovery data) in the zone or interpretation based on hydrogeological knowledge and literature values (Bayer et al., 2011, 2015; De Caro et al. 2020; Heinz et al.,2003; Previati et al., 2020). In practice, an ASCII file was generated for each stratigraphic log, which was divided into a number  $n$  of georeferenced elevation points  $(x, y, z)$ , associated with the lithofacies and a corresponding hydraulic conductivity  $(K[m/s])$ . In addition, where the stratigraphic layer was thicker than 1.0 m, the information was duplicated each meter.

#### 2.4.1.2.3. *Spatial interpolation*

The spatial variability of the main hydro-stratigraphic class was achieved from stratigraphic sections and deterministic and inferential statistical analysis. In particular, a geo-statistical analysis was carried out through the definition of a semi-variogram, i.e., the function of the spatial variability  $(\gamma(h))$  of a regionalised phenomenon  $(Z_i)$  expressed as follows:

$$\gamma(h) = \frac{1}{2N(h)} \sum_{i=1}^{N(h)} (Z_i(x) - Z_i(x+h))^2 \quad (2.02)$$

Where, for each considered lag  $h$ , the variability is measured by considering  $N$  couples of points located in  $x$  and in  $x+h$ , respectively. Subsequently, the obtained geostatistical variogram parameters were used for generating the distributed  $K_{aq}$  field with the Ordinary Kriging estimation algorithm in SGeMS (Remy et al., 2009). For areas not populated by stratigraphic data, the  $K_{aq}$  field was assigned according to geological and hydrogeological knowledge exclusively (Crosta et al., 2004; De Finis et al., 2017,2018; Fleckenstein et al., 2006).

#### 2.4.2. *Analysis and results*

The Valtellina floodplain was partitioned into 4 hydrological macro-areas defined with different levels of detail (**Figure 2.10**). The first subdivision was defined by taking into account the two-deposit detected in the geomorphological maps: the Alluvial zone and the Alluvial fan zone.

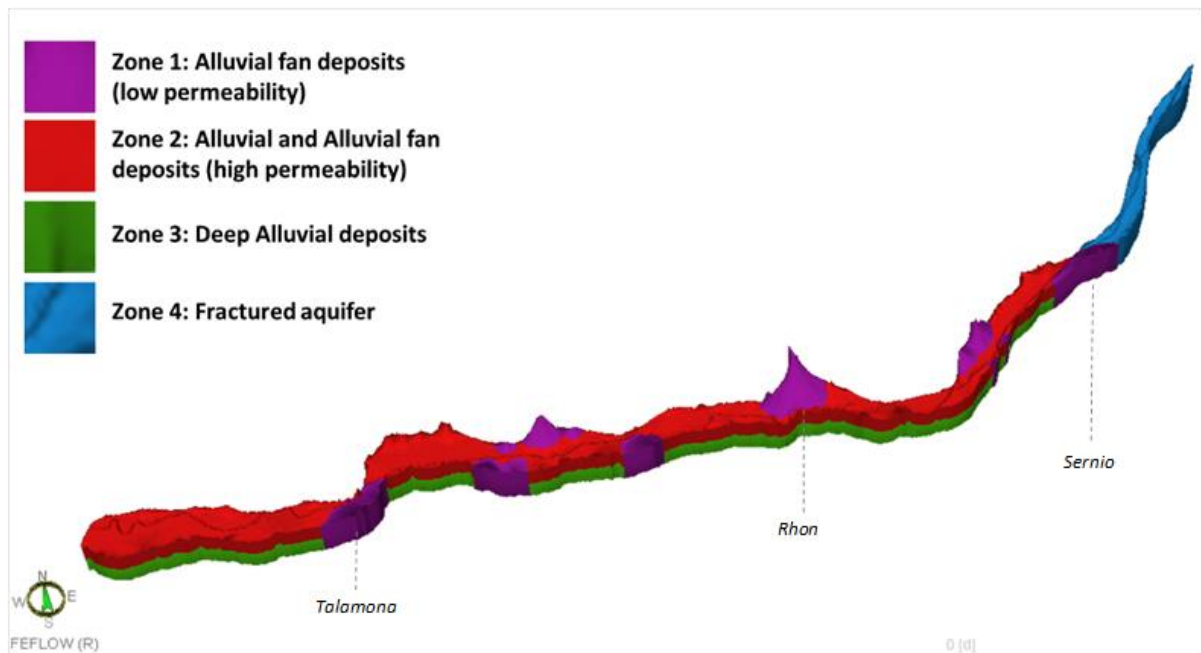


Figure 2.10: Conceptual model of the groundwater flow system.

Considering the location of the stratigraphic data, 50% of the logs provide information related to alluvial fan deposits. Here (Zone 2), the 60% of the deposits are characterised by 10 lithofacies, between gravel and gravel with sand, and only 7% are composed of fine material. Each of these lithofacies was associated with hydraulic conductivity values, as shown in **Table 2.1**. In addition, a trend in grain size has been detected (

**Figure 2.11**): fine deposits increase downstream, while, upstream, the deposits are composed almost entirely (80%) of gravel or gravel and sand. However, the distribution of wells does not allow a detailed stratigraphic characterisation of this environment. Firstly, the depths of the logs average 30m and do not allow the delimitation of the extension of the deposits in depth. In addition, logs are only located inside type I alluvial fans (originating from fluvial processes). This is because the main water-intensive urban areas (Morbegno, Sondrio, Tirano) are concentrated on these deposits.

Table 2.1: Prevalent lithofacies found from the analysis of 1746 borehole log data and their hydraulic conductivity values. The conductivity was estimated by considering the literature data.

Lithofacies	Hydraulic conductivity [m/s]
Rock (R)	1.00E-05
Coarse-grained gravel (Gg)	5.00E-02
Gravel (G)	1.00E-02
Gravel and Sand (Gs)	7.50E-03
Fine-grained gravel (Gf)	5.00E-04
Sand and Gravel (Sg)	5.00E-03
Sand (S)	7.50E-04
Fine-grained sand (Sf)	5.00E-05
Fine sediment (F)	1.00E-06
Soil	1.00E-05

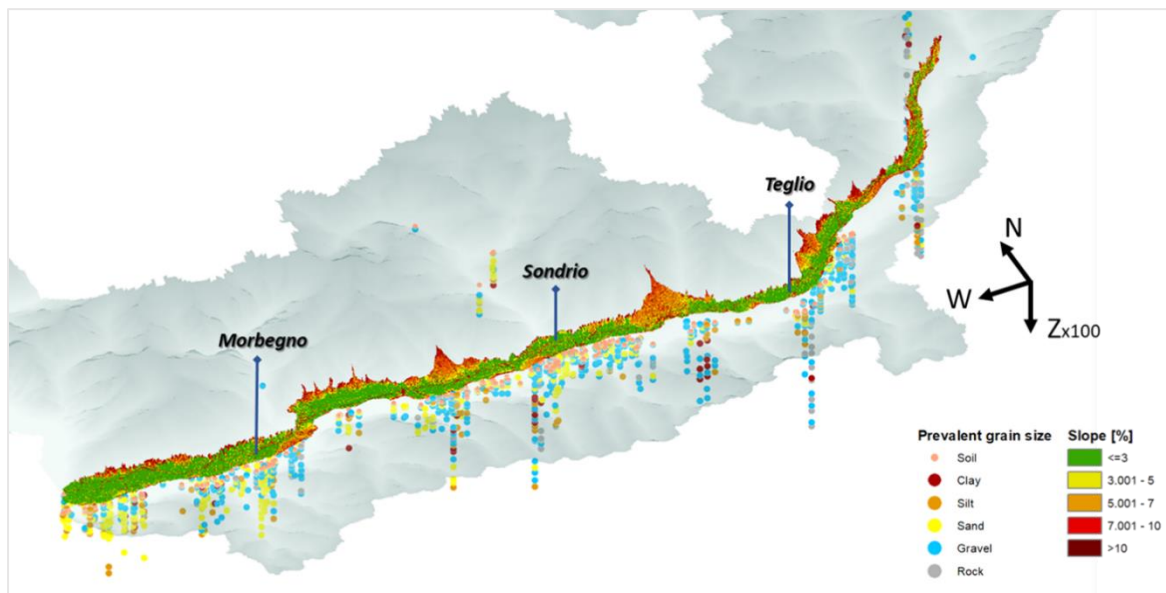


Figure 2.11: 3D view of the distribution of lithofacies in the available stratigraphic logs, located in the Zone 2 of the study domain. A decrease in grain size is observed from upstream to downstream.

Regarding the areas of type II and anomalous alluvial fans, the lack of data provides indirect evidence of the permeability of these areas. In fact, due to their origin, these deposits are composed of coarse material in an abundant fine matrix, which causes a reduction in permeability. Consequently, these areas have not been historically exploited. This environment represents Zone 1 of the domain, with a  $K_{aq}$  of  $1E-6$  m/s.

The alluvial/fluvial-glacial deposits were further discretized into 3 environments.

Deep fluvio-glacial deposits (depth > 200 m) represent the Zone 3, for which no hard stratigraphic data are available. However, seismic surveys conducted by Mele et al. (2021) and De Franco (2009) have shown homogeneous deep levels of low-velocity infill, consisting

of partially cemented fluvio-glacial gravel and sand deposits. For this reason,  $K_{aq}$  was set equal to  $1E-5$  m/s.

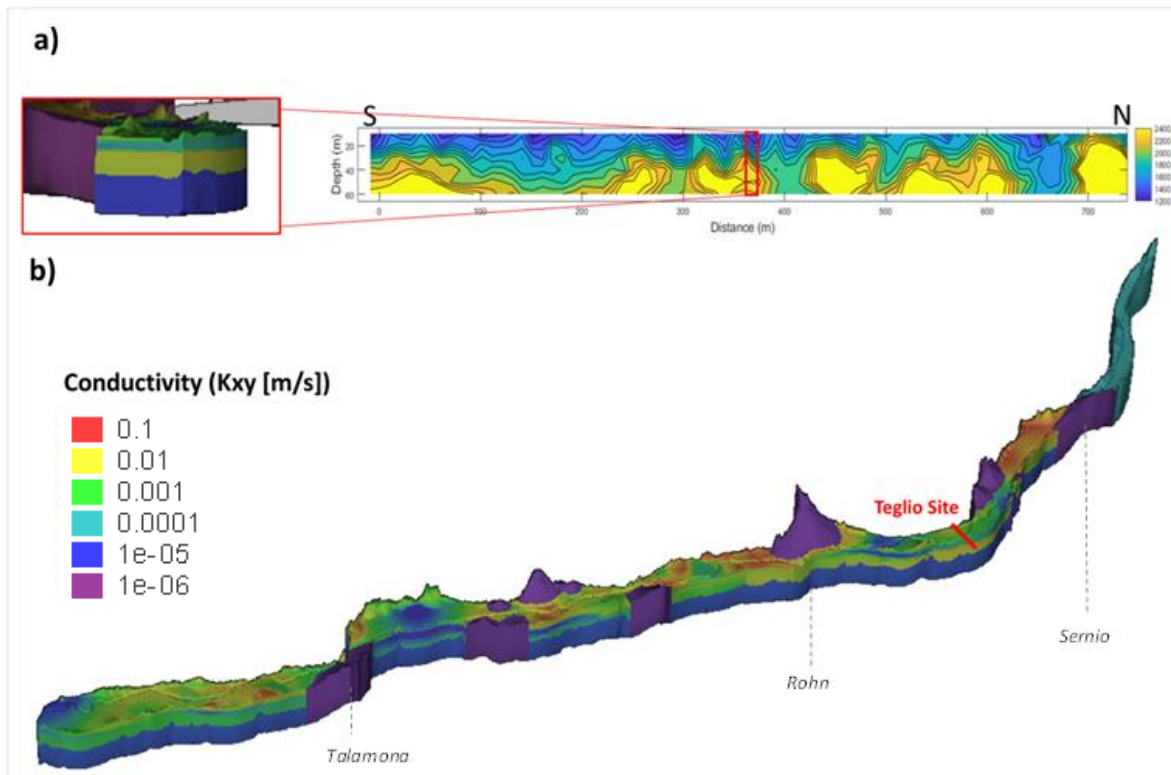


Figure 2.12: a) Reinterpretation of the seismic section in the first 60 m of depth at the Teglio site and detail of the hydraulic conductivity distribution (red box). Spatial distribution of the hydraulic conductivity (m/s) in the study domain (b).

For the more superficial deposits (depth <200m), 10 lithofacies are identified and associated with hydraulic conductivity and porosity values, as shown in **Table 2.1**. In the area upstream of the Sernio reservoir, the aquifer appears to be in fissured rock (Zone 4). This is clearly shown by the almost total composition of rock, blocks, and gravel. Downstream of the Sernio, statistical analysis of the data shows a predominant composition of deposits characterised by gravel and sand, with only 13% of fine materials (clay and silt). Due to the similar lithological composition, the superficial alluvial deposits and type-1 alluvial fans were merged into Zone 2, which represent the main superficial aquifer. However, the spatial distribution analysis of the logs and the reinterpretation of the seismic section revealed marked heterogeneity. A trend is observed throughout the valley, marked by a gradual increase in the sandy component of deposits (

**Figure 2.11**). Vertically, reinterpretation of the seismic section in the first 60 m revealed a change in seismic wave velocity at about 40 m depth (**Figure 2.12a**). Locally, the low

permeability level at the Teglio section may be associated with lacustrine deposits linked to a damming phase in the valley caused by the Rhon alluvial fan.

This discontinuity was not recognised continuously in the valley (**Figure 2.12b**). However, only upstream of the Ardenno dam, low permeability levels were recognised and confirmed by saturated soils subject to frequent flooding during precipitation events. Finally, the  $K_{aq}$  in the Zone 2 was estimated with the Ordinary Kriging algorithm. The geostatistical variogram parameters used are listed in **Table 2.2**. A spherical variogram was selected, with a nugget value of 0.0 log10 m/s and a sill value of 1.5 log10 m/s. The semivariogram range was set to 500 m in the N-S and E-W direction and 50 m vertically.

Table 2.2: Variogram Parameters Used for Generating the  $K_{aq}$

	Parameter	Model Type	Nugget (log10 m/s)	Sill (log10 m/s)	Range (EW, NS, Z)
Zone 1	$K_{aq}$	Spherical	0	1.5	500, 500, 50

For the spatial interpolation, the surface was discretized into a triangular finite elements mesh by using Triangle meshing method, and the value of  $K_{aq}$  was calculated for each node of the mesh. Mesh refining was applied to ensure good quality simulations: elements size decreases gradually from 100 to 25 m where surface-water/groundwater interaction occurs and from 100 to 10 m near the observation points. The mesh quality is very high with only 0.5% of triangles with obtuse angles ( $>120^\circ$ ), without violating the Delaunay's criterion. This discretization produced a surface mesh made of 61,365 nodes and 119,740 elements. Then, the volume between the topographic surface and the bedrock is discretized with 9, variably thick slices, ranging from 5 m at the top to a maximum of 200 m at the bottom of the model. In total, the 3D meshes consist of more than 2 million prismatic elements for the hydrodynamic flow model.

## 2.5. Rivers characterization

### 2.5.1. Methods

For the study of the interaction between the groundwater and the surface water, the main river and the tributaries were considered.

In order to reconstruct the morphology of streambed of the main river Adda, the Lidar DTM has been modified because the Lidar elevation along the water body is referred to the water level. Since only a few topographic sections of the streambed are available at major built structure (e.g., bridges), a constant simplified rectangular section was assumed for the river Adda. The elevation of the streambed ( $z_{rb}$  [m a. s. l]) was calculated as follows:

$$z_{rb} = z_{sw} - h \quad (2.03)$$

Where  $z_{sw}$  [m a.s.l] is the surface water elevation, derived from the interpolation of the values at the SW observation points (Appendix 1) during the monitoring campaigns, and  $h$  [m] is calculated as follows:

$$h = Q / w * V \quad (2.04)$$

Where  $Q$  [ $m^3/s$ ] is the discharge at hydrological stations, for the main river, or obtained from catchment hydrological analyses,  $w$  [m] is the river width, set equal to the distance between the two banks and measured orthogonally to the river axis, and  $V$  [m/s] is the velocity obtained indirectly at the points where the topographic section of the river is available.

For tributaries, the riverbed morphology was assumed the same as the DTM elevation since the stream stage is estimated less than the average value of accuracy of the DTM elevation products.

Finally, in the absence of historical data on the nature of the riverbed, a field survey was carried out in order to I) classify areas with cemented or natural riverbed, and II) define, for areas with a natural riverbed, the predominant grain size.

In lack of data, the streambed hydraulic conductivity ( $K_{rb}$  [m/s]) was defined by literature values (Chen et al., 2013; Naganna et al., 2017; Stewardson et al., 2016; Tang et al., 2018), assuming a natural stream bed.

## 2.5.2. Results

The study domain includes the Adda River and 19 tributary rivers (**Figure 2.13**).

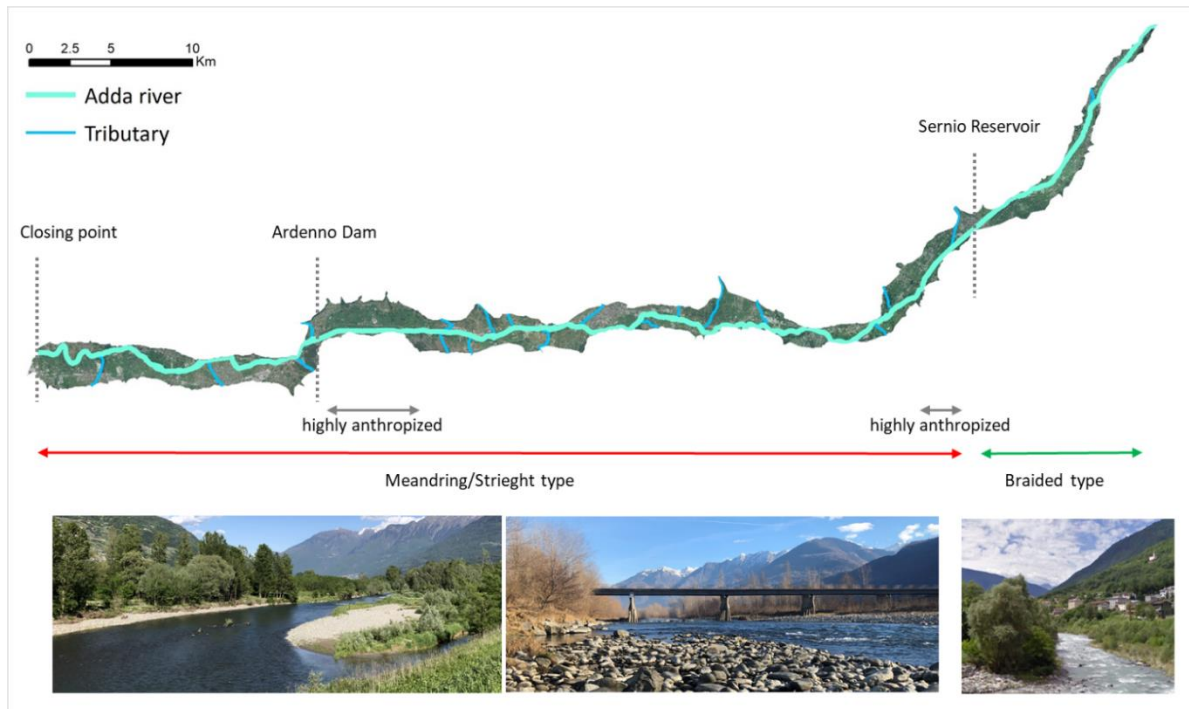


Figure 2.13: Summary scheme of the Adda river zoning, and location of the main tributaries on the floodplain

Considering the morphological characteristics, the Adda River was divided in two main sectors. The first one flows in N-S direction, along the upper part of the valley to the Sernio artificial reservoir. Here, the channel has a braided pattern with an average bankfull width of 40.0 m and a depth of 1-4 m. The sediments on the riverbed are characterised by a gravel-pebble type, with an increase in size at the tributary confluence. Hydrological monitoring data defined a losing or disconnected river behaviour with respect to groundwater flow. The second sector flows from the Sernio reservoir to the closing point of the Valtellina catchment. A single-thread channels and a progressive meanders pattern to the lower part of the valley was observed. The streambed has a width of 60 m and a depth of 4-8 m with a prevailing gravel sediment size. In addition, the streambed is affected by high fluvial erosion. This is clearly shown during the period of low stream stage, when the bridge piles are 2-3 m above the water level. In this area, the river and groundwater are closely connected and the stretches gaining or losing of the river may change in time and space.

Along the whole catchment area, the Adda River is highly anthropized. In fact, several longitudinal defence works could be found, mostly in the proximity of structure and banks

with high erosion rates. In addition, at downstream of the Sernio reservoir (about 5 km long) and upstream of the Ardenno dam (about 6 km long), the Adda river was completely rectified laterally and consolidated at the bottom.

For the tributaries, the assumption on the riverbed height was verified by considering the available historical data. The tributaries show a range of runoff from 0.2 m<sup>2</sup>/day to 15 m<sup>2</sup>/day and a maximum width of 30 m. These data confirm a riverbed depth of less than 1 m and within the accuracy range of the DTM. Due to the lack of data, the hydrological parameter for the streambed was assumed homogeneous, introducing a level of uncertainty. In fact, the riverbed should be considered heterogeneous in space and time because the erosive and depositional process acts on a daily basis on the porosity and distribution of preferential water pathways (Naganna et al., 2017; Tang et al. 2018). However, according to Birk et al. (2006), Shubert et al. (2006) and Tang et al. (2018), the variations are minimal, except after major flood events, and the assumption could be accepted.

Therefore, the value of  $K_{rb}$  was initially assigned to 0.0E-1 m/s for the consolidated bottom sections and a range between 1.0E-4 and 1.0E-6 m/s in the natural riverbed. The second value was defined by literature data: several sites and laboratory tests shown a high permeability for streambed characterized by a sands and gravels containing fine-grained fraction (5–15%) sediments (Naganna et al., 2017; Stewardson et al., 2016; Tang et al., 2018).

## 2.6. Steady-state Groundwater flow model

A steady-state finite element numerical model (WASY software-FEFLOW: Diersch, 2013), suitable for complex three-dimensional groundwater flows, was used to set and calibrate the groundwater model of the floodplain.

### 2.6.1. Methods

#### 2.6.1.1. Numerical model: Feflow

FeFlow is a software for solving numerically the groundwater flow equations within a three-dimensional porous medium, using the finite element method. In order to solve the flow equations, the software needs a vertical and horizontal discretization of the domain of interest into homogeneous elements, on which to apply the set of the three-dimensional flow algebraic equations of the mathematical model. The 3D mesh was subdivided in  $n$  zones based on the geological conceptual model obtained in the previous step of the workflow.

For an unconfined phreatic aquifer, the numerical model allows to solve the Darcy equation in porous media, as follows:

$$\frac{\delta}{\delta x} \left( K_{xx} \frac{\delta h}{\delta x} \right) + \frac{\delta}{\delta y} \left( K_{yy} \frac{\delta h}{\delta y} \right) + \frac{\delta}{\delta z} \left( K_{zz} \frac{\delta h}{\delta z} \right) + W = S_s \frac{\delta h}{\delta t} \quad (2.05)$$

Where  $K_{xx}$ ,  $K_{yy}$  and  $K_{zz}$  [L/T] are the principal components of the hydraulic conductivity tensor, assumed to be parallel to the direction of the three geometric axes,  $h$  is the hydraulic head [L],  $S_s$  is the specific storage of the porous medium [L-1], while  $W$  is the specific loss or recharge relative to the aquifer system [T-1].

A hydraulic property value in the three directions was assigned to each 3D element. For the heterogeneous zones, the 3D meshes were imported into SGEMS (Remy, 2009), and used as interpolation grid for Ordinary Kriging, where the variogram parameters are set equal to those obtained from geostatistical analysis of available data.

The exchange between the river and the groundwater is solved considering the follow relation:

$$Q = AC(h_r - h_a) \quad (2.06)$$

Where the inflow or outflow to/from the groundwater system ( $Q$  [ $L^3/T$ ]) is function of the area ( $A$  [ $L^2$ ]), the hydraulic gradient between the river and the aquifer ( $(h_r - h_a)$  [ $L$ ]), and the streambed conductance  $C$  [ $T^{-1}$ ]. In particular, the conductance is defined as the ratio between the hydraulic conductivity ( $K_{rb}$ , [ $L/T$ ]) and the thickness of the clogging layer of the river ( $d$ , [ $T^{-1}$ ]) (Hantush, 1965; Kollet and Zlotnik, 2007).

#### 2.6.1.2. Boundary conditions

A constant-head (Dirichlet type) boundary condition (BC) corresponding to hydraulic head was imposed at upstream and downstream boundary nodes ( **Figure** 2.14). Along the main rivers and the tributaries, a fluid-transfer BC (Cauchy type) was applied in order to account for surface-water/groundwater interaction. For the main river, a predefined reference head was set equal to the elevation of the water table measured along the main river network. Instead, for the tributary, an estimation of the stream stage was carried out from the historical discharge. The northern and southern boundaries of the superficial layer, coincident with mountain slopes, were considered as no-flow BC (Neumann type).

To simulate effective recharge, a spatially distributed inflow value (mm/year) was assigned imported in Feflow to surface elements belonging to permeable sedimentary units. The map of the infiltration was obtained from the hydro-meteorological analysis of the 2019-2020 year.

In addition, 173 extraction wells have been included in the area, for which the flow rate in l/s is known from public documentation relating to the concessions and is assumed to be constant throughout the year.

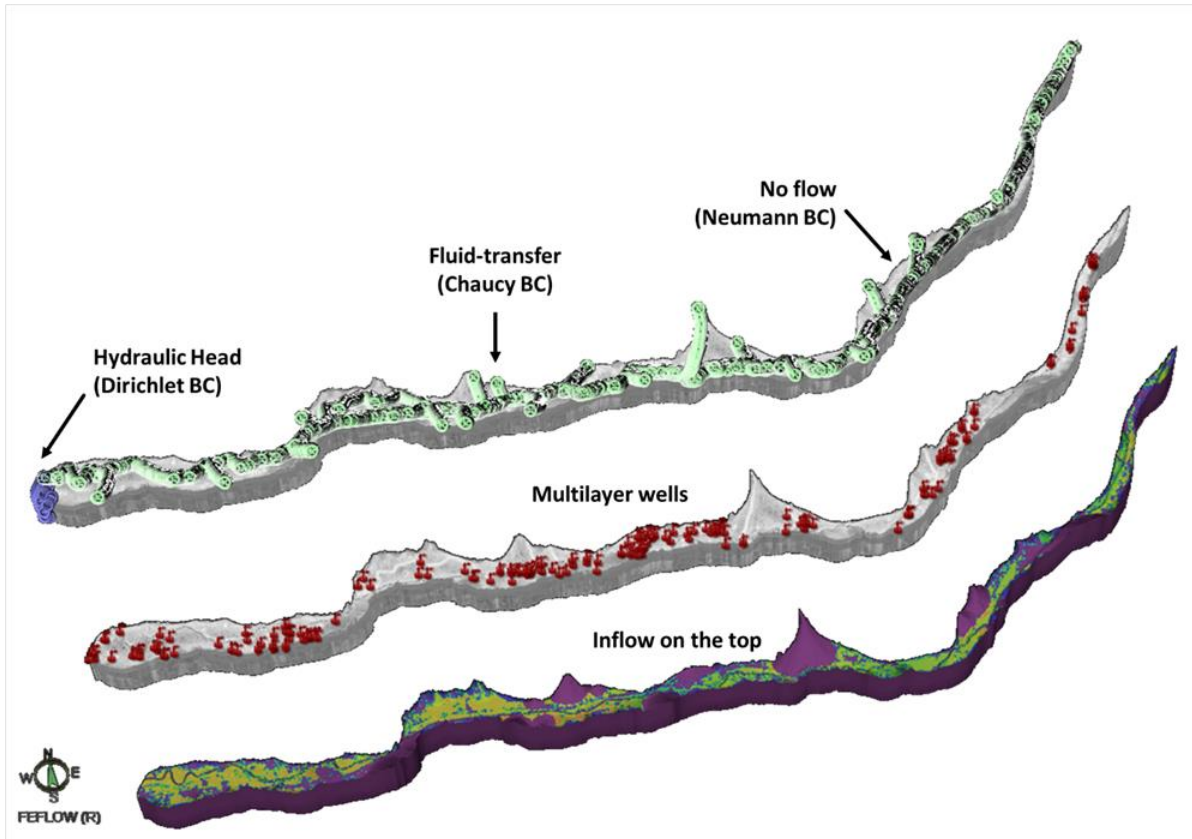


Figure 2.14: Boundary conditions and source/sink terms considered in the 3D model

Finally, for the numerical resolution of the flow model, different calculation codes can be set up, including:

- I) Direct solution strategy that provides the advantage of an exact solution of the equation system without any residual error due to a solver iteration.
- II) Preconditioned conjugate-gradient method (PCG), which allows a termination criterion to be set for the iteration of the solver, useful in cases where there are very strong contrasts in the size of elements within the model domain.
- III) Algebraic Multigrid Method (SAMG), which is optimal for simulations in stationary conditions, when the circumstantial conditions differ significantly from the expected results and when the variability of the dimensions of the individual elements making up the mesh is high.

### 2.6.1.3. Calibration of the Hydrogeological parameters: PEST

The calibration was achieved with PEST code (Doerthy & Hunt, 2010). PEST (Parameters ESTimation code) is a procedure to set the input parameters of a model in order to obtain

results that reflect reality as closely as possible. It is an automatic calibration process in that, for each input parameter in the model, the user assigns an initial value and defines a range of variation that must be respected throughout the processing, and then, the necessary number of simulations are carried out to determine the best configuration of the parameters.

In highly parameterized models, such as the groundwater flow models, the mathematic method of the regularized inversion is usually applied, due to the complexity of the problem. This type of inversion is based on the principle of least squares minimisation, where the best result is the lowest sum of squared differences between estimated and measured solutions. In particular, the degree of fit is expressed by the objective function  $[\Phi]$ , defined as the weighted  $[W_i]$  sum of squares of the residuals between measurement  $[h_i^{obs}]$  and simulation  $[h_i^{sim}]$  results:

$$\Phi = \sum_i W_i (h_i^{obs} - h_i^{sim})^2 \quad (2.07)$$

It is important consider in the assessment of the fitting that the parameters estimated are accompanied by a-priori error, as a consequence of I) the simplified simulation of a complex natural world and II) the noise in the observations used to constrain estimates of parameter. In the present work, 54 observation points corresponding to the groundwater monitoring network located in the shallow aquifer along the valley floor were taken into account.

The mathematical regularization could be reduced into three broad categories: the Tikhonov regularization, the subspace regularization, and the combination of these two. The first one (Tikhonov, 1963a, 1963b; Tikhonov and Arsenin, 1977) provides a vehicle for formally incorporating the intuitive knowledge and geological expertise information into the calibration process: Tikhonov regularization, if properly formulated, is enable determine a unique solution to the inverse problem that balances the model's fit to the observed data and adherence to the soft knowledge of the system. The minimization of the objective function consists in the definition of special pseudo-observations, pertaining to a preferred condition for one or more parameters employed by the model, that constitute a suite of fallback values for parameters, or for relations between parameters. During the calibration processes, the fallback value prevails where the information dataset is insufficient for unique estimation of certain parameters, or combinations of parameters. Instead, subspace regularisation allows

faster and numerically stable solution for problems with large numbers of parameters. The method simplifies the parameterisation by subtracting parameters, defined as inestimable based on the calibration dataset, from the inversion (Aster et al., 2005). The subspaces, where the parameters are calibrated, are obtained by the application of the singular value decomposition (SVD) or least squares method (LSQR) algorithm: these algorithms allow the decomposition of the weighted Jacobian matrix through the linear combination of smaller matrices. Moreover, the application of this regularization requires a pre-calibration based on the knowledge of the system. In fact, it maintains values assigned in the initial phase for parameters that are considered inestimable, thus preserving the geological setting. The last category is the SVD-Assist algorithm. The SVD-Assist consists in an extremely reduced computational time of the regularized inversion process compared to traditional methods, while combining the characteristic simplicity of the Tikhonov method with the numerical stability due to SVD.

The spatial distribution of the parameter in the model domain could be set in multiple way considering the prior information. The spatial parametrization could be defined for I) constant zone, where parameters are considered homogenous, or for II) pilot-point, where parameters are estimated in a number of discrete positions and are automatically interpolated to the rest of the model domain. The pilot points, according to the guidelines suggested by Doherty, Fienen and Hunt (2010), should generally be distributed homogeneously within the domain, increasing the density in areas with more information. In addition, it is possible to combine the two spatial parameterisations, defining groups of pilot points for homogeneous zones, in order to take into account the variability of the spatial distribution of homogeneous zone.

For the calibration of the Valtellina floodplain model, the parametrization was defined considering 4 geological zones in which the model was subdivided and for which a constant hydraulic conductivity was estimated. For heterogeneous areas, the hydraulic conductivity was estimated in a number of discrete positions corresponding to a subset of the hydro-stratigraphic information available. The rest of the model domain was interpolated with 3D Ordinary Kriging, where the variogram parameters are set equal to those obtained from geostatistical analysis of available data.

To assess the result of the calibration, the deviation between calibrated set and initial set was considered. Moreover, the sensitivity distribution result was analysed to understand the influence of the observation points on the regularized calibration.

### 2.6.2. Results

A steady-state calibration of  $K_{aq}$  of the unconfined aquifer and  $K_{rb}$  of the main river and the tributary was performed. The average groundwater levels recorded in the year 2019-2020 at 47 observation wells were used as initial condition for executing steady-state simulation. The simulation results are shown with the measured data in **Figure 2.16b**. The comparison between the observed and the measured data give a root mean square of 8.15 m and an absolute error of 6.35 m.

Then, the parameters were calibrated using FePEST, integrating the FEFLOW model into the PEST (Doherty 2015) framework. For the autocalibration 138 parameters were defined, considering the 4 hydrostratigraphic zones, and the conductance of the streambed for the exchange with the aquifer in the two directions (inflow and outflow). In particular, for the Zone 2 with a heterogeneous distribution of the hydraulic conductivity, 130 pilot points were selected at 3 different depths (10 m, 40m, and 80 m), in correspondence of available boreholes data (**Figure 2.16a**). Moreover, the calibration of the riverbed conductance was obtained for homogeneous zones in the meander section, in the braided section, and at the tributaries. The objective function was based on the observed water heads and a constant weighting factor was assigned to the hydraulic heads contributing to the objective function.

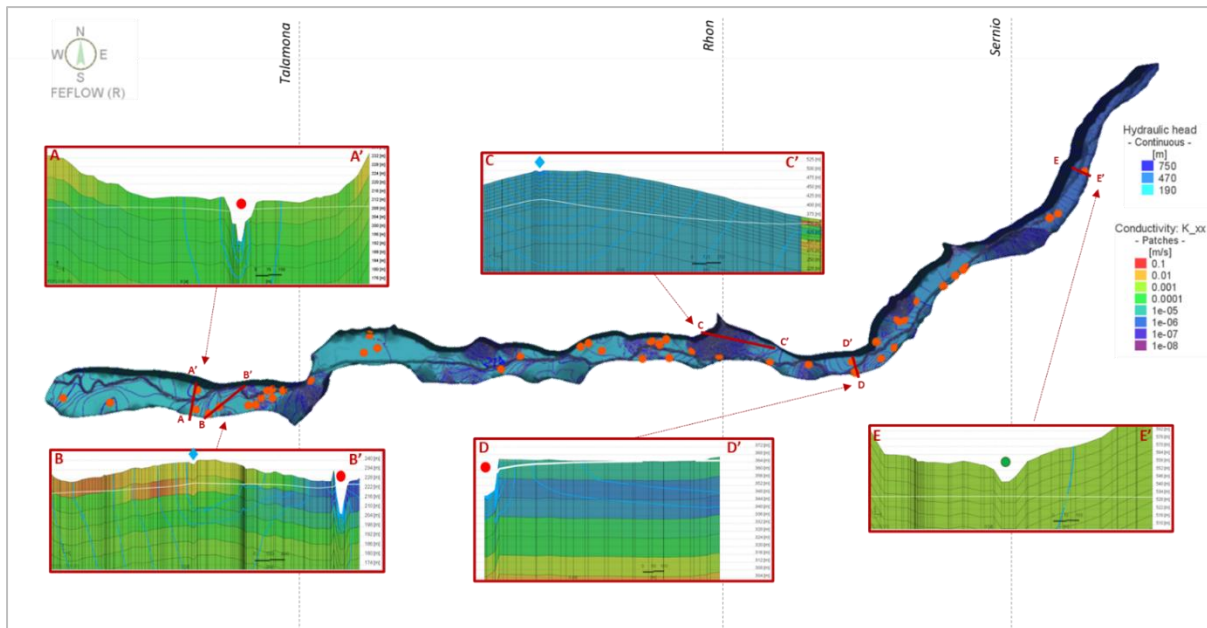


Figure 2.15: Result of the calibrated steady state model with the location of the observation points (orange points). In the boxes, 5 vertical sections of the water table (white line) for the visualisation of the relationship between the Adda river (red point= meander section; green point= braided section) and the tributary (blue diamond) and the groundwater.

A decrease of the residual of 80% was observed, with an RMS of 1.47 m and an E of 1.06 m (Figure 2.16b). The calibration results indicate a reasonable agreement between the calculated and observed heads considering the large range of head variability along the valley (500 to 200 m a.s.l.) and the high level of fluctuation during the hydrologic year ( $\pm 2$  m). The balance of rates in the steady state simulation shows a total equilibrium in the problem setting, where interchange with rivers involves almost all the volumes involved. Furthermore, considering the piezometric map obtained from the simulation, different relationships with the aquifer are observed between the Adda and the tributaries (Figure 2.15). As shown in sections BB' and CC', the tributaries are generally disconnected from the aquifer. However, they are attributed an important function in recharging and raising the water table, by conveying volumes from secondary valleys into the valley floor aquifer. Along the axis of the alluvial plain, the meandering section of the Adda and the aquifer are generally in contact and in equilibrium, with local areas where groundwater feeds the Adda River (section DD'). In contrast, in the braided section of the Adda, no exchange of flows with the aquifer is observed (section EE').

Figure 2.16c and d show the results of the calibration of the hydraulic conductivities at the pilot points in Zone 2. For the pilot points located at a depth of 10 m, the median of the K calibrated values is 0.5 orders of magnitude lower than the initial one, and the residuals

between the pre- and post-calibration values, considering a range of 25-75% of the data, go from -0.4 to +0.8 log<sub>10</sub> m/s. However, the highest residual values occur for points that were initially set with low conductivities (1E-06 m/s), indicating an initial underestimation of the permeability of the layers. For pilot points at 40 m depth, the median of the K is 1.1 orders of magnitude lower than the initial median. In addition, it is observed that, although the 75th percentile is unvaried, the 25th percentile is one order of magnitude higher than the initial K at the pilot points. Finally, even for pilot points located at 80 m depth, the median is an order of magnitude lower, with residual values ranging from the 75th percentile of 0.9 log<sub>10</sub> m/s, to the 25th percentile of -0.7 log<sub>10</sub> m/s. However, it should be noted that there are only a small number of points available at this depth (<10 points).

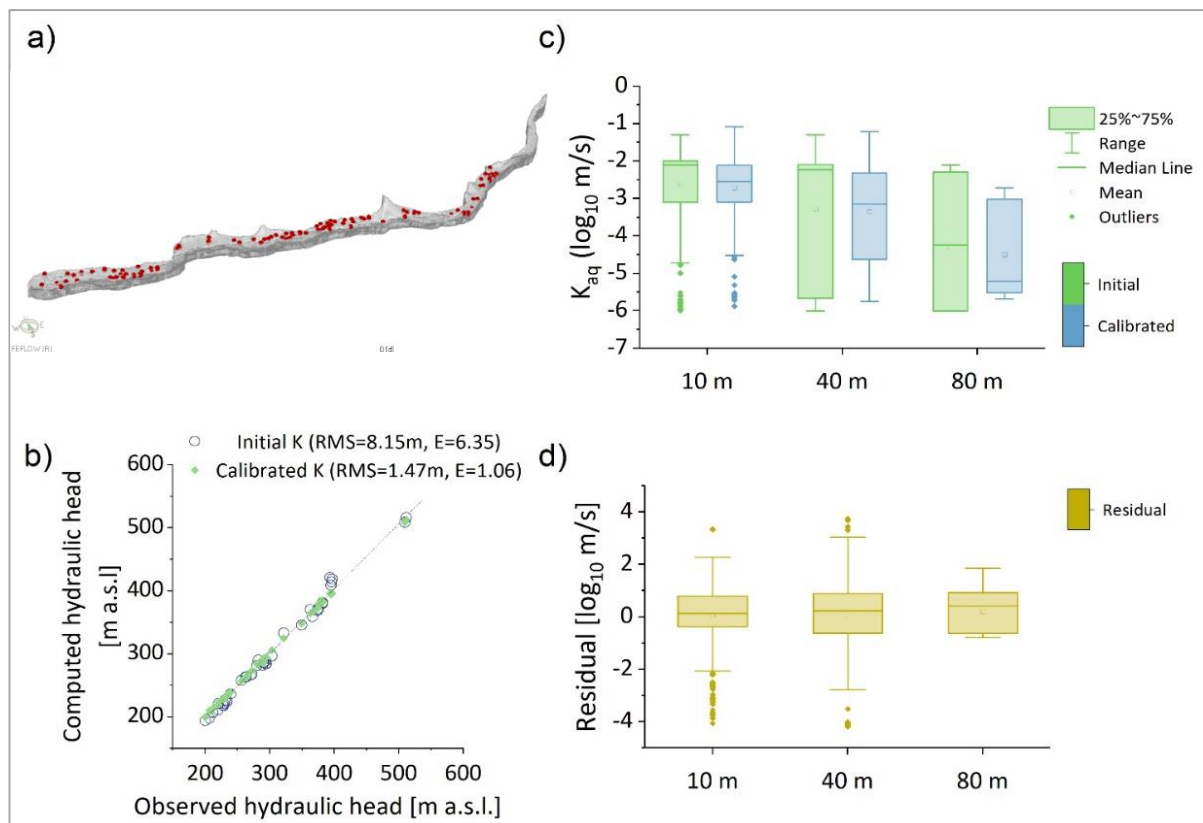


Figure 2.16: Calibration of the model. a) Spatial distribution of the 130 pilot points (red dots) and the homogeneous zones. b) Comparison of the computed and observed hydraulic head pre (Initial K) and post (Calibrated K) auto calibration: RMS = root mean square; E = absolute error. c) and d) Comparison between the initial K (log<sub>10</sub> m/s) values and the calibrated K (log<sub>10</sub> m/s) at the pilot point location.

For the homogeneous zones, the results of the calibration are shown in **Table 2.3**. In the deep alluvial zone (Zone 3) and in the fractured aquifer upstream of the model (Zone 4), the calibration returned permeability values one order of magnitude higher than assumed. In contrast, Zone 2, characterised by anomalous alluvial fans, confirmed the initial low permeability of the deposits. For the riverbed, the self-calibration returned conductance

values (Table 2.3) consistent with the predicted lower limit ( $\approx 1E-6$  m/s) in literature for streambed characterised by sands and gravels, with fine-grained fraction (5-15%) sediments. Moreover, for the three river types, a conductance value for the flow towards the aquifer ( $K_{rb}$  inflow) is observed to be about one order of magnitude lower than the conductance values for the flows from the aquifer to the river ( $K_{rb}$  outflow). This is consistent with the literature; several studies, in fact, have demonstrated that an inflow into the aquifer makes the clogging layer impermeable in the first metre of thickness, due to the deposition of suspended fine particles (Chen et al., 2013; Fox et al., 2018; Jasechko et al. 2021). Instead, where an outflow from the aquifer occurs, the clogging layer is more permeable, since fine particles are lifted from the streambed and then swept away by the streamflow (Chen et al., 2013; Preziosi-Ribero et al., 2020).

For the observation points, a sensitivity analysis was carried out considering the simulations carried out during model calibration (Figure 2.17). The analysis shows the highest sensitivity values for the  $K_{rb}$  of tributary conductance. This further confirms that the alluvial river-

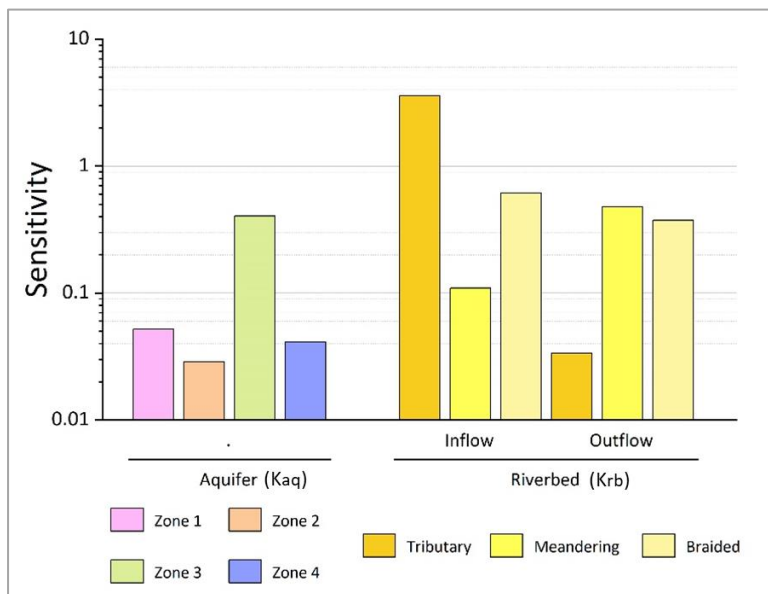


Figure 2.17: Sensitivity analysis of calibrated hydraulic parameters ( $K_{aq}$  for the Aquifer in the four zones;  $K_{rb}$  for the river-aquifer interaction, in outflow or inflow condition, for the different river condition).

aquifer systems in the Valtellina valley floor are strongly influenced by river seepage and by the recharge from the high-altitude mountain area. To improve the result obtained, a greater discretization of the parameter would be appropriate, following a careful analysis of the heterogeneity of the riverbed and tributaries.

Table 2.3: Comparison between the initial hydraulic parameters and the calibrated values.

		Estimated K [m/s]	Calibrated K [m/s]
$K_{aq}$	Zone 1	1.00E-06	4.40E-06
	Zone 3	1.00E-05	2.23E-04
	Zone 4	1.00E-04	1.10E-03
$K_{rb}$ inflow	Tributary	1.00E-06	3.76E-06
	Meandering	1.00E-06	1.13E-06
	Braided	1.00E-06	0.95E-06
$K_{rb}$ outflow	Tributary	1.00E-05	3.74E-05
	Meandering	1.00E-05	6.60E-06
	Braided	1.00E-05	5.20E-06

## 2.7. Conclusion

The accurate characterisation of the structural and lithological heterogeneity of a floodplain requires the collection and interpretation of detailed 3D geological and hydrogeological data. However, in mountain valley floor areas, this information is often limited, also because groundwater in mountainous areas is generally of little interest with respect to the surface water resources. However, the application of geostatistical reconstruction techniques and parameterization by autocalibration algorithms, together with the geomorphological and geological study of the area, make it possible to obtain reliable conceptual models.

The proposed workflow has enabled the development of a 3D hydrogeological model of the Valtellina flood plain. In particular, the valley floor was divided into 4 areas with different level of information and different hydraulic properties. Considering the monitoring network of the University of Milan Bicocca, the steady-state simulation of the calibrated hydrogeological model provides an acceptable error of less than 2m.

Considering the limited information available on the main river and tributaries, geomorphological study of the hydrological network was fundamental. The sensitivity analysis showed that the steady-state flow simulation is strongly influenced by the parameterisation of the riverbed conductance value. However, the results of this study have shown that this model is able to investigate the dynamics of river-aquifer exchange. Consequently, the model can be used as a tool to the study of the relationship between surface water and groundwater under the impact of climate change.

## 2.8. Appendix 1

The following table lists the points of the Valtellina monitoring network. For each point, the altitude (m a.s.l.), the coordinates (WGS 1984 in decimal degree), the sampling frequency and the available time interval are indicated. The points with the prefix "Ms" indicate the points belonging to ARPA meteorological and hydrogeological monitoring network. For these points, the variables collected are temperature (T), precipitation (P), snow depth (SD), wind speed (W), relative humidity (Hum), global radiation (R), and discharge (Q) and stage (Hsw) of the stream. The network, developed by the University of Milano Bicocca group, is divided into groundwater ("Gw" prefix) and surface water ("Sg" prefix) monitoring points. Here, hydraulic head (Hgw and Hsw), temperature (T), pH, electrical conductivity (cond.E) and main ions (MI) are collected.

	<i>ALT [m a.s.l.]</i>	<i>Lat wGS84 [DD]</i>	<i>Lon wGS84 [DD]</i>	<i>Variable</i>	<i>Resolution used</i>	<i>time interval</i>
<b>Ms01</b>	1950	46.129688	10.148266	SD, P	daily	2016-2020
<b>Ms02</b>	1172	46.453701	10.366032	P, T, w, Hum, R	daily	2016-2020
<b>Ms03</b>	274	46.154927	9.792523	P, T, w, Hum, R	daily	2016-2020
<b>Ms04</b>	2040	46.321466	9.763076	SD, P	daily	2016-2020
<b>Ms05</b>	2014	46.290759	9.863706	SD, P	daily	2016-2020
<b>Ms06</b>	993	46.167263	9.45814	P	daily	2016-2020
<b>Ms07</b>	199	46.150329	9.412275	P, T, Q	daily	2016-2020
<b>Ms08</b>	1875	46.026197	9.571121	SD, P	daily	2016-2020
<b>Ms09</b>	1220	46.327062	10.245981	SD, P	daily	2016-2020
<b>Ms10</b>	1970	46.305757	9.92752	SD, P	daily	2016-2020
<b>Ms11</b>	2151	46.292907	9.884528	SD, P	daily	2016-2020
<b>Ms12</b>	3032	46.34981	9.915154	SD, P	daily	2016-2020
<b>Ms13</b>	2660	46.477098	10.205837	SD, P	daily	2016-2020
<b>Ms14</b>	230	46.136635	9.584344	P, T, w, Hum, R	daily	2016-2020
<b>Ms15</b>	2440	46.096514	9.969999	SD, P	daily	2016-2020
<b>Ms16</b>	959	46.291989	10.082806	Hsw-Q	daily	2018-2019
<b>Ms17</b>	307	46.165595	9.848505	P, T, w, Hum, R	daily	2016-2020
<b>Ms18</b>	357	46.158277	10.03848	P, Hsw-Q	daily	2016-2020
<b>Ms19</b>	1750	46.244091	10.17332	SD	daily	2016-2020
<b>Ms20</b>	481	46.218168	10.182292	P, T, w, Hum, R	daily	2018-2020
<b>Ms21</b>	1948	46.512933	10.323059	SD, P	daily	2016-2020
<b>Ms22</b>	2300	46.453565	10.305964	SD, P, T, w, Hum, R	daily	2016-2020
<b>Ms23</b>	1050	46.384385	10.353989	SD, P	daily	2016-2020
<b>Ms24</b>	1730	46.41215	10.494665	SD, P	daily	2016-2020
<b>Ms25</b>	1950	46.229316	9.581636	SD, P	daily	2016-2020
<b>Gw01</b>	560.69	46.263116	10.258204	Hgw, MI	quarterly, daily	2016-2021
<b>Gw02</b>	514.327	46.239817	10.237396	Hgw, T, pH, Cond.E, MI	quarterly	2019-2020
<b>Gw03</b>	512.082	46.237487	10.230587	Hgw, T, pH, Cond.E	quarterly	2019-2020
<b>Gw04</b>	425.471	46.210842	10.164063	Hgw, T, pH, Cond.E, MI	quarterly, daily	2016-2020
<b>Gw05</b>	421.781	46.20905	10.162052	Hgw, T, pH, Cond.E, MI	quarterly	2019-2020
<b>Gw06</b>	415.941	46.205814	10.155776	Hgw, T, pH, Cond.E	quarterly	2019-2020
<b>Gw07</b>	406.862	46.199907	10.146193	Hgw, T, pH, Cond.E, MI	quarterly	2019-2020
<b>Gw08</b>	395.552	46.191587	10.123614	Hgw, MI	daily	2016-2021

<b>Gw09</b>	389.104	46.181272	10.114556	Hgw	quarterly	2019-2020
<b>Gw10</b>	386.299	46.18041	10.110382	Hgw, T, pH, Cond.E	quarterly, daily	2019-2021
<b>Gw11</b>	389.716	46.181755	10.108262	Hgw, MI	quarterly	2019-2020
<b>Gw12</b>	380.689	46.165582	10.1067	Hgw	quarterly	2019-2020
<b>Gw13</b>	377.574	46.168824	10.092176	Hgw, T, pH, Cond.E, MI	quarterly	2019-2020
<b>Gw14</b>	371.353	46.151978	10.074718	Hgw, T, pH, Cond.E	quarterly	2019-2020
<b>Gw15</b>	367.798	46.158006	10.072195	Hgw	quarterly	2019-2020
<b>Gw16</b>	365.829	46.156386	10.037046	Hgw, MI	quarterly	2019-2020
<b>Gw17</b>	352.92	46.158574	10.006101	Hgw, T, pH, Cond.E, MI	quarterly	2019-2020
<b>Gw18</b>	373.386	46.162382	9.965143	Hgw	quarterly	2019-2020
<b>Gw19</b>	322.536	46.165056	9.944003	Hgw, T, pH, Cond.E	quarterly	2019-2020
<b>Gw20</b>	295.828	46.159783	9.925219	Hgw	quarterly	2019-2020
<b>Gw21</b>	295.768	46.160893	9.925111	Hgw	quarterly	2019-2020
<b>Gw22</b>	295.45	46.171141	9.922561	Hgw, MI	quarterly	2018-2020
<b>Gw23</b>	293.61	46.168161	9.917344	Hgw	quarterly	2019-2020
<b>Gw24</b>	293.54	46.168887	9.916749	Hgw, MI	quarterly	2019-2020
<b>Gw25</b>	297.288	46.170493	9.910497	Hgw	quarterly	2019-2020
<b>Gw26</b>	297.1	46.17032	9.909496	Hgw	quarterly	2019-2020
<b>Gw27</b>	292.635	46.160599	9.903341	Hgw, MI	quarterly, daily	2019-2020
<b>Gw28</b>	294.44	46.165475	9.870284	Hgw, T, pH, Cond.E	quarterly, daily	2017-2020
<b>Gw29</b>	291.895	46.15707	9.860779	Hgw	quarterly	2019-2020
<b>Gw30</b>	292.799	46.169448	9.859665	Hgw, MI	quarterly, daily	2018-2020
<b>Gw31</b>	286.834	46.167433	9.853334	Hgw, MI	quarterly	2016-2020
<b>Gw32</b>	277.509	46.162566	9.803937	Hgw, T, pH, Cond.E	quarterly	2019-2020
<b>Gw33</b>	274.241	46.155184	9.788324	Hgw	quarterly	2019-2020
<b>Gw34</b>	265.139	46.167809	9.687879	Hgw	quarterly	2019-2020
<b>Gw35</b>	267.254	46.175284	9.681456	Hgw	quarterly	2019-2020
<b>Gw36</b>	264.443	46.165243	9.676749	Hgw, MI	quarterly	2019-2020
<b>Gw37</b>	272.917	46.149277	9.634032	Hgw	quarterly	2019-2020
<b>Gw38</b>	263.151	46.151781	9.633456	Hgw	quarterly	2019-2020
<b>Gw39</b>	267.334	46.149522	9.630517	Hgw	quarterly	2019-2020
<b>Gw40</b>	244.368	46.143995	9.610658	Hgw, T, pH, Cond.E	quarterly	2019-2020
<b>Gw41</b>	238.64	46.140393	9.603844	Hgw, T, pH, Cond.E	quarterly	2019-2020
<b>Gw42</b>	237.419	46.139122	9.602476	Hgw	quarterly	2019-2020
<b>Gw43</b>	238.597	46.139888	9.601975	Hgw, T, pH, Cond.E, MI	quarterly, daily	2019-2021
<b>Gw44</b>	239.947	46.144569	9.601262	Hgw, T, pH, Cond.E, MI	quarterly	2019-2020
<b>Gw45</b>	237.978	46.144203	9.597451	Hgw, T, pH, Cond.E, MI	quarterly, daily	2019-2021
<b>Gw46</b>	232.341	46.139814	9.592787	Hgw, MI	quarterly, daily	2018-2020
<b>Gw47</b>	230.354	46.136071	9.588064	Hgw	quarterly	2019-2020
<b>Gw48</b>	235.255	46.135631	9.581816	Hgw	quarterly	2019-2020
<b>Gw49</b>	238.433	46.135016	9.558947	Hgw, MI	quarterly	2019-2020
<b>Gw50</b>	223.053	46.143367	9.558133	Hgw	quarterly	2019-2020
<b>Gw51</b>	220.287	46.142317	9.55135	Hgw	quarterly	2019-2020
<b>Gw52</b>	226.625	46.131067	9.549699	Hgw, MI	quarterly	2018-2020
<b>Gw53</b>	220.917	46.137895	9.547946	Hgw	quarterly	2019-2020
<b>Gw54</b>	215.368	46.14438	9.540328	Hgw	quarterly	2019-2020
<b>Gw55</b>	216.681	46.133363	9.539134	Hgw	quarterly	2019-2020
<b>Gw56</b>	221.645	46.134048	9.531571	Hgw	quarterly	2019-2020
<b>Gw57</b>	219.633	46.13745	9.469009	Hgw, T, pH, Cond.E, MI	quarterly, daily	2018-2020
<b>Gw58</b>	202.016	46.140288	9.430385	Hgw, T, pH, Cond.E	quarterly	2019-2020
<b>Sw01</b>	545.216	46.260912	10.25179	Hgw, T, pH, Cond.E, MI	quarterly	2019-2020
<b>Sw02</b>	501.712	46.236253	10.225707	Hgw, T, pH, Cond.E, MI	quarterly	2019-2020
<b>Sw03</b>	420.89	46.211324	10.164202	Hgw, T, pH, Cond.E, MI	quarterly	2019-2020
<b>Sw05</b>	369.192	46.162481	10.087887	Hsw, T, pH, Cond.E	quarterly	2019-2020

<b>Sw06</b>	356.876	46.158367	10.037981	Hgw, T, pH, Cond.E, MI	quarterly	2019-2020
<b>Sw07</b>	348.479	46.160353	9.990734	Hgw, T, pH, Cond.E, MI	quarterly	2019-2020
<b>Sw08</b>	307.86	46.157825	9.949483	Hsw, T, pH, Cond.E	quarterly	2019-2020
<b>Sw09</b>	295.998	46.164589	9.930313	Hsw, T, pH, Cond.E	quarterly	2019-2020
<b>Sw10</b>	288.359	46.167558	9.903794	Hgw, T, pH, Cond.E, MI	quarterly	2019-2020
<b>Sw11</b>	283.738	46.158377	9.860463	Hgw, T, pH, Cond.E, MI	quarterly	2019-2020
<b>Sw12</b>	274.083	46.16053	9.816889	Hgw, T, pH, Cond.E, MI	quarterly	2019-2020
<b>Sw13</b>	266.958	46.159239	9.743053	Hsw, T, pH, Cond.E	quarterly	2019-2020
<b>Sw14</b>	265.121	46.160186	9.68835	Hsw, T, pH, Cond.E	quarterly	2019-2020
<b>Sw15</b>	240.919	46.143075	9.610363	Hgw, T, pH, Cond.E, MI	quarterly	2019-2020
<b>Sw16</b>	220.101	46.145446	9.564627	Hsw, T, pH, Cond.E	quarterly	2019-2020
<b>Sw17</b>	209.763	46.138988	9.527414	Hgw, T, pH, Cond.E, MI	quarterly	2019-2020
<b>Sw18</b>	203.226	46.150792	9.486272	Hgw, T, pH, Cond.E, MI	quarterly	2019-2020
<b>Sw19</b>	199.074	46.149654	9.412463	Hsw, T, pH, Cond.E	quarterly	2019-2020

## 2.9. References

- Agliardi, F., Crosta, G. B., Frattini, P., & Malusà, M. G. (2013). Giant non-catastrophic landslides and the long-term exhumation of the European Alps. *Earth and Planetary Science Letters*, 365, 263-274.
- Aili, T., Soncini, A., Bianchi, A., Diolaiuti, G., D'Agata, C., & Bocchiola, D. (2019). Assessing water resources under climate change in high-altitude catchments: A methodology and an application in the Italian Alps. *Theoretical and Applied Climatology*, 135(1), 135-156.
- Allen, R. G., Pereira, L. S., Raes, D., & Smith, M. (1998). *Crop evapotranspiration-Guidelines for computing crop water requirements-FAO Irrigation and drainage paper 56*. Fao, Rome, 300(9), D05109.
- Aster, R. C., Borchers, B., & Thurber, C. H. (2005). *Parameter estimation and inverse problems elsevier*. New York.
- Bayer, P., Huggenberger, P., Renard, P., & Comunian, A. (2011). Three-dimensional high resolution fluvio-glacial aquifer analog: Part 1: Field study. *Journal of Hydrology*, 405(1-2), 1-9.
- Bayer, P., Comunian, A., Höyng, D., & Mariethoz, G. (2015). High resolution multi-facies realizations of sedimentary reservoir and aquifer analogs. *Scientific data*, 2(1), 1-10.
- Beck, H. E., Zimmermann, N. E., McVicar, T. R., Vergopolan, N., Berg, A., & Wood, E. F. (2018). Present and future Köppen-Geiger climate classification maps at 1-km resolution. *Scientific data*, 5(1), 1-12.
- Bini, A., Buoncristiani, J. F., Couterrand, S., Ellwanger, D., Felber, M., Florineth, D., ... & Schoeneich, P. (2009). *Die Schweiz während des letzteiszeitlichen Maximums (LGM)*.
- Birck, M. D. (2006). *Temporal variability of riverbed hydraulic conductivity at an induced infiltration site, southwest Ohio (Doctoral dissertation, Miami University)*.
- Bocchiola, D., & Rosso, R. (2007). The distribution of daily snow water equivalent in the central Italian Alps. *Advances in water resources*, 30(1), 135-147.
- Bocchiola, D., & Groppelli, B. (2010). Spatial estimation of Snow Water Equivalent at different dates within the Adamello Park of Italy. *Cold regions science and technology*, 63(3), 97-109.
- Bocchiola, D., Mihalcea, C., Diolaiuti, G., Mosconi, B., Smiraglia, C., & Rosso, R. (2010). Flow prediction in high altitude ungauged catchments: a case study in the Italian Alps (Pantano Basin, Adamello Group). *Advances in Water Resources*, 33(10), 1224-1234.
- Cairns, D. W. (2014). *Simulation of groundwater flow in mountain watersheds (Doctoral dissertation, Lethbridge, Alta.: University of Lethbridge, Dept. of Geography)*.
- Calver, A. (2001). Riverbed permeabilities: Information from pooled data. *Groundwater*, 39(4), 546-553.

- Carelli, M., Ceriani, M., & Valbuzzi, E. (2007). Analisi del dissesto da frana in Lombardia. Rapporto sulle Frane in Italia: Progetto IFFI metodologia, risultati e rapporti regionali; Trigila, A., Ed.
- Cavallin, A., Baroni, C., Bini, A., Carton, A., Marchetti, M., Orombelli, G., ... & Zanchi, A. (1997). Geomorphology of the central and southern Alps. In Fourth International Conference on Geomorphology (Vol. 3, No. T2, pp. 13-47). Comitato Glaciologico Italiano.
- Celico, P. (1988). Prospezioni idrogeologiche (vol. 1 e 2). Liguori Ed., Napoli.
- Chen, X., Dong, W., Ou, G., Wang, Z., & Liu, C. (2013). Gaining and losing stream reaches have opposite hydraulic conductivity distribution patterns. *Hydrology and Earth System Sciences*, 17(7), 2569-2579.
- Cochand, M., Molson, J., Barth, J. A. C., van Geldern, R., Lemieux, J. M., Fortier, R., & Therrien, R. (2020). Rapid groundwater recharge dynamics determined from hydrogeochemical and isotope data in a small permafrost watershed near Umiujaq (Nunavik, Canada). *Hydrogeology Journal*, 28(3), 853-868.
- Comunian, A., Renard, P., Straubhaar, J., & Bayer, P. (2011). Three-dimensional high resolution fluvio-glacial aquifer analog—Part 2: Geostatistical modeling. *Journal of hydrology*, 405(1-2), 10-23.
- Crippa, C., Franzosi, F., Zonca, M., Manconi, A., Crosta, G. B., Dei Cas, L., & Agliardi, F. (2020). Unraveling spatial and temporal heterogeneities of very slow rock-slope deformations with targeted DInSAR analyses. *Remote Sensing*, 12(8), 1329.
- Crippa, C., Valbuzzi, E., Frattini, P., Crosta, G. B., Spreafico, M. C., & Agliardi, F. (2021). Semi-automated regional classification of the style of activity of slow rock-slope deformations using PS InSAR and SqueeSAR velocity data. *Landslides*, 1-19.
- Crosta, G. B., & Frattini, P. (2004). Controls on modern alluvial fan processes in the central Alps, northern Italy. *Earth Surface Processes and Landforms: The Journal of the British Geomorphological Research Group*, 29(3), 267-293.
- D'Agata, C., Bocchiola, D., Soncini, A., Maragno, D., Smiraglia, C., & Diolaiuti, G. A. (2018). Recent area and volume loss of Alpine glaciers in the Adda River of Italy and their contribution to hydropower production. *Cold Regions Science and Technology*, 148, 172-184.
- De Caro, M., Perico, R., Crosta, G. B., Frattini, P., & Volpi, G. (2020). A regional-scale conceptual and numerical groundwater flow model in fluvio-glacial sediments for the Milan Metropolitan area (Northern Italy). *Journal of Hydrology: Regional Studies*, 29, 100683.
- De Carvalho, P. R. M., da Costa, J. F. C. L., Rasera, L. G., & Varella, L. E. S. (2017). Geostatistical facies simulation with geometric patterns of a petroleum reservoir. *Stochastic environmental research and risk assessment*, 31(7), 1805-1822.
- De Finis, E., & Bini, A. (2014). Control of fans dominated by landslide on the quaternary sequence in Alpine valley (Valtellina, Northern Italy). In *Conference Proceedings of the 14th*

GeoConference on Science and Technologies in Geology, Exploration and Mining. Albena (Bulgaria). II (pp. 219-226).

De Finis, E., Gattinoni, P., Marchi, L., & Scesi, L. (2017, May). Modeling debris flows in anomalous basin-fan systems. In *Workshop on World Landslide Forum* (pp. 601-609). Springer, Cham.

De Finis, E., Gattinoni, P., Marchi, L., & Scesi, L. (2018). Anomalous Alpine fans: From the genesis to the present hazard. *Landslides*, 15(4), 683-694.

De Franco, R., Biella, G., Caielli, G., Berra, F., Guglielmin, M., Lozej, A., ... & Sciunnach, D. (2009). Overview of high resolution seismic prospecting in pre-Alpine and Alpine basins. *Quaternary International*, 204(1-2), 65-75.

Diersch, H. J. G. (2013). *FEFLOW: finite element modeling of flow, mass and heat transport in porous and fractured media*. Springer Science & Business Media.

Dochartaigh, B. Ó., Archer, N. A. L., Peskett, L., MacDonald, A. M., Black, A. R., Auton, C. A., ... & Bonell, M. (2019). Geological structure as a control on floodplain groundwater dynamics. *Hydrogeology Journal*, 27(2), 703-716.

Doherty, J. E., & Hunt, R. J. (2010). *Approaches to highly parameterized inversion: a guide to using PEST for groundwater-model calibration* (Vol. 2010). Reston: US Department of the Interior, US Geological Survey.

Fleckenstein, J. H., Niswonger, R. G., & Fogg, G. E. (2006). River-aquifer interactions, geologic heterogeneity, and low-flow management. *Groundwater*, 44(6), 837-852.

Fox, A., Packman, A. I., Boano, F., Phillips, C. B., & Arnon, S. (2018). Interactions between suspended kaolinite deposition and hyporheic exchange flux under losing and gaining flow conditions. *Geophysical Research Letters*, 45(9), 4077-4085.

Grämiger, L. M., Moore, J. R., Gischig, V. S., Ivy-Ochs, S., & Loew, S. (2017). Beyond debulking: Mechanics of paraglacial rock slope damage during repeat glacial cycles. *Journal of Geophysical Research: Earth Surface*, 122(4), 1004-1036.

Heinz, J., & Aigner, T. (2003). Hierarchical dynamic stratigraphy in various Quaternary gravel deposits, Rhine glacier area (SW Germany): implications for hydrostratigraphy. *International Journal of Earth Sciences*, 92(6), 923-938.

Ivy-Ochs, S., Kerschner, H., Reuther, A., Preusser, F., Heine, K., Maisch, M., ... & Schlüchter, C. (2008). Chronology of the last glacial cycle in the European Alps. *Journal of Quaternary Science: Published for the Quaternary Research Association*, 23(6-7), 559-573.

Jarman, D., Agliardi, F., & Crosta, G. B. (2011). Megafans and outsize fans from catastrophic slope failures in Alpine glacial troughs: the Malser Haide and the Val Venosta cluster, Italy. *Geological Society, London, Special Publications*, 351(1), 253-277.

Jasechko, S., Seybold, H., Perrone, D., Fan, Y., & Kirchner, J. W. (2021). Widespread potential loss of streamflow into underlying aquifers across the USA. *Nature*, 591(7850), 391-395.

- Martin, S., Klingler, S., Dietrich, P., Leven, C., & Cirpka, O. A. (2020). Structural controls on the hydrogeological functioning of a floodplain. *Hydrogeology Journal*, 28(8), 2675-2696.
- Mele, M., Bersezio, R., Bini, A., Bruno, M., Giudici, M., & Tantardini, D. (2021). Subsurface profiling of buried valleys in central alps (northern Italy) using HVSR single-station passive seismic. *Journal of Applied Geophysics*, 193, 104407.
- Naganna, S. R., Deka, P. C., Ch, S., & Hansen, W. F. (2017). Factors influencing streambed hydraulic conductivity and their implications on stream–aquifer interaction: a conceptual review. *Environmental Science and Pollution Research*, 24(32), 24765-24789.
- Peel, M. C., Finlayson, B. L., & McMahon, T. A. (2007). Updated world map of the Köppen-Geiger climate classification. *Hydrology and earth system sciences*, 11(5), 1633-1644.
- Prevati, A., De Caro, M., & Crosta, G. B. (2020). Hydro-stratigraphic datasets for the reconstruction of a large scale 3D FEM numerical model in the Milan metropolitan area (northern Italy). *Data in Brief*, 33, 106541.
- Preziosi-Ribero, A., Packman, A. I., Escobar-Vargas, J. A., Phillips, C. B., Donado, L. D., & Arnon, S. (2020). Fine sediment deposition and filtration under losing and gaining flow conditions: A particle tracking model approach. *Water Resources Research*, 56(2), e2019WR026057.
- Remy, N., Boucher, A., & Wu, J. (2009). *Applied geostatistics with SGeMS: A user's guide*. Cambridge University Press.
- Riva, F., Agliardi, F., Amitrano, D., & Crosta, G. B. (2018). Damage-based time-dependent modeling of paraglacial to postglacial progressive failure of large rock slopes. *Journal of Geophysical Research: Earth Surface*, 123(1), 124-141.
- Rubel, F., Brugger, K., Haslinger, K., & Auer, I. (2017). The climate of the European Alps: Shift of very high resolution Köppen-Geiger climate zones 1800–2100. *Meteorologische Zeitschrift*, 26(2), 115-125.
- Ryder, J. M. (1971). The stratigraphy and morphology of para-glacial alluvial fans in south-central British Columbia. *Canadian Journal of Earth Sciences*, 8(2), 279-298.
- Schmid SM (2017) On the Insubric line and the Southern Steep Belt of the Penninic nappes in the Ticino area (including 2 excursion guides). *Swiss Bull Appl Geol* 22(2):69–89
- Schubert, J. (2006). Experience with riverbed clogging along the Rhine River. In *Riverbank filtration hydrology* (pp. 221-242). Springer, Dordrecht.
- Scotti, R., Brardinoni, F., & Crosta, G. B. (2014). Post-LIA glacier changes along a latitudinal transect in the Central Italian Alps. *The Cryosphere*, 8(6), 2235-2252.
- Singleton, M. J., & Moran, J. E. (2010). Dissolved noble gas and isotopic tracers reveal vulnerability of groundwater in a small, high-elevation catchment to predicted climate changes. *Water Resources Research*, 46(10).
- Somers, L. D., & McKenzie, J. M. (2020). A review of groundwater in high mountain environments. *Wiley Interdisciplinary Reviews: Water*, 7(6), e1475.

Spreafico, M. C., Agliardi, F., Andreozzi, M., Cossa, A., & Crosta, G. B. (2020, May). Large slow rock-slope deformations affecting hydropower facilities. In EGU General Assembly Conference Abstracts (p. 8288).

Stewardson, M. J., Datry, T., Lamouroux, N., Pella, H., Thommeret, N., Valette, L., & Grant, S. B. (2016). Variation in reach-scale hydraulic conductivity of streambeds. *Geomorphology*, 259, 70-80.

Strebelle, S. (2002). Conditional simulation of complex geological structures using multiple-point statistics. *Mathematical geology*, 34(1), 1-21.

Tang, Q., Schilling, O. S., Kurtz, W., Brunner, P., Vereecken, H., & Hendricks Franssen, H. J. (2018). Simulating Flood-Induced Riverbed Transience Using Unmanned Aerial Vehicles, Physically Based Hydrological Modeling, and the Ensemble Kalman Filter. *Water resources research*, 54(11), 9342-9363.

Viaroli, S., Mastroiello, L., Lotti, F., Paolucci, V., & Mazza, R. (2018). The groundwater budget: a tool for preliminary estimation of the hydraulic connection between neighboring aquifers. *Journal of hydrology*, 556, 72-86.

# Chapter 3:

## Water balance in Alpine catchments by Sentinel data

### 3.1. Introduction

Understanding the storage dynamics of the groundwater resources represents one of the major contemporary challenges for water management (Bales et al., 2006; Sheffield et al., 2018; Sorg et al., 2012; Taylor et al., 2013). This is especially true for mountain areas that are recognized to be the source of much of the world's surface water supply (Fayad et al., 2017; Viviroli et al., 2007). In the Alpine zone, the snow-dominated catchments show a high potential of recharge due to a large precipitation and the relatively small evapotranspiration (Wilson and Guan, 2004; Hayashi, 2020). However, climate change affects surface processes such as runoff, snowpack dynamics, or evapotranspiration (Clow, 2010; Cochand et al., 2019; Rodell et al., 2018), conditioning water availability.

A major issue for alpine catchments is the heterogeneous distribution and the rapid dynamics of hydrological processes owing to the local-scale variability of meteorological conditions and the terrain complexity. These prevent a spatial and temporal efficient input-data collection, even considering the relative scarcity of hydro-meteorological stations in such low-population areas. Accordingly, these limitations in data acquisition introduce significant approximations and uncertainty (West et al., 2019).

In the past 30 years, the advance in the ability to observe some hydrological phenomena from space has given new opportunities for their monitoring (Brunner et al., 2007; Lettenmaier et al., 2015; McCabe et al., 2017; Tang et al., 2009). At watershed and regional scales, remote sensing products are deemed as a complementary source of information to in situ monitoring networks and, in many cases, the only feasible source (Sheffield et al., 2018). Except for a few studies that approached the estimation of groundwater storage in the alpine zone by using remote sensing data (Bibi et al., 2019; Gemitzi et al., 2017), most of the satellite-based methods proposed to calculate the main components of the water balance (i.e., evapotranspiration and snow water equivalent) are poorly suited for large alpine catchments. These methods do not allow capturing topography variability because of the low spatial resolution or are still impracticable in large catchments (Dozier et al., 2016).

For evapotranspiration (ET), satellite data are used in several methods and models (Zhang et al., 2016). MOD16, a physical model based on the Penman-Monteith's equation, is routinely applied to generate a global ET dataset (MODIS/Terra Net Evapotranspiration 8-Day L4 Global

500 m) by using NASA MODIS (MODerate Resolution Imaging Spectroradiometer) data. This dataset provides an 8-day averaged value of ET with a spatial resolution of 500 m. Other satellite-based approaches developed in the last two decades, such as METRIC (Mapping Evapotranspiration with Internalized Calibration, Allen et al., 2007), SSEBop (Simplified Surface Energy Balance; Senay et al., 2013), ALEXI/DisALEXI (Atmosphere–Land Exchange Inverse, Anderson et al., 1997, 2007), fall into the category of the surface energy balance (SEB). In these models, ET is linked to Land Surface Temperature (LST) derived from thermal infrared (TIR) of Meteosat, MODIS and Landsat remote sensing dataset (Bhattarai et al., 2016; Castelli et al., 2018). The thermal input affects the quality and the spatial and temporal resolution of these products (Cammalleri et al., 2014). In particular, the coarse resolution remains insufficient to fulfil the requirements of applications in heterogeneous areas, such as the mountain regions (Cammalleri et al., 2014; Guzinski et al., 2019; Kustas et al., 2004).

The spatially-distributed quantification of snow depth and snow water equivalent (SWE) is still problematic in mountain hydrology (Dozier et al., 2016; Liu et al., 2020). One of the most consistent methods is the spatial interpolation of local measurements of SWE, constrained by remotely sensed snow cover area (SCA) (Dozier et al., 2016). This method is physically realistic but is affected by a high uncertainty in the unrepresented areas and influenced by the location of the monitoring sites on flat terrain (Bavera et al., 2009; Rice et al., 2011). Another method is the backward reconstruction of the SWE accumulation time series, with a high spatial resolution (10-30m) and based on daily snowmelt and SCA changes from the last significant snowfall (Jonas et al., 2009; Liu et al., 2020). This method is still impracticable on extensive catchments for its computational load (Dozier et al., 2016). The passive microwave is at the basis of the available SWE maps (spatial resolution of 10-25km) of the northern hemisphere, such as NASA/JAXA's AMSR-E/Aqua Daily L3 Global Snow Water Equivalent EASE-Grids (AE\_DySno) (Tedesco et al., 2004), NSIDC's Global EASE-Grid 8-day Blended SSM/I and MODIS Snow Cover (NSIDC-0321) (Brodzik et al., 2007). The use of the passive microwave has the advantage in the day-night all-weather capability, but it is strongly affected by the texture of the snow and the content of liquid water in the snowpack.

Recently, new opportunities for an accurate, operational, and multiply-scale estimation of the hydrological parameters emerge through Sentinel data (Guzinski et al., 2019; Veloso et al., 2017). These new freely and globally available data are collected in the Sentinel missions,

launched in the last 6 years by ESA, acquiring frequent observations from a combination of optical, thermal and microwave sensors with high spatial and temporal resolutions (Guzinski et al., 2019; Malenovský et al., 2012; West et al. 2019).

We take advantage of these recent developments to address the previously identified issues concerning water balances in alpine areas. The main objectives of this study are (i) to propose a Sentinel-based methodology to quantify the seasonal groundwater storage in a snow-dominated catchment, and (ii) to apply the methodology to an extensive alpine catchment (Valtellina Valley, North Italy) for two hydrologic years (March 2018 to February 2020). For these purposes, we quantified the seasonal groundwater storage volume according to the residual water budget method (Healy et al., 2010), starting from multi-sensory Sentinel data. In particular, we tested new promising methods for the estimation of ET (Guzinski et al., 2020) and snow depth (Lievens et al., 2019), and we investigated the inherent uncertainties. To assess the effect of physiographic characteristics (altitude, slope, and exposition) and seasonality on the storage quantification, we analysed the root mean square error (RMSE) concerning available ground truth data or to other databases.

## 3.2. Methods

### 3.2.1. Groundwater storage dynamics

The dynamics of water during the hydrologic year were investigated with the residual water-budget method (Healy et al., 2010), where all the terms of the governing equation are independently measured or estimated, and groundwater storage ( $\Delta S^{gw}$ , [ $m^3/day$ ]) is set equal to the residual. The groundwater storage volumes were quantified for 3 different phases of the hydrologic year: (1) snowmelt; (2) snow-free; (3) snow accumulation.

For a watershed, considering snowpack (*snow*), surface water (*sw*), and water in the unsaturated (*uz*) and saturated (*gw*) zone, the water budget corresponds to the following equation:

$$P + Q_{on}^{sw} + Q_{on}^{gw} = ET^{sw} + ET^{gw} + ET^{uz} + S^{snow} + \Delta S^{snow} + \Delta S^{sw} + \Delta S^{gw} + \Delta S^{uz} + Q_{off}^{gw} + Q_{off}^{sw} + Abs \quad (3.01)$$

where P is the precipitation [ $m^3/day$ ],  $Q_{on}$  and  $Q_{off}$  are the water flow [ $m^3/day$ ] into and out from surface water and groundwater systems, ET is the evapotranspiration [ $m^3/day$ ],

$S^{snow}$  is the snow sublimation [ $m^3/day$ ],  $\Delta S$  is the water storage, and  $Abs$  is the anthropic abstraction [ $m^3/day$ ]. The volume of each component was calculated considering the entire area of the catchment.

In an extensive snow-dominated catchment, the rainfall, given by the difference between the total precipitation ( $P$ ) and the water stored in the snow-pack (positive  $\Delta S(+)^{snow}$ ), and the snowmelt (negative  $\Delta S(-)^{snow}$ ), are the two main sources of groundwater recharge during the hydrologic year. Meanwhile, the depletion of water is caused by evapotranspiration ( $ET = ET^{sw} + ET^{uz} + ET^{gw}$ ) and sublimation ( $S^{snow}$ ), the main river outflow from the catchment ( $Q_{off}^{sw}$ ) and by the abstraction ( $Abs$ ). The storage of the surface-water ( $\Delta S^{sw}$ ) and of the unsaturated zone ( $\Delta S^{uz}$ ), the flow into the superficial system ( $Q_{on}^{sw}$ ), the flows into and out of the groundwater system ( $Q_{on}^{gw}$  and  $Q_{off}^{gw}$ ) were assumed negligible given the topographical and geological setting of the catchment. For similar Alpine sites, sublimation has been estimated to be about 10% of the SWE, with lower values during the snowmelt period (Cochand et al., 2019; DeWalle & Rango, 2008; Hood et al., 1999; Strasser et al., 2008). In this study, sublimation was neglected because it cannot be captured with the Sentinel-based ET estimates. A slight overestimation of the groundwater storage is thus expected.

The volume of groundwater storage ( $\Delta S^{gw}$ , [ $m^3$ ]) was estimated with the water budget equation as following:

$$\Delta S^{gw} = (P + \Delta S(-)^{snow}) - (ET + \Delta S(+)^{snow} + Q_{off}^{sw} + Abs) \quad (3.02)$$

In the present work, the  $Q_{off}^{sw}$  at the outlet point of the catchment and the  $Abs$  from the public wells and springs data were extracted from available in-situ database. The ERA5 reanalysis, produced by the European Centre for Medium-Range Weather Forecasts (ECMWF) (Hersbach et al., 2020), was selected to the quantification of daily total  $P$  (liquid and frozen water). This dataset provides reasonable spatial ( $0.25^\circ \times 0.25^\circ$ ) and temporal variability of different atmospheric variables through the assimilation of large amounts of ground-based observations, atmospheric data and remote-sensing data. In particular, the precipitation data in regions such as in the North America and Europe has a high potential for applicability (Jiang et al., 2021; Keller and Wahl, 2021; Tarek et al., 2020). Meanwhile, as described in the next

paragraphs  $\Delta S^{snow}$  and  $ET$  were quantified with SWE and ET the spatial-time-series achieved with Sentinel-based methods.

The estimates of the water balance components are affected by many sources of uncertainty (Cochand et al., 2019; Sattary et al., 2002; Silva et al., 2018). Consistently with the main purpose of the paper, only the “additional” uncertainty [%] derived from the use of Sentinel-based methods in the estimation of groundwater storage was explicitly quantified as:

$$u = \sqrt{u_{ET}^2 + u_{SWE}^2} \quad (3.03)$$

In which  $u_{ET}$ , [%], and  $u_{SWE}$ , [%], are the values of uncertainty calculated as RMSE calculated for all available monitoring sites.

### 3.2.2. Evapotranspiration

A new method based on the synergistic use of Sentinel 2 and 3 satellite data was explored for the estimation of evapotranspiration (Guzinski et al., 2020, 2019). This method, implemented in an open-source Python library in the “Sentinels for Evapotranspiration (SEN-ET)” project (by DHI GRAS, IRTA and Sandholt ApS), aims at modelling evapotranspiration at the highest possible spatial resolution without sacrificing the output accuracy. In particular, we used the plugin of the SEN-ET algorithms (<http://esa-sen4et.org/outputs/software>) in the SNAP (ESA Sentinel Application Platform 7.0.0) graphical user interface (GUI). This plugin is designed to work with the products of the second level of processing for SLSTR and MSI instrument data, respectively onboard the Sentinel-3 and Sentinel-2, available for the download from the Copernicus Open Access Hub (COAH - <https://scihub.copernicus.eu>).

The model requires as input morphological (STRM DEM), land-use (ESA-CCI-LC 2015, available at <http://maps.elie.ucl.ac.be/CCI/viewer>) and meteorological (ECMWF ERA-5 dataset) data. In particular, the plugin enables to reanalyse the meteorological ERA-5 products using the DEM, to obtain the air temperature, vapour pressure, air pressure, wind speed, clear-sky incoming solar radiation, and average daily solar irradiance data.

The method involves two steps: the thermal sharpening and the land-surface energy flux model. The former allows to obtain high-resolution (20 m) Land Surface Temperature (LST) maps using a multivariate regression model with the biophysical and topographic information and exposure maps at the S3 overpass time (Gao et al., 2012; Guzinski et al., 2020). To ensure

the conservation of energy and reduce the residual bias, a bias-correction between the two thermal images with different spatial resolutions is provided within the algorithm. The land-surface energy flux model applied in this study is based on the Two-Source Energy Balance (TSEB) model (Colaizzi et al., 2012; Guzinski et al., 2020; Norman et al., 1995), which splits the surface energy fluxes between two sources, canopy and soil, derived from a measurement of the bulk surface radiometric temperature. As a result, four instantaneous land-surface energy fluxes at the time of Sentinel-3 overpass are produced by means of the Priestley-Taylor's approximation: sensible heat flux ( $H$ , [ $W/m^2$ ]), latent heat flux ( $LE$ , [ $W/m^2$ ]), ground heat flux ( $G$ , [ $W/m^2$ ]) and net radiation ( $R_n$ , [ $W/m^2$ ]):

$$R_n - G = H + LE \quad (3.04)$$

Finally, the daily evapotranspiration ( $ET$ , [ $mm/day$ ]) is extrapolated by the ratio between the instantaneous latent heat flux and daily solar irradiances [ $J/m^2$ ].

However, in order to evaluate the generated maps in extensive mountain areas, a comparison with two different datasets was performed. The first dataset was obtained by applying the FAO Penman-Monteith's equation (Allen et al., 1998) on the data from the meteorological stations, located in crop fields or grasslands along the floodplain. The second was the MOD16A2 global evapotranspiration (MODIS/Terra Snow Cover 8-Day L3 Global 500m SIN Grid, Version 6) dataset. The correlation coefficient ( $r$ ) and root mean square error (RMSE) were used to assess the goodness of fit of the satellite to the ground-based evapotranspiration estimated.

Finally, the numerical integration of the total daily evapotranspiration volume ( $ET_{daily}$ , [ $m/day$ ]) over the entire catchment,  $A$  [ $m^2$ ], was used to calculate the  $ET_i$ , [ $m^3$ ] for each  $i$ -th phase of the hydrologic year, as:

$$ET_i = \int_{t_0}^{t_f} (ET_{daily} \times A) dt \quad (3.05)$$

Where  $t_0$  and  $t_f$  are the time at the beginning and at the end of the  $i$ -th hydrologic phase of the year, respectively.

Due to the unavailability of in-situ ground-truth data, the uncertainty of the ET estimation,  $u_{ET}$ , corresponds to that of the SEN-ET method (Guzinski et al., 2020).

### 3.2.3. Snow Water Equivalent

The snow contribution to the hydrologic balance was quantified from the time-series of the total SWE calculated at the catchment scale. As described in equation (6), the  $\Delta S^{snow} [m^3]$ , of each  $i$ -th phase of the hydrologic year is the sum of difference for each time step  $t(i)$  between the SWE,  $[m/day]$ , at time  $t$  and at time  $t-1$  and multiplied for the area,  $A [m^2]$ , of the catchment:

$$\Delta S^{snow}_i = \sum_{t(i)} (SWE_t - SWE_{t-1}) \times A \quad (3.06)$$

Where a positive value,  $\Delta S(+)^{snow} [m^3/day]$  indicates that water is stored in the snow-pack at the time step  $t$ ; while a negative value,  $\Delta S(-)^{snow} [m^3/day]$ , is representative of a snowmelt process that contributes to the groundwater recharge.

The SWE time-series were estimated with two different methods for either the snow accumulation phase or the snow melting phase.

For the snow accumulation phase, the 30-m resolution SWE maps were calculated starting from Sentinel-based data for snow depth (SD,  $[m]$ ) and spatially-distributed snow/water density ratio ( $\rho_b/\rho_w$ ,  $[-]$ ), as:

$$SWE = SD * \frac{\rho_b}{\rho_w} \quad (3.07)$$

where  $\rho_b [kg/m^3]$  and  $\rho_w [kg/m^3]$  are the snow bulk density and the water density, respectively.

The  $\rho_w$  was set =  $1000 kg/m^3$ . The spatially-distribute snow density ( $\rho_b$ ) maps were achieved by applying an empirical relationship on the SRTM DEM provided by NASA JPL at a resolution of 1 arc-second (approximately 30 m at the latitude of the case study). Among the several empirical relationships (Jonas et al., 2009; Valt et al., 2018), we adopted the linear regression equation of Bavera and De Michele (2009) that has been proposed for a sub-catchment inside the case study area. This relationship considers the altitude,  $z [m a. s. l]$ , the number of days after 1st of September,  $D [d]$ , and the local slope,  $I [^\circ]$ , as predictors of the  $\rho_b$ :

$$\rho_b = 0.038z + 0.649D - 1.434I + 145.03 \quad R^2 = 0.43 \quad (3.08)$$

The SD dataset is produced by the C-SNOW project (<https://ees.kuleuven.be/project/c-snow>), which retrieves the snowpack depth from cross-polarized backscatter measurements of the Sentinel-1 C-band (5.4 GHz, 10m) with a revisit time of 6 days, and with a good accuracy during the snow accumulation phase. The algorithm details are presented in Lievens et al. (2019). The C-SNOW dataset includes northern hemisphere maps of the snow-depth at 1 km<sup>2</sup> spatial resolution, starting from September 2016. The SD maps have been resampled with a bi-cubic resampling technique to obtain the same resolution of the snow density maps.

To improve the accuracy along with the transition from snow-covered to snow-free areas, a SCA mask was applied on the SD maps for each month of the accumulation phase. The masks were performed by processing Sentinel-2 images (20 m resolution) with cloud-free pixels classified as snow when:

$$NDSI < 0.4 \text{ and } \rho_{red} < 0.2 \quad (3.09)$$

where NDSI is the Normalized Difference Snow Index, [-], and  $\rho_{red}$  [-] is the value of the red band (B4). The thresholds were set conservatively high to avoid false detection.

For the melting phase, the 30-m resolution SWE maps were calculated by using a temperature index method (Rango and Martinec, 1979). The method is based on the high correlation (0.96, Braithwaite and Olesen, 1989) between air temperature and snowmelt and consists in the computation of the daily snowmelt rate,  $M_t$ , [m/day] as a function of the degree day factor,  $DDF$  [m/day/°C], the mean daily air temperature,  $T_d$  [°C], and the temperature threshold that controls the occurrence of melting,  $T_b$  [°C]:

$$M_t = \begin{cases} DDF(T_d - T_b), & T_d > T_b \\ 0, & T_d \leq T_b \end{cases} \quad (3.10)$$

The  $T_b$  was set to 0°C (He et al., 2014) and the  $T_d$  was derived from the air temperature ERA-5 reanalysis. The empirical DDF values were obtained as the ratio between measured changes in SWE and the difference between daily temperature and the threshold value. Considering a linear relationship with the altitude (Hock 2003), the DDF values were spatially interpolated by Ordinary Co-Kriging.

The estimation of SWE at time  $t$  is completed with an iterative routine for each grid point, as follows:

$$SWE_t = SWE_{t-1} - M_t \quad (3.11)$$

Due to the unavailability of in situ SWE data, the uncertainty in the total SWE estimation,  $u_{SWE}$ , was assessed by considering the NRMSE of the snow depth, calculated for all available monitoring sites and normalized with respect to the average. In addition, the correlation coefficient ( $r$ ) between the measured and the estimated SD values, and the dependence of the RMSE on physiographic parameters (altitude, slope, and exposure) and on the seasonal conditions were examined.

### 3.3. Analysis and Results

#### 3.3.1. Evapotranspiration estimation

Spatial distribution of evapotranspiration was produced for the 2018-2019 and the 2019-2020 hydrologic year with a monthly average of 8 maps using:

- 69 Sentinel-2A and Sentinel-2B MSIL2A images, selected from the T32TNS and T32TPS tiles with a maximum cloud cover percentage of 20%. The downloaded data of the two tiles were extracted in the area of interest and merged into 34 images.
- 277 Sentinel-3A SL\_2\_LST images with sensing data in the morning. After the extraction into the area of interest, 141 images were manually selected by considering a maximum cloud cover percentage of 20%.

The uncertainty ( $u_{ET}$ ) of the method, considering the RMSE of instantaneous  $LE$  in agricultural areas, is 30% (Guzinski et al., 2020).

During the first part of the hydrologic year, the results show an ET increase from March to June, with mean values during the first year of  $3.9 \pm 1.3$  mm/day and  $4.0 \pm 1.0$  mm/day for the grassland and the forest cover, respectively (**Figure 3.1a**), and  $4.7 \pm 1.0$  mm/day and  $4.4 \pm 0.8$  mm/day for the second year. An anomalous spike of evapotranspiration is observed at the end of April 2018 (**Figure 3.3**). The maximum ET value is recognized at the beginning of the snow-free phase: the peaks were recorded on the 18 July 2018, with mean values of  $5.2 \pm 0.9$  mm/day and  $5.8 \pm 0.7$  mm/day for the grassland and the forest cover, respectively (**Figure 3.1b**), and on the 29 June 2019, with mean values of  $5.4 \pm 1.0$  mm/day and  $6.1 \pm 0.8$  mm/day. Successively, the ET shows a strong decrease until the end of October, with minimum values in the two years equal to  $1.5 \pm 0.5$  and  $2.0 \pm 0.4$  mm/day for the grassland and of  $1.8 \pm 0.4$  and  $2.2 \pm 0.3$  mm/day for the forest area (**Figure 3.1c**). During the snow accumulation phase, the results show a minimum value of ET ( $\approx 0.01$  mm/day). Moreover, due to an increase of the snow-cover area and the decrease in average temperature, the ET is null over a percentage of area that increases, up to a maximum of 17% in February. At the end of February (**Figure 3.1d**), the ET starts to increase up to  $1.5 \pm 0.8$  and  $2.0 \pm 0.4$  mm/day and of  $1.1 \pm 0.8$  and  $2.1 \pm 0.3$  mm/day for the grassland and the forest cover, respectively, for each hydrologic year.

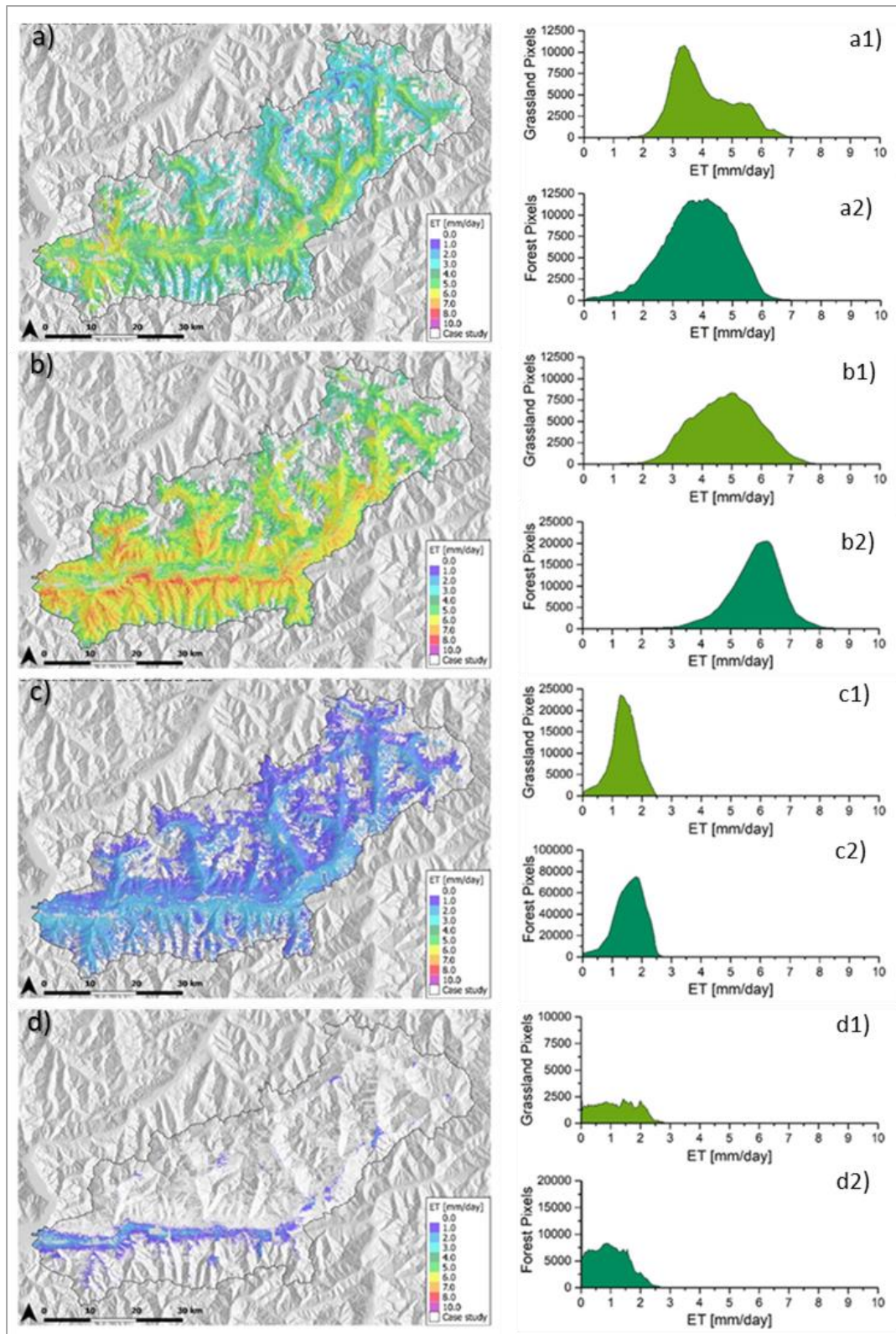


Figure 3.1: Maps of daily evapotranspiration (ET) during four representative days in different seasons of the 2018-2019 hydrologic year and corresponding evapotranspiration frequency distributions in grassland and forest areas. a) 15 June 2018; b) 18 July 2018; c) 19 October 2018; d) 21 February, 2019.

The comparison among the ET values estimated with the Sentinel and Modis data and the ground-based data at 6 locations is shown in **Figure 3.2**. The results indicate a significant correlation ( $p < 0.05$ ) with the ground-based ET for both the MOD16A2 ( $r = 0.72$ ,  $RMSE = 0.82$  mm) and the Sentinel products ( $r = 0.79$ ,  $RMSE = 1.5$  mm).

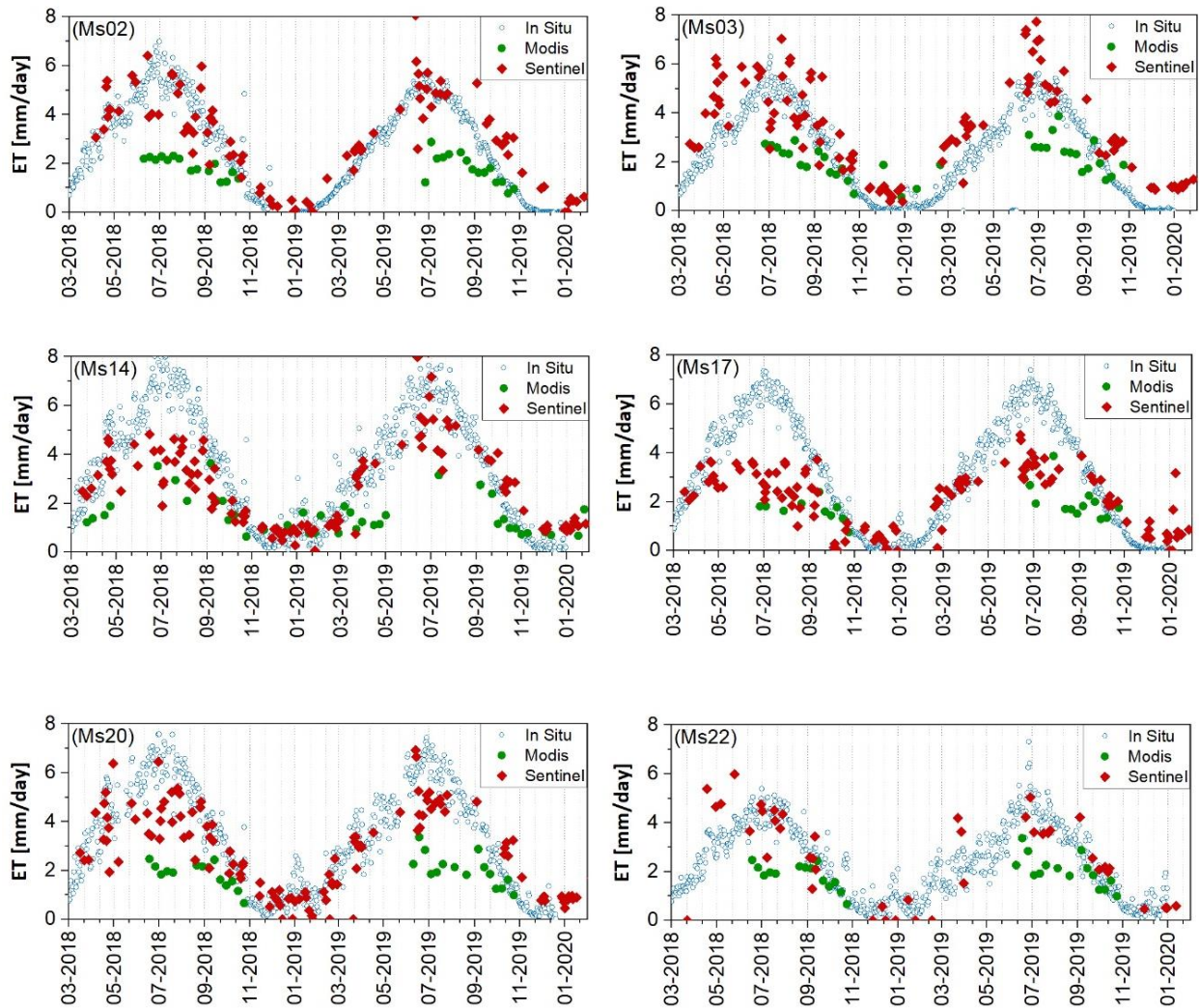


Figure 3.2: Comparison among the ET time series for the 2018–2019's and 2019–2020's hydrologic year, estimated with the Sentinel and Modis data and the ground-based data at the monitoring stations Ms02, Ms03, Ms14, Ms17, Ms20 and Ms22 (see Figure 2.2, Chapter 2).

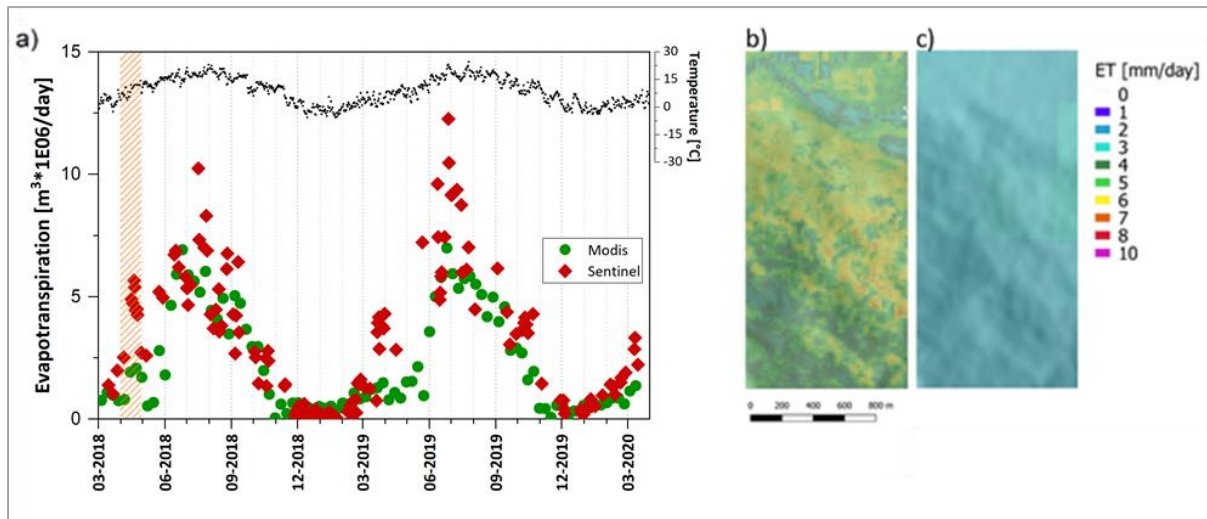


Figure 3.3: a) Time series of daily evapotranspiration volumes estimated at the basin scale with Sentinel data (red diamonds) and MODIS (green circles) data. b) and c) maps of daily ET spatial distribution on 20 April 2018 with Sentinel (b) and MODIS (c) data, showing the capability of Sentinel to recognize the temperature anomaly of April.

In addition, although a comparable total volume of evapotranspiration was observed at the catchment scale ( $10.7\text{E}+08 \text{ m}^3/\text{year}$  vs  $9.1\text{E}+08 \text{ m}^3/\text{year}$ ), the Sentinel product provides a better fitting with ground-based data during snowmelt and extreme weather conditions, instead of MODIS16A2, where a slight and smooth underestimation was generally observed (Figure 3.2 e Figure 3.3).

### 3.3.2. Snow water equivalent estimation

Based on the empirical relation of Bavera and De Michele (2009), spatial time-series of the snow densities in the Valtellina catchment was obtained. The snow-density distribution during the snow accumulation shows an average of  $240 \pm 30 \text{ kg/m}^3$  phase, and an average of  $350 \pm 30 \text{ kg/m}^3$ , with a maximum value of  $460 \text{ kg/m}^3$  at high altitude, in the snowmelt phase. The results are able to reproduce in time and space the influence of altitude and topography. In fact, at high altitudes, it tends to result in greater snow density as a consequence of generally lower temperatures, leading to a greater amount of snow and a greater possibility of compaction (Rango and Martinec, 1995).

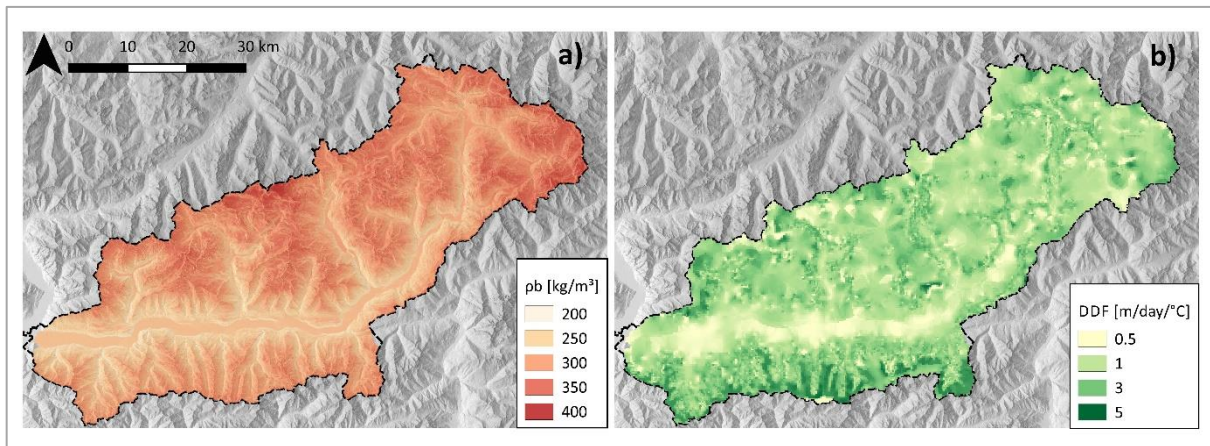


Figure 3.4: Maps of daily snow density (a) and of the DDF (b) obtained by Ordinary-Kriging.

The DDF distribution was generated with the Ordinary Co-Kriging estimation algorithm (**Figure 3.4b**). A spherical variogram was selected, with a sill value of  $2.95 \text{ (m/day/}^\circ\text{C)}^2$  and a range of 10 km, which is approximately 10% of the horizontal model domain size. The estimation was conditioned to the altitude information, which are obtained from SRTM DEM.

The SWE products for the 2018-2019 and 2019-2020 hydrologic year consist of 420 maps at the resolution of 30 m, with weekly and daily frequencies during the snow accumulation and the snowmelt phase, respectively. **Figure 3.5** shows the SWE spatial distribution for several representative days. At the starting point of the snowmelt phase of the two hydrological years (**Figure 3.5a** and **Figure 3.5d**), the total volume of water stored in the snow was estimated equal to  $5.4\text{E}+08 \text{ m}^3$  and  $7.7\text{E}+08 \text{ m}^3$ , respectively. The snow line is located between 1,800 m a.s.l. and 2,100 m a.s.l and the mean height of the snow equivalent was estimated equal to 0.5 m, for the 2018-2019 year, and 0.8 m, for the 2019-2020 year. Snow depth values calculated with the temperature-index model confirm, for both years, a high melt rate between May and June (**Figure 3.5b** and **Figure 3.5e**), and a snow-free phase from July, in line with historical trends (Bavera et al., 2009). The first evidence of snow is observed after the first snowfall event at the end of October 2019 and at the beginning of November 2019 (**Figure 3.5c** and **Figure 3.5f**). The accumulation of the snow increases until February, when the snow line reaches the altitude of 1,800 m a.s.l. At the end of the 2019-2020 hydrologic year (**Figure 3.5g**) the mean thickness of the snow was 0.49 m and the total water volumes stored was  $4.4\text{E}+08 \text{ m}^3$ .

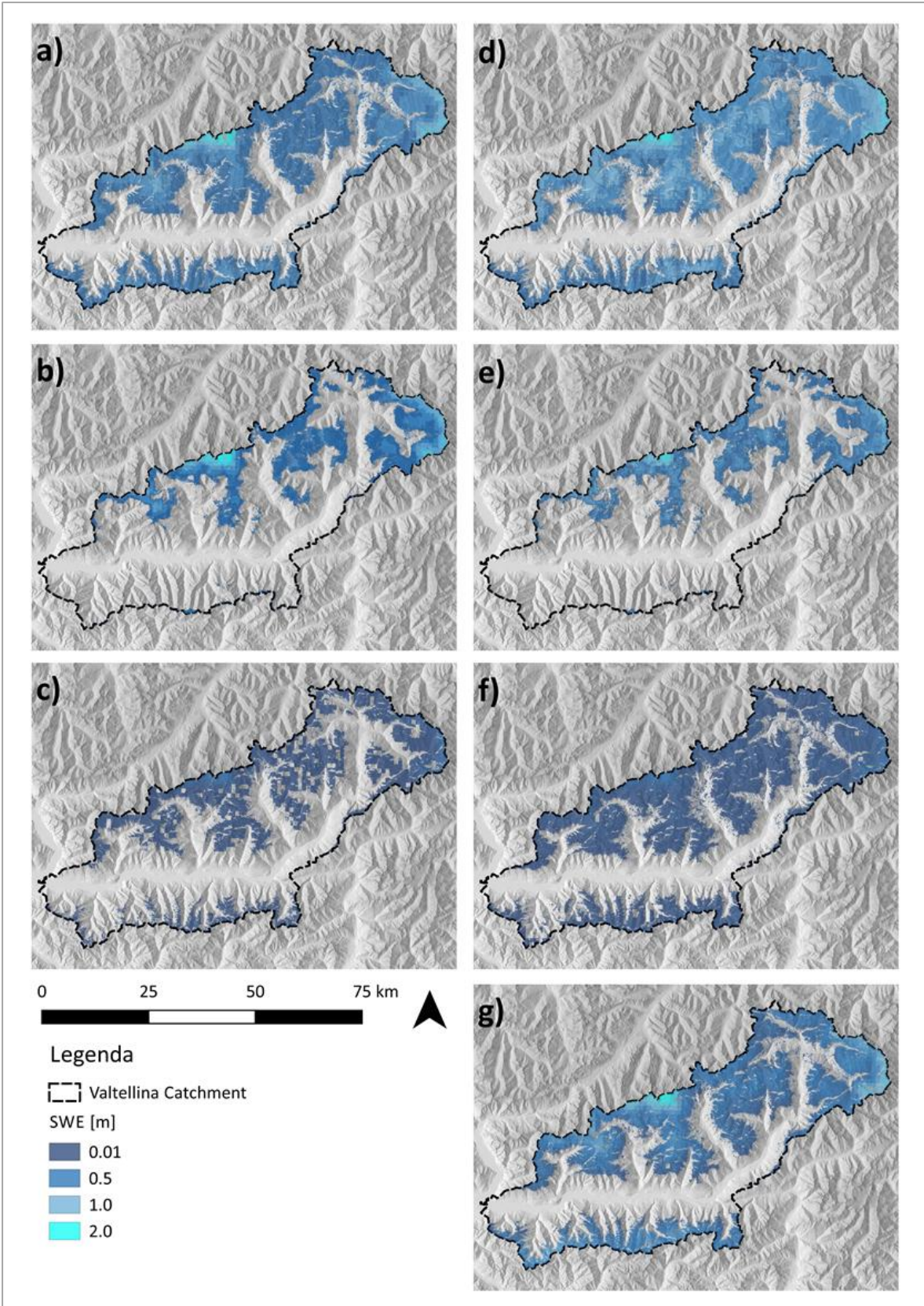


Figure 3.5: Maps of daily snow water equivalent (SWE) for three representative days in different seasons of the 2018-2019 (left) and 2019-2020 (right) hydrologic year. a-d) March; b-e) May; c-f) November; g) February.

For the validation of the SD database (from 2017 to 2020), the data from 13 snow gauge stations were available in the catchment, covering different altitude zones (**Appendix 1**). The average weekly snow depth (m) at the measurement sites and corresponding Sentinel-1 grid cells were compared. The uncertainty ( $u_{SWE}$ ), considering the total time series, amounts to 23%. The reliability is proved by a positive temporal correlation ( $r=0.54$   $p<0.01$ ) and a RMSE of 0.74 m (**Table 3.4**). Considering the three winter seasons available, the higher average RMSE was recorded for the 2018-2019's year, equal to 0.84 m (**Table 3.4**). As shown in **Figure 3.6**, the residuals for the winter 2018-2019 show high negative values, suggesting an overestimation of C-SNOW SD estimates. It is worth remarking that, in contrast to exposure and slope, altitude influences more the difference between the Sentinel and in-situ data, with an increase in RMSE of ca. 0.02 m every 100 m.

Table 3.4: Statistical relations between measured and retrieved snow depths for the total time series and for the time series of the season available.

Series	Pearson's r	RMSE [m]	NRMSE [-]
ts_2017-2018	0.51 (<0.01)	0.60	0.22
ts_2018-2019	0.48 (<0.01)	0.84	0.27
ts_2019-2020	0.62 (<0.01)	0.73	0.23
TOTAL (2017-2020)	0.54 (<0.01)	0.74	0.23

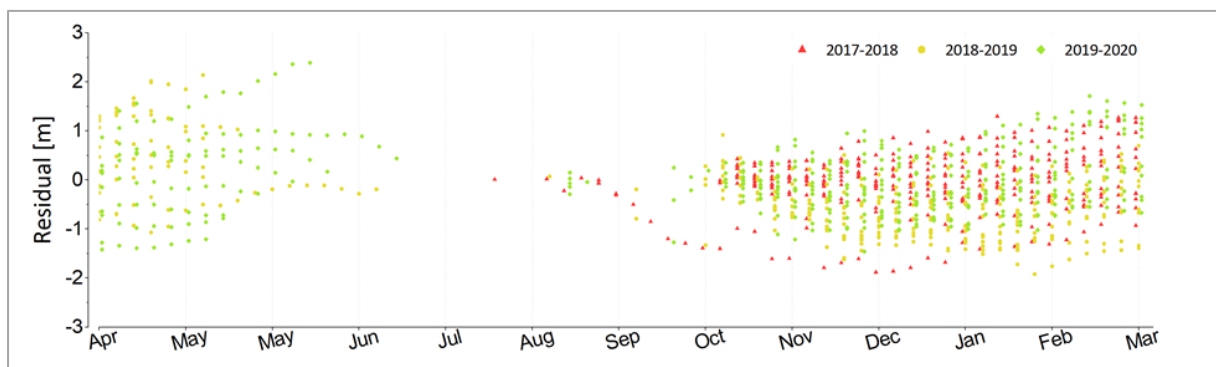


Figure 3.6: Comparison between ground-monitored weekly snow-depth values at monitoring stations (Tab 1) and C-SNOW estimates: Temporal pattern of residual during three hydrologic years.

### 3.3.3. Quantification of groundwater storage dynamics

The dynamics of storage was achieved by quantifying the volumes involved in each hydrologic process during the 3 phases of the hydrologic year in the Valtellina valley (**Figure 3.7**). The overall uncertainty ( $u$ ) of the Sentinel-based method amounts to about 38%, due to the uncertainty of ET (30%) and SWE (23%).

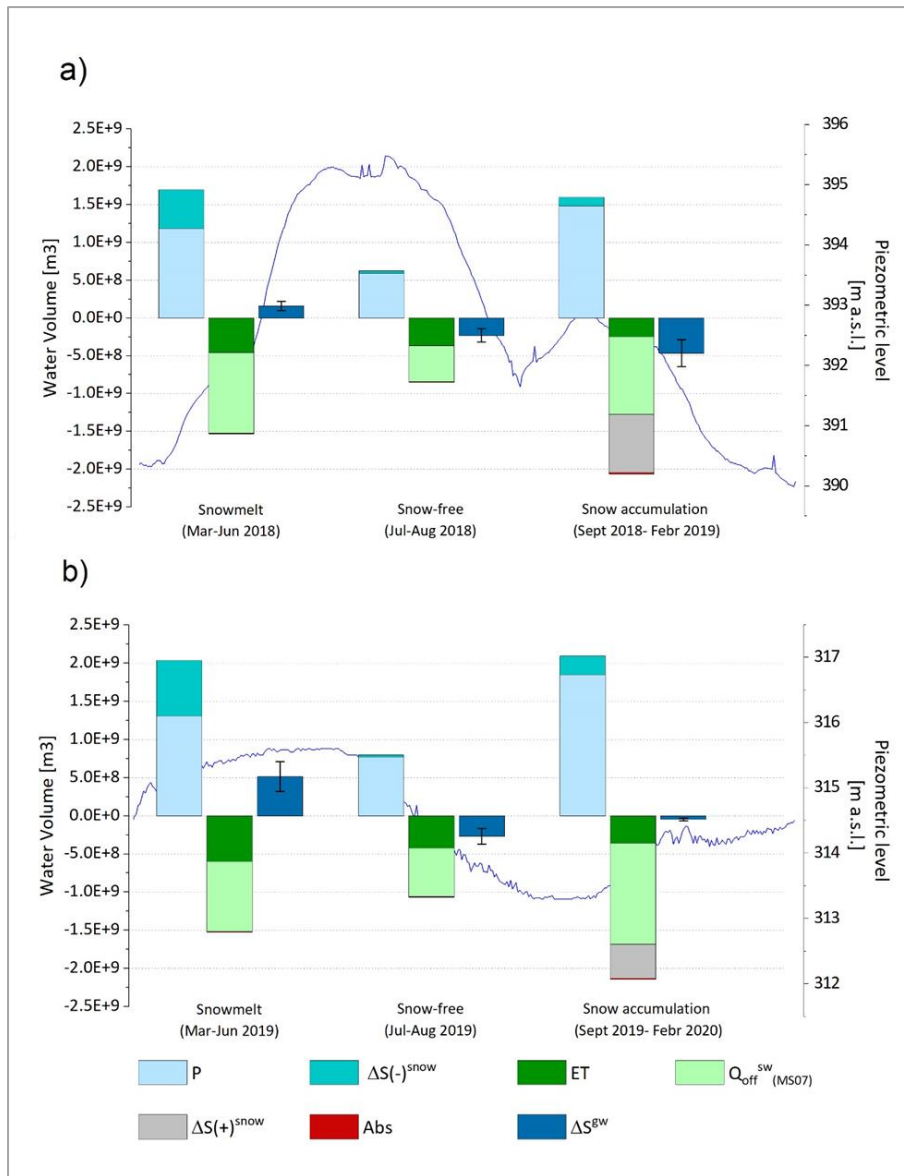


Figure 3.7: Water balance for different periods of the year (snowmelt period, snow-free period, and snow accumulation period) between the 01 March 2018 and 28 February 2019 (a) and between the 01 March 2019 and 29 February 2020 (b). Error bars represent the uncertainty associated to the use of Sentinel-based method for the estimation of the groundwater storage. In the background, the fluctuations of the groundwater level measured in the floodplain during the year.  $P$  = ERA5-based precipitation;  $\Delta S(-)^{snow}$  = Sentinel-based snowmelt;  $ET^{sw}$  = Sentinel-based Evapotranspiration;  $Q_{off}^{sw}$  = measured discharge;  $\Delta S(+)^{snow}$  = Sentinel-based stored snow;  $Abs$  = measured anthropic abstraction;  $\Delta S^{gw}$  = Sentinel-based groundwater storage.

At the catchment scale, the residual water-budget was achieved considering the Ms07 (see **Figure 2.2**, Chapter 2) as outlet point. During the first phase (March to June) of the 2018-2019 and 2019-2020 hydrological year, the groundwater storage reaches the peak value, with  $1.6\text{E}+08 \pm 0.5\text{E}+08 \text{ m}^3$  and  $5.1\text{E}+08 \pm 2.0\text{E}+08 \text{ m}^3$ , respectively (**Figure 3.7**). This corresponds to an average rate of GW storage of  $0.7 \pm 0.3 \text{ mm/day}$  and of  $2.2 \pm 0.8 \text{ mm/day}$ , respectively. The higher GW storage rate in the second year is mainly due to the amount of water made available by snowmelt, which is 40% higher than in the previous year. During the snow-free phase (July to August), we observe the first part of the recession curve in which the catchment outflow is larger than the total precipitation, leading to a depletion of the GW storage (**Figure 3.7**). In both years, the decrease is due almost equally to the evapotranspiration ( $\text{ET} \approx 40\%$  of the output) and the runoff ( $Q_{off}^{SW} \approx 60\%$  of the output) related to heavy and instantaneous rainfall events. In the snow accumulation phase (September to February), a significant additional depletion of the GW storage ( $4.6\text{E}+08 \pm 1.8\text{E}+08 \text{ m}^3$ , with an average rate of  $1.3 \pm 0.4 \text{ mm/day}$ ) is observed for the 2018-2019 hydrologic year, as a result of the surface flow ( $Q_{off}^{SW} \approx 50\%$  of the output) and the storage of water as snow ( $\Delta S(+)^{snow} \approx 38\%$  of the output), despite the instantaneous peaks of recharge due to heavy rainfall events. In contrast, during the accumulation phase of the hydrological year 2019-2020, the hydrological processes are balanced, with a small GW-storage depletion of  $4.7\text{E}+07 \pm 1.8\text{E}+08 \text{ m}^3$ , corresponding to an average rate of  $0.1 \pm 0.04 \text{ mm/day}$ . This is due to the intense autumn precipitation and the small snow storage in winter. As a consequence, the total balance leads to a negative storage of the groundwater resource only for the first hydrological year. This trend is confirmed by the groundwater levels measured along the main floodplain of the catchment, where the piezometers show an annual net lowering of about 0.10 m for the year 2018-2019 and a rise of about 0.02 m for the year 2019-2020 (**Figure 3.7**). A representative example of a piezometer is shown in **Figure 3.7**.

## 3.4. Discussion

### 3.4.1. Water dynamics

The estimate of the water balance is affected by many sources of uncertainty in the different components (Cochand et al., 2019; Sattary et al., 2002; Silva et al., 2018). For instance, river discharge and well abstraction, which are obtained from water management authorities, may be affected by instrumental measurement errors that are unknown. The snow density is calculated with an empirical relationship (Bavera and De Michele, 2009) showing a low correlation coefficient, and defined for a subcatchment of the study area. In addition, some of the minor components of the budget are neglected, such as the sublimation, the storage of the surface-water and of the unsaturated zone, and the flows into and out of the groundwater system. Note, however, that all of these components and especially groundwater outflow are of minor importance for our project area as the basin is closed. Also, storage in the unsaturated zone is of minor importance, because the vertical extent and thus the storage capacity of the unsaturated zone is small. If, however, the same approach is applied to a different basin where groundwater outflow or unsaturated storage is important, these components should be explicitly considered in the water balance.

However, the main purpose of the present work is to assess the applicability of Sentinel-based data to groundwater storage estimation. Thus, only the “additional” uncertainty derived from the use of Sentinel-based methods was explicitly quantified, resulting in a relatively small value ( $u = 38\%$ ) compared to other remote sensing methods (Dozier et al., 2016; Karimi et al., 2015). Therefore, the application of Sentinel-based methods for the analysis of the groundwater recharge and storage seems to provide consistent and physically realistic values for extensive alpine catchments. This is confirmed by the agreement between the estimated variation of the storage and the groundwater fluctuation observed in the main floodplain (see example provided in **Figure 3.7**).

Although limited to two hydrologic years, the results allow obtaining a preliminary understanding of the storage dynamics in the Alpine area. First of all, a positive groundwater storage is limited only to the snowmelt phase. In the rest of the year, the storage is negative, also during the snow accumulation phase when the precipitation input is significant but stored in the snowpack. Looking at the total GW storage for the whole hydrologic year, the

GW depletion is much higher for the year 2018-2019 with respect to the second year (**Figure 3.7**). This is confirmed by the fluctuations of the groundwater level recorded in the piezometers, located in the alluvial floodplain. However, this difference may be accentuated by the slight overestimation of SD in winter 2018-2019, leading to a higher snow storage in the first year, and a higher snowmelt in the second year.

Previous studies have shown similar dynamics in snow-dominated areas. Based on to the Special Report on Emission Scenarios (SRES), Eckhardt and Ulbrich (2003) and Neukum and Azzam (2012) found that climate change could increase groundwater recharge in spring and winter, partially associated to lower river discharge, and decrease recharge during summer and autumn, with higher river discharge. Likewise, in well-constrained water balance studies by Hood and Hayashi (2015) and Cochand et al. (2019) the groundwater storage in alpine catchments shown an excess volume of water recharge during the melting period, and an excess volume output in the late season, with an overall negative yearly storage.

#### 3.4.2. Evaluation of ET and SWE products

The Sentinel-based values of ET and SWE show a good correlation with ground-based measurements and estimates, supporting the use of these new remote-sensing-based methods to compensate for the lack of ground data. For the ET, a good correspondence with the ground-based estimations of evapotranspiration was observed (**Figure 3.2**), considering the uncertainty related to the quality of the LST maps. This agrees with the results previously reported by Guzinski et al. (2019). However, since the meteorological stations for the ET computation are available only in the floodplain, it was not possible to investigate the dependence of the elevation and the exposure in the application of SEN-ET algorithm. In comparison with ET estimates done with the other considered methods, the Sentinel-based estimates appear to be more capable to highlight anomalies and variations, which may be useful for climate change analysis. For instance, the effect of the air temperature anomaly of April 2018, associated with a recorded temperature 3-5°C higher than the seasonal average (<https://www.ncdc.noaa.gov/temp-and-precip/global-maps>) is clearly shown in the Sentinel-based estimation (**Figure 3.3**), in which the values of ET result twice those expected considering the seasonal trend. The integration of the surface temperature enables to catch the seasonal fluctuations, in contrast to other methods such as in the MOD16 algorithm. For the SWE calculation, two different approaches have been used for the snow-accumulation

and the snowmelt phases. For the first phase, the C-SNOW dataset has been used, which provides a readily usable spatially-distributed information about the SD based on Sentinel-1 satellite data. However, during the snowmelt phase, the C-SNOW dataset is affected by a higher uncertainty due to wet-snow conditions that partially reflect and absorb the radar signal (Lievens et al., 2019). For this reason, a temperature index model was preferred for the modeling the snow-melting process. Although this method involves a simplification of complex processes, it is widely adopted for large basins owing to the good model performance and computational simplicity (He et al., 2014; Hoek et al. 2003). Overall, the comparison with in-situ gauge station values is good, although an altitude-dependent discrepancy has been observed. However, it is important to remark that the meteorological monitoring sites in the mountains, especially at high altitude, lie usually on nearly flat terrain for logistical reasons. Therefore, they may not fully represent snow accumulation and melt rates on nearby slopes and in the entire pixel areas in which the stations are located (Dozier et al., 2016).

#### 3.4.3. Spatio-temporal resolution

Sentinel-based methods offer maps with the highest temporal and spatial resolution currently available to estimate ET and SWE for extensive study areas. The temporal resolution is controlled by satellite overpass and clear-sky/seasonal conditions. In large mountain catchments, the size of the area reduces the availability of useful satellite images. The full spatial coverage of the area is not guaranteed at each overpass of the satellite, offering at times incomplete information for catchment-scale studies. Moreover, at high-altitude, satellite imagery is frequently affected by cirrus clouds with an occurrence larger than 50% over the mid-latitude area (Schläpfer et al., 2020). For instance, this limitation causes information gaps during the rainy months of May and November, when only three maps per month are available for the ET estimation.

Regarding the spatial resolution, the methodology allowed us to obtain a resolution of 20 m for ET and 30 m for SWE. The 20-m resolution of Sentinel-based ET is due to the sharpening of the original Sentinel-3 imagery. Higher-resolution thermal remote sensing data that are expected to be available in the future will further improve energy flux models based on satellite data in complex terrain (Castelli et al 2018). For the SWE, the 30-m resolution is obtained by resampling the 1-km snow depth maps (C-SNOW SD), according to the density

maps, at the resolution of the SRTM DEM. The resolution along the snow line was further improved by applying the Sentinel-2 SCA. In the future, the results may be further improved by taking advantage of the Sentinel-1 full resolution (about 100 m), already planned in the next implementation for the snow depth retrieves (Lievens et al., 2019).

The high resolution achieved with the Sentinel data offers several advantages. For the ET estimates, it allows to catch the local-scale complexity of the physiographic elements and land-use in mountain areas, resulting in a wide fine-scale variability of ET values (**Figure 3.3**). This is of great importance for both water resource management and groundwater modelling. For the SD and SWE estimates, the advantage of high resolution mainly lies in the possibility to trace the snow line with more accuracy, strongly improving the volumetric budget in the transition zone between snow-covered and snow-free areas.

### 3.5. Conclusions

We propose a Sentinel-based methodology to quantify the seasonal groundwater storage in a snow-dominated catchment. It consists of the application of new promising methods for the estimation of ET (Guzinski et al., 2020) and the new database of snow depth (Lievens et al., 2019) in the residual water balance approach. The use of Sentinel data provides estimates of ET and SWE with a weekly frequency and a remarkable spatial resolution of 20 m for ET and 30 m for SWE. Applied to an extensive alpine catchment, this spatial and temporal resolution allows obtaining consistent and physically realistic values for extensive alpine catchments, as demonstrated by a relatively limited uncertainty ( $u = 38\%$ ). The high temporal and spatial resolution enables to investigate the influence of physiographic parameters (altitude, slope, and aspect) and the seasonal conditions in the ET and SWE estimates. The overall negative storage for the 2018-2019 hydrological year shows a reduced recharge potential related to low precipitation and high evapotranspiration, highlighting the possible effects of climate change on the hydrological processes and to manage the water resources in alpine snow-dominated catchments.

To the authors' best knowledge, this is the first time the groundwater storage was estimated in an extensive alpine catchment based on the synergistic use of satellite data. Moreover, the free-availability of the Sentinel data and of the algorithms for the estimation of the ET and SWE components ensure a methodology that can be applied to other catchments. The high spatial and temporal resolution of the obtained groundwater storage estimates allow to significantly contribute to the understanding of hydrogeological processes in Alpine areas, opening new frontiers to improve the elaboration and calibration of a numerical model.

### 3.6. References

- Allen, R. G., Pereira, L. S., Raes, D., & Smith, M. (1998). FAO Irrigation and drainage paper No. 56. Rome: Food and Agriculture Organization of the United Nations, 56(97), e156.
- Allen, R. G., Tasumi, M., & Trezza, R. (2007). Satellite-based energy balance for mapping evapotranspiration with internalized calibration (METRIC)—Model. *Journal of irrigation and drainage engineering*, 133(4), 380-394.
- Anderson, M. C., Kustas, W. P., & Norman, J. M. (2007). Upscaling flux observations from local to continental scales using thermal remote sensing. *Agronomy Journal*, 99(1), 240-254.
- Anderson, M. C., Norman, J. M., Diak, G. R., Kustas, W. P., & Mecikalski, J. R. (1997). A two-source time-integrated model for estimating surface fluxes using thermal infrared remote sensing. *Remote sensing of environment*, 60(2), 195-216..
- Bales, R. C., Molotch, N. P., Painter, T. H., Dettinger, M. D., Rice, R., & Dozier, J. (2006). Mountain hydrology of the western United States. *Water Resources Research*, 42(8).
- Bavera, D., & De Michele, C. (2009). Snow water equivalent estimation in the Mallero basin using snow gauge data and MODIS images and fieldwork validation. *Hydrological Processes: An International Journal*, 23(14), 1961-1972.
- Bhattarai, N., Shaw, S. B., Quackenbush, L. J., Im, J., & Niraula, R. (2016). Evaluating five remote sensing based single-source surface energy balance models for estimating daily evapotranspiration in a humid subtropical climate. *International journal of applied earth observation and geoinformation*, 49, 75-86.
- Bibi, S., Wang, L., Li, X., Zhang, X., & Chen, D. (2019). Response of groundwater storage and recharge in the Qaidam Basin (Tibetan Plateau) to climate variations from 2002 to 2016. *Journal of Geophysical Research: Atmospheres*, 124(17-18), 9918-9934.
- Braithwaite, R. J., & Olesen, O. B. (1989). Calculation of glacier ablation from air temperature, West Greenland. In *Glacier fluctuations and climatic change* (pp. 219-233). Springer, Dordrecht.
- Brodzik, M. J., Armstrong, R., & Savoie, M. (2007). Global EASE-grid 8-day blended SSM/I and MODIS snow cover. National Snow and Ice Data Center, Boulder, CO, digital media. [Available online at <http://nsidc.org/data/nsidc-0321.html>.]
- Brunner, P., Franssen, H. J. H., Kgotlhang, L., Bauer-Gottwein, P., & Kinzelbach, W. (2007). How can remote sensing contribute in groundwater modeling?. *Hydrogeology journal*, 15(1), 5-18.
- Cammalleri, C., Anderson, M. C., Gao, F., Hain, C. R., & Kustas, W. P. (2014). Mapping daily evapotranspiration at field scales over rainfed and irrigated agricultural areas using remote sensing data fusion. *Agricultural and forest meteorology*, 186, 1-11.

- Castelli, M., Anderson, M. C., Yang, Y., Wohlfahrt, G., Bertoldi, G., Niedrist, G., & Notarnicola, C. (2018). Two-source energy balance modeling of evapotranspiration in Alpine grasslands. *Remote Sensing of Environment*, 209, 327-342.
- Clow, D. W. (2010). Changes in the timing of snowmelt and streamflow in Colorado: a response to recent warming. *Journal of Climate*, 23(9), 2293-2306.
- Cochand, M., Christe, P., Ornstein, P., & Hunkeler, D. (2019). Groundwater storage in high alpine catchments and its contribution to streamflow. *Water Resources Research*, 55(4), 2613-2630.
- Colaizzi, P. D., Kustas, W. P., Anderson, M. C., Agam, N., Tolk, J. A., Evett, S. R., & O'Shaughnessy, S. A. (2012). Two-source energy balance model estimates of evapotranspiration using component and composite surface temperatures. *Advances in water resources*, 50, 134-151.
- Colombo, M., (2000). Inquadramento climatico statico e dinamico. [Online]Available at: <http://www.aineva.it/pubblica/neve43/colombo3.htm>
- D'Agata, C., Bocchiola, D., Soncini, A., Maragno, D., Smiraglia, C., & Diolaiuti, G. A. (2018). Recent area and volume loss of Alpine glaciers in the Adda River of Italy and their contribution to hydropower production. *Cold Regions Science and Technology*, 148, 172-184.
- De Franco, R., Biella, G., Caielli, G., Berra, F., Guglielmin, M., Lozej, A., & Sciunnach, D. (2009). Overview of high-resolution seismic prospecting in pre-Alpine and Alpine basins. *Quaternary International*, 204(1-2), 65-75.
- De Palézieux, L., & Loew, S. (2019). Long-term transient groundwater pressure and deep infiltration in Alpine mountain slopes (Poschiavo Valley, Switzerland). *Hydrogeology Journal*, 27(8), 2817-2834.
- DeWalle, D. R., & Rango, A. (2008). *Principles of snow hydrology*. Cambridge University Press.
- Dozier, J., Bair, E. H., & Davis, R. E. (2016). Estimating the spatial distribution of snow water equivalent in the world's mountains. *Wiley Interdisciplinary Reviews: Water*, 3(3), 461-474.
- Eckhardt, K., & Ulbrich, U. (2003). Potential impacts of climate change on groundwater recharge and streamflow in a central European low mountain range. *Journal of Hydrology*, 284(1-4), 244-252.
- Fayad, A., Gascoin, S., Faour, G., López-Moreno, J. I., Drapeau, L., Le Page, M., & Escadafal, R. (2017). Snow hydrology in Mediterranean mountain regions: A review. *Journal of Hydrology*, 551, 374-396.
- Gao, F., Kustas, W. P., & Anderson, M. C. (2012). A data mining approach for sharpening thermal satellite imagery over land. *Remote Sensing*, 4(11), 3287-3319.
- Gemitzi, A., Ajami, H., & Richnow, H. H. (2017). Developing empirical monthly groundwater recharge equations based on modeling and remote sensing data—Modeling future

groundwater recharge to predict potential climate change impacts. *Journal of hydrology*, 546, 1-13.

Guzinski, R., & Nieto, H. (2019). Evaluating the feasibility of using Sentinel-2 and Sentinel-3 satellites for high-resolution evapotranspiration estimations. *Remote Sensing of Environment*, 221, 157-172.

Guzinski, R., Nieto, H., Sandholt, I., & Karamitilios, G. (2020). Modelling High-Resolution Actual Evapotranspiration through Sentinel-2 and Sentinel-3 Data Fusion. *Remote Sensing*, 12(9), 1433.

Hayashi, M. (2020). Alpine hydrogeology: The critical role of groundwater in sourcing the headwaters of the world. *Groundwater*, 58(4), 498-510.

He, Z. H., Parajka, J., Tian, F. Q., & Blöschl, G. (2014). Estimating degree-day factors from MODIS for snowmelt runoff modeling. *Hydrology and Earth System Sciences* 18(12), 4773-4789.

Healy, R. W. (2010). *Estimating groundwater recharge*. Cambridge University Press.

Hersbach, H., Bell, B., Berrisford, P., Hirahara, S., Horányi, A., Muñoz-Sabater, J., ... & Thépaut, J. N. (2020). The ERA5 global reanalysis. *Quarterly Journal of the Royal Meteorological Society*, 146(730), 1999-2049.

Hock, R. (2003). Temperature index melt modelling in mountain areas. *Journal of hydrology*, 282(1-4), 104-115.

Hood, E., Williams, M., & Cline, D. (1999). Sublimation from a seasonal snowpack at a continental, mid-latitude alpine site. *Hydrological Processes*, 13(12-13), 1781-1797.

Hood, J. L., & Hayashi, M. (2015). Characterization of snowmelt flux and groundwater storage in an alpine headwater basin. *Journal of Hydrology*, 521, 482-497.

Jiang, Q., Li, W., Fan, Z., He, X., Sun, W., Chen, S., ... & Wang, J. (2021). Evaluation of the ERA5 reanalysis precipitation dataset over Chinese Mainland. *Journal of Hydrology*, 595, 125660.

Jonas, T., Marty, C., & Magnusson, J. (2009). Estimating the snow water equivalent from snow depth measurements in the Swiss Alps. *Journal of Hydrology*, 378(1-2), 161-167.

Karimi, P., & Bastiaanssen, W. G. (2015). Spatial evapotranspiration, rainfall and land use data in water accounting—Part 1: Review of the accuracy of the remote sensing data. *Hydrology and Earth System Sciences*, 19(1), 507-532.

Keller, J. D., & Wahl, S. (2021). Representation of Climate in Reanalyses: An Intercomparison for Europe and North America. *Journal of Climate*, 34(5), 1667-1684.

Kustas, W. P., Li, F., Jackson, T. J., Prueger, J. H., MacPherson, J. I., & Wolde, M. (2004). Effects of remote sensing pixel resolution on modeled energy flux variability of croplands in Iowa. *Remote sensing of Environment*, 92(4), 535-547.

- Lettenmaier, D. P., Alsdorf, D., Dozier, J., Huffman, G. J., Pan, M., & Wood, E. F. (2015). Inroads of remote sensing into hydrologic science during the WRR era. *Water Resources Research*, 51(9), 7309-7342.
- Lievens, H., Demuzere, M., Marshall, H. P., Reichle, R. H., Brucker, L., Brangers, I., & Jonas, T. (2019). Snow depth variability in the Northern Hemisphere mountains observed from space. *Nature communications*, 10(1), 1-12.
- Liu, M., Xiong, C., Pan, J., Wang, T., Shi, J., & Wang, N. (2020). High-Resolution Reconstruction of the Maximum Snow Water Equivalent Based on Remote Sensing Data in a Mountainous Area. *Remote Sensing*, 12(3), 460.
- Malenovský, Z., Rott, H., Cihlar, J., Schaepman, M. E., García-Santos, G., Fernandes, R., & Berger, M. (2012). Sentinels for science: Potential of Sentinel-1,-2, and-3 missions for scientific observations of ocean, cryosphere, and land. *Remote Sensing of environment*, 120, 91-101.
- McCabe, M. F., Rodell, M., Alsdorf, D. E., Miralles, D. G., Uijlenhoet, R., Wagner, W., & Shi, J. (2017). The future of Earth observation in hydrology. *Hydrology and earth system sciences*, 21(7), 3879.
- Neukum, C., & Azzam, R. (2012). Impact of climate change on groundwater recharge in a small catchment in the Black Forest, Germany. *Hydrogeology Journal*, 20(3), 547-560.
- Norman, J. M., Kustas, W. P., & Humes, K. S. (1995). Source approach for estimating soil and vegetation energy fluxes in observations of directional radiometric surface temperature. *Agricultural and Forest Meteorology*, 77(3-4), 263-293.
- Rango, A., & Martinec, J. (1979). Application of a snowmelt-runoff model using Landsat data. *Hydrology Research*, 10(4), 225-238.
- Rice, R., Bales, R. C., Painter, T. H., & Dozier, J. (2011). Snow water equivalent along elevation gradients in the Merced and Tuolumne River basins of the Sierra Nevada. *Water Resources Research*, 47(8).
- Rodell, M., Famiglietti, J. S., Wiese, D. N., Reager, J. T., Beaudoing, H. K., Landerer, F. W., & Lo, M. H. (2018). Emerging trends in global freshwater availability. *Nature*, 557(7707), 651-659.
- Sattary, J., Boam, D., Judeh, W. A., & Warren, S. (2002). The impact of measurement uncertainty on the water balance. *Water and Environment Journal*, 16(3), 218-222.
- Schläpfer, D., Richter, R., & Reinartz, P. (2020). Elevation-Dependent Removal of Cirrus Clouds in Satellite Imagery. *Remote Sensing*, 12(3), 494.
- Senay, G. B., Bohms, S., Singh, R. K., Gowda, P. H., Velpuri, N. M., Alemu, H., & Verdin, J. P. (2013). Operational evapotranspiration mapping using remote sensing and weather datasets: A new parameterization for the SSEB approach. *JAWRA Journal of the American Water Resources Association*, 49(3), 577-591.

- Silva, M. A., Amado, C., & Loureiro, D. (2018). Propagation of uncertainty in the water balance calculation in urban water supply systems—A new approach based on high-density regions. *Measurement*, 126, 356-368.
- Sheffield, J., Wood, E. F., Pan, M., Beck, H., Coccia, G., Serrat-Capdevila, A., & Verbist, K. (2018). Satellite remote sensing for water resources management: Potential for supporting sustainable development in data-poor regions. *Water Resources Research*, 54(12), 9724-9758.
- Sorg, A., Bolch, T., Stoffel, M., Solomina, O., & Beniston, M. (2012). Climate change impacts on glaciers and runoff in Tien Shan (Central Asia). *Nature Climate Change*, 2(10), 725-731.
- Strasser, U., Bernhardt, M., Weber, M., Liston, G. E., & Mauser, W. (2008). Is snow sublimation important in the alpine water balance?. *The Cryosphere*, 2(1), 53-66.
- Tang, Q., Gao, H., Lu, H., & Lettenmaier, D. P. (2009). Remote sensing: hydrology. *Progress in Physical Geography*, 33(4), 490-509.
- Taylor, R. G., Scanlon, B., Döll, P., Rodell, M., Van Beek, R., Wada, Y., & Konikow, L. (2013). Ground water and climate change. *Nature climate change*, 3(4), 322-329.
- Tarek, M., Brissette, F. P., & Arsenault, R. (2020). Evaluation of the ERA5 reanalysis as a potential reference dataset for hydrological modelling over North America. *Hydrology and Earth System Sciences*, 24(5), 2527-2544.
- Tedesco, M., Kelly, R., Foster, J. L., & Chang, A. T. C. (2004). AMSR-E/aqua daily L3 global snow water equivalent EASE-grids. Version 2. AE\_DySno. Boulder, Colorado USA. NASA National Snow and Ice Data Center Distributed Active Archive Center.
- Valt, M., Guyennon, N., Salerno, F., Petrangeli, A. B., Salvatori, R., Cianfarra, P., & Romano, E. (2018). Predicting new snow density in the Italian Alps: A variability analysis based on 10 years of measurements. *Hydrological Processes*, 32(20), 3174-3187.
- Veloso, A., Mermoz, S., Bouvet, A., Le Toan, T., Planells, M., Dejoux, J. F., & Ceschia, E. (2017). Understanding the temporal behavior of crops using Sentinel-1 and Sentinel-2-like data for agricultural applications. *Remote sensing of environment*, 199, 415-426.
- Viviroli, D., Dürr, H. H., Messerli, B., Meybeck, M., & Weingartner, R. (2007). Mountains of the world, water towers for humanity: Typology, mapping, and global significance. *Water resources research*, 43(7).
- West, H., Quinn, N., & Horswell, M. (2019). Remote sensing for drought monitoring & impact assessment: Progress, past challenges and future opportunities. *Remote Sensing of Environment*, 232, 111291.
- Wilson, J. L., & Guan, H. (2004). Mountain-block hydrology and mountain-front recharge. *Groundwater recharge in a desert environment: The Southwestern United States*, 9.
- Zhang, K., Kimball, J. S., & Running, S. W. (2016). A review of remote sensing based actual evapotranspiration estimation. *Wiley Interdisciplinary Reviews: Water*, 3(6), 834-853.

# Chapter 4: Groundwater-Surface Water modelling

## 4.1. Introduction

In snow-dominated areas, such as the European Alps, there is a widespread consensus on how climate change impacts surface inflows. Several model predictions agree with the near-term reduction in runoff and surface water resources (Patro et al., 2018; Wagner et al. 2017) during the current century. Recently, a wide range of field and modelling methods were explored to understand the impact of surface resource variability on groundwater at the catchment scale. The study of the two systems was traditionally treated separately by hydrologists and hydrogeologists, introducing strong assumptions for the boundary conditions of the model domain with respect to groundwater and surface water (Staudinger et al., 2019). Thanks to the advances in the modelling capabilities, fully integrated modelling tools have been developed for simultaneously including SW (lakes, streams and wetlands) and GW flow (unsaturated and saturated) in a single hydrological modelling scheme (Barthel et al 2016; Ala-aho et al., 2015).

Integrated models can be classified in numerous ways, considering, for example, the type of conceptual/mathematical representation of the hydrological processes, the problem setting, and the focus of interest. Based on the type of coupling scheme (Barthel et al 2016; Cochand et al.,2021), it is possible to distinguish among loosely-coupled and fully-coupled models. The loosely coupled scheme involves the use of two or more independent models that solve the flow equations consecutively or with an explicit exchange in time and space. The accuracy of this integrated model depends strongly on how the interfaces between the separate model modules are implemented, for instance the riverbed conductance for the river-aquifer interaction. Generally, the groundwater flow models are managed with software like FeFlow or MODFLOW (Harbaugh 2005; McDonald and Harbaugh 1988), while the superficial flows are solved with different types of ready-to-use models or developed for a peculiar analysis condition or for specific types of physical process. Cochand et al. (2021) offers an example of a coupling between FeFlow and a sophisticated crop modelling software to assess the impact on groundwater due to changes in irrigation patterns driven by climate change. The fully coupled scheme provides a single physically based model in which the equations governing subsurface and surface flows are solved simultaneously. Several software exist, such as CATCHY (CATCHment HYdrology, Bixio et al., 2002; Camporese et al., 2010) or HydroGeoSphere (Aquanty Inc., 2013). The first combines a 3D finite element groundwater

flow based on Richard's equation with a finite difference surface water analysis. The coupling is of the sequential iterative type, where boundary conditions are automatically switched between the two systems for each time step and for each model element (Maxwell et al., 2014). It was applied to case studies of varying size and resolution, as in Sulis et al. (2011) or Camparese et al. (2019). The HydroGeoSphere model is a three-dimensional finite element simulator designed to simulate the processes involved in the hydrological cycle, by dynamically integrating the several components. In the specific case of the interaction between rivers and groundwater, it is able to automatically generate drainage lines without having to impose river boundary and hydraulic heads in the spatial domain. This type of model was employed by De Schepper et al. (2017) to simulate seasonal variations in subsurface drainage discharge in an agricultural catchment: accurate results were obtained keeping a good spatial resolution and heterogeneity of the catchment. However, due to the massive computational load they require, these types of coupled models are generally used for small case studies or synthetic tests.

The main aim of the present work is to study the relationship between surface and groundwater flows in a valley floor in the Alpine area in order to assess the future impacts of climate change on water resources. In addition, the applicability of high spatial and temporal resolution satellite data as input for dynamic models was assessed. For this second purpose, a loosely coupled model was chosen, coupling a groundwater flow model in FeFlow with a hydrological model, able to handle spatially distributed time series for each hydrological process involved. I applied the above-mentioned model coupling for an important catchment in north of Italy, where local groundwater resources play an important role: the Valtellina valley.

## 4.2. Methods

### 4.2.1. Gw-sw modelling strategy

A spatial-distributed modelling strategy was applied for the reconstruction of surface and groundwater interactions in an extensive alpine catchment. A high spatial resolution was achieved, thanks to the detailed hydro-stratigraphical reconstruction (**Chapter 2**) and the estimation of the hydrological -balance components based on the Sentinel data (**Chapter 3**). Regarding the temporal resolution, a daily frequency was used for both hydrological processes and subsurface flows. This allows accounting for the rapid reaction time of watershed flow and groundwater movement to weather conditions in mountain areas.

To reduce the computational load required for these analyses at high spatial and temporal resolution, a loosely coupled modelling approach was selected. The approach consists in the mutual integration of two stand-alone models, where the first one allows to reconstruct surface runoff with a hydrological model of precipitation-runoff system type (**Section 4.2.2**),

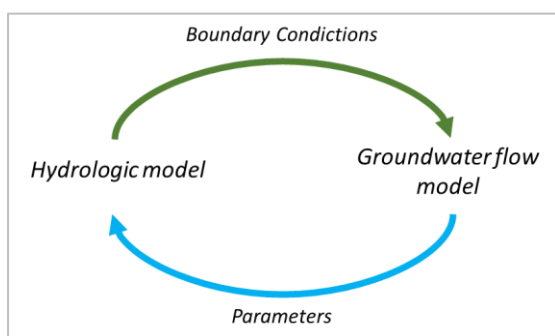


Figure 4.1: Scheme of the gw-sw modelling strategy.

while the second one reconstructs groundwater flow with finite element model (**Section 4.2.3**). As can be seen in the **Figure 4.1**, the two models interact iteratively: the results of the former play the role of boundary conditions for the latter, while the results of the latter allow the calibration of the parameters of the former.

The parameters of each model were calibrated by using time series at monitoring points. The assessment of the goodness of the fit between the observed (obs) and simulated (sim) groundwater head/stream stage was carried out using the root mean square error (RMSE, [m, log m]) and the coefficient of correlation ( $r$ , [-]). Moreover, for the hydrologic model, the Nash-Sutcliffe Efficiency (NSE, [-]) (Nash and Sutcliffe 1970, **Eq. 4.01**) and the percentage bias (PBIAS, [%]) (**Eq. 4.02**) were calculated on the volume of the discharge ( $Q$  [m<sup>3</sup>/d]) to assess the performance:

$$NSE = 1 - \frac{\sum_{t=1}^T (Q_{Obs(t)} - Q_{Sim(t)})^2}{\sum_{t=1}^T (Q_{Obs(t)} - \bar{Q}_{Obs})^2} \quad \text{where } t \text{ is the daily time step} \quad (4.01)$$

$$PBIAS = \frac{\sum_{t=1}^T (Q_{Obs(t)} - Q_{Sim(t)}) \times 100}{\sum_{t=1}^T Q_{Obs(t)}} \quad \text{where } t \text{ is the daily time step} \quad (4.02)$$

The objective of the calibration was to achieve a NSE value above zero, and to minimize the accumulated discharge error to approximately  $\pm 38\%$ , which we defined as satisfactory in relation to the uncertainties of the input hydrologic processes (see **Chapter 3**). For the hydrogeological modelling,

#### 4.2.1.1. Climate change scenarios

The flow model was used to evaluate the impact on groundwater of possible climate change scenarios. Specifically, a reduction in runoff was applied over the boundary conditions of a steady-state model. The percentage of reduction was selected in accordance with Wagner et al. (2017), where the change in river discharge characteristics for the Alpine region was estimated based on the ENSEMBLES project data (van der Linden and Mitchell, 2009). In particular, for the present work, scenarios from four regional climate model (RCM) simulations available for the Alpine region (Wegner et al. 2017) were calculated on the surface resources based on the annual averages and applied to the flow model to compare the variation of the groundwater resource.

#### 4.2.2. Hydrologic Modelling

The method adopted for the simulation of the river discharge is based on the Runoff modelling tank system (Leavesley et al., 1983) (**Figure 4.2**).

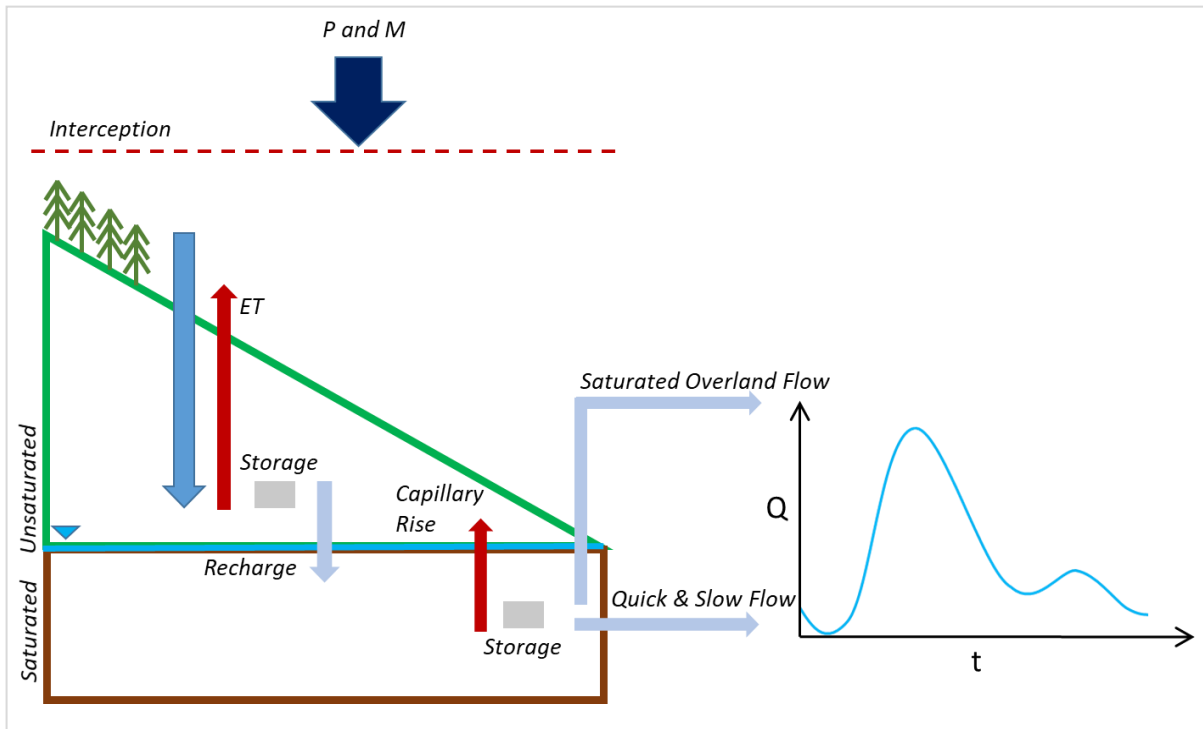


Figure 4.2: Schematic presentation of the tank system considered for the hydrologic modelling.

The input of the system is provided by the melted snow and the excess precipitation from the interception by vegetation. This quantity of water feeds the first reservoir, the unsaturated zone, and then the second reservoir, the saturated zone. Within the first reservoir, the input is added to a previously stored volume of water. When a maximum storage level is reached, the second reservoir is recharged, regulated by a recession constant between the two tanks. The amount of daily evapotranspiration is then subtracted from the volumes remaining in the unsaturated zone. As a result, the second tank includes the previously stored volumes and the recharge from the unsaturated zone. Then, the runoff is estimated in the quick and slow (the base flow) flow contribution as a function of the recession coefficients. Finally, net infiltration is obtained from the difference between day  $t$  and day  $t-1$  of the water stored in the saturated zone. In addition, during exceptional precipitation events, saturated overland flow occurs and contributes to the daily runoff. In fact, under these circumstances, net precipitation causes the unsaturated zone to become completely saturated, leading to upwelling of the water table to the surface and runoff. The partitioning of inputs to the tanks occurs differentially throughout the basin as a function of soil and land cover. For this purpose, the ESA-CCI-LC 2015 land cover map (<http://maps.elie.ucl.ac.be/CCI/viewer>) was adopted. This map allows to define the hydrologic response units (HRUs) to which hydrologic

parameters can be assigned from literature values or from the hydro-stratigraphic analysis. Specifically, the parameters involved and calibrated in the model are: I) the interception threshold and II) the maximum storage of the unsaturated zone.

An added value in the application of the model is given by the high temporal and spatial resolution maps of precipitation, snowmelt and evapotranspiration obtained by satellite data. In particular, the daily rainfall data come from the ERA5 reanalysis database (produced by ECMWF, Hersbach et al., 2020) and resampled on the SRTM DTM (provided by NASA JPL) raster grid at 30m of resolution. Snowmelt and evapotranspiration data previously obtained by physically based methods using Sentinel data at 30m resolution (**Chapter 3**) were linearly resampled at daily frequency.

The model has been implemented in the PCRaster Python language and is provided in **Appendix 02**. PCRaster (2008) is a framework for the development of dynamic models, in which raster-based two-dimensional maps and three-dimensional block structures are organized and managed on spatial entities (pixel) and the temporal domain (Schmitz et al., 2009). The model, executable for  $n$  time steps, is implemented in a python class subdivided into an initial and a dynamic model section. In the initial section, the constant-over-time specifications or values are set, such as the calibration parameters and the values linked to the HRUs. In the dynamic section, the daily input (precipitation (P), snow melt (M), and evapotranspiration (ET)) are imported and the net infiltration and runoff are calculated for each pixel at the  $n$ -time step. Moreover, for the estimation of the discharge at location of the closing points, the sum of the total saturated overland flow, quick flow and slow flow is calculated PCRaster native operation. The accuflux operation calculates the total discharge (lateral flow) for each cell as the amount of water that is transported out of the cell and composes of the water in the cell itself and the water from the upstream cells. Upstream cells are derived from the local drain direction map.

#### 4.2.3. Groundwater flow Modelling

Groundwater flow was numerically modelled with the finite elements Feflow 7.2 software (Diersch, 2013) already use for the steady-state calibration of the hydrological parameters. The model allows solving 3D flow in a saturated aquifer with discretization of the Darcy equation, for each element, considering surface water inputs. The surface water inputs were included in the model as time-varying boundary conditions at a daily frequency, as shown in the **Figure 4.3**. Regarding the interaction with rivers, to simulate the natural runoff conditions, a Cauchy boundary condition was imposed on the riverbed using time series for each node. The time series was generated in a loop process: discharge dynamics obtained from the hydrologic model at tributary valley closure points and along the main river were converted to river water heights and added to the node elevation. To do this, available relationships between discharge and river water level were used. Lateral fluxes from consolidated rock between two different sub-catchments were assumed negligible with respect to the other volumes involved. The recharge rate of the saturated zone was assigned through the material property in/outflow on the top, where the value is positive if the groundwater is recharging, negative if there is a withdrawal. The time series for each element on the top of the model was generated by the infiltration maps of the hydrologic model and applied using “assign material data to time stages” option.

The transient model was implemented starting from the calibrated steady-state model, where the hydraulic conductivity of the aquifer and the conductance of the riverbed were automatically calibrated with PEST (J.E Doerthy & R.J. Hunt, 2010) (**Chapter 2**). In transient state simulation, the calibration of Drain-/Fillable Porosity is required to reproduce the correct magnitude of fluctuations due to surface inputs. This parameter corresponds to the specific yield, which describes the fraction of the bulk volume that can be drained under the forces of gravity. On the zones detected by the hydro stratigraphic characterization, calibration was carried out for a time frame of 30 days, corresponding to the initial phase of aquifer recharge during the snowmelt. In particular, a constant porosity was estimated. After

the calibration, the model was used to simulate the daily mean groundwater dynamics and also the seasonal dynamics for two hydrologic years.

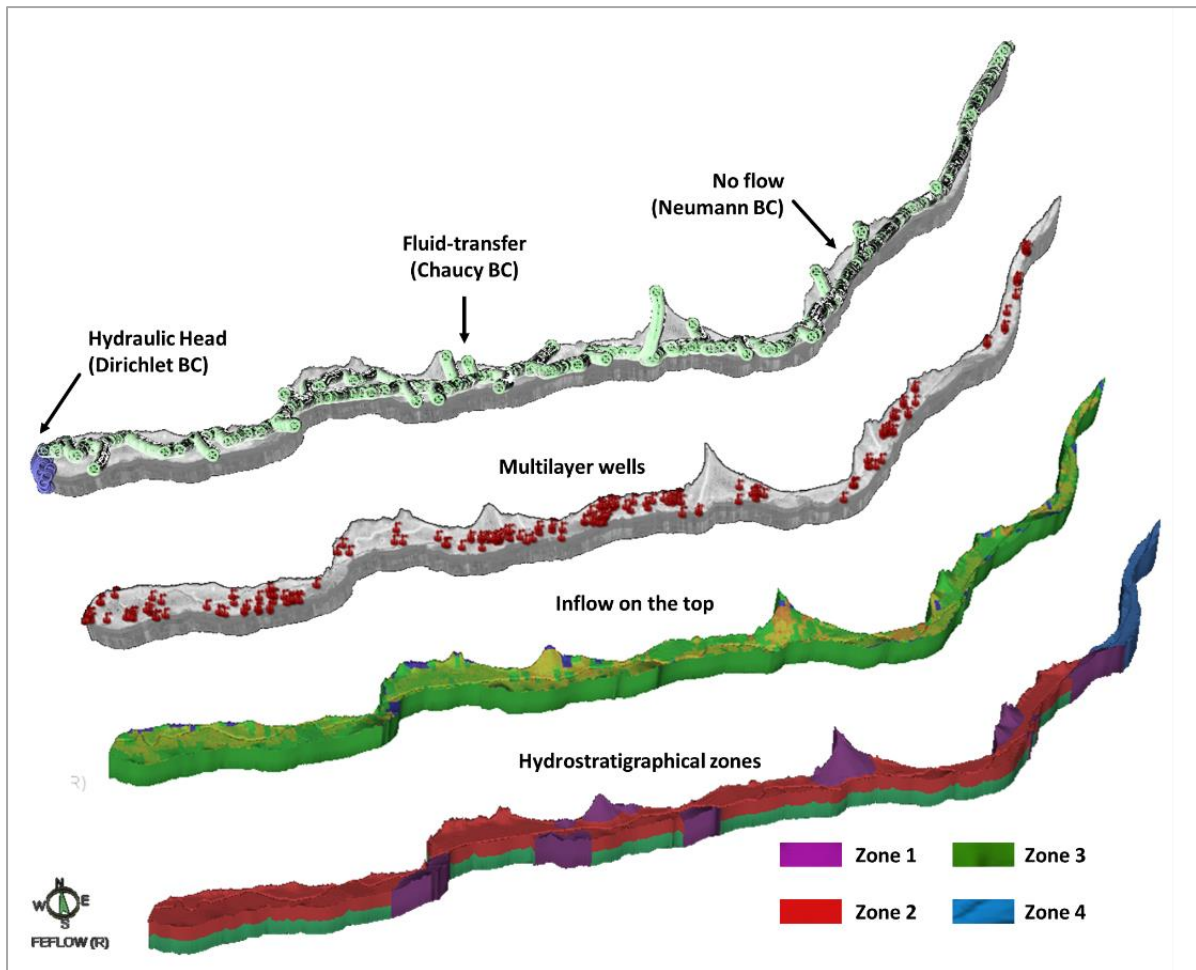


Figure 4.3: Boundary conditions and hydrostratigraphical zonation considered in the 3D model.

## 4.3. Results and discussion

### 4.3.1. Surface water

Surface flow modelling was carried out for the whole area of the Valtellina basin (26,000 km<sup>2</sup>). The area has been discretized with a 30x30 m grid, constructed from the SRTM DEM. The period selected for the simulations includes two hydrological years between 15 March 2018 and 15 March 2020. The total time steps simulated are 732 days. For each time step, the three maps related to the hydrological input given by the total precipitation (ERA5), snow melt and evapotranspiration (Sentinel-based method, **Chapter 3**) were assigned.

The elevation in the study area ranges from 200 m a.s.l., at the closing point, to a maximum of 4,000 m a.s.l., at the northern ridge of the valley. Furthermore, the catchment has been divided into 5 HRU (**Figure 4.4**) according to the land cover and the hydrogeological characterisation of the valley floor:

- HRU1: Area corresponding to alluvial deposits and permeable alluvial fans on the valley floor. In this area the unsaturated area can be characterised by variable thicknesses, with a water table depth of 5 m, while the main river is in close connection with the saturated area (**Chapter 2**). The maximum storage in the unsaturated zone was calibrated to be half this thickness (2.5 m). The calibrated interception limit is equal to the minimum value of 0.01 m.
- HRU2: area corresponding to the anomalous alluvial fans of the valley floor. These areas are characterised by low permeability and are not in direct contact with the tributary rivers that flow through them (**Chapter 2**). Here, a high value (5.0 m) of storage in the unsaturated was obtained, due to the higher thicknesses. The calibrated interception limit is the minimum value (0.01 m).
- HRU3: Urban area as defined by the Land Cover map (ESA-CCI-LC 2015). In correspondence with urban areas, soil sealing prevents infiltration into the unsaturated and saturated zones. Here only surface runoff is expected.
- HRU4: the sloping area covered by forest and grassland type vegetation (Land cover map). The thickness of non-saturated soil above the rock aquifers is generally limited and the maximum storage in the non-saturated was calibrated to be 0.5 m, with quick flow in the direction of higher order streams prevalent. here, where interception by vegetation is important, the limit was set at 0.05 m.

- HRU5: this area includes bare rock areas, with less than 4% vegetation cover (Land Cover map). In this area, storage in the non-saturated is very limited (0.1 m). The flow is directly channelled into the saturated through rock fractures or to higher order rivers by surface runoff. The calibrated interception limit is the minimum value (0.01 m).

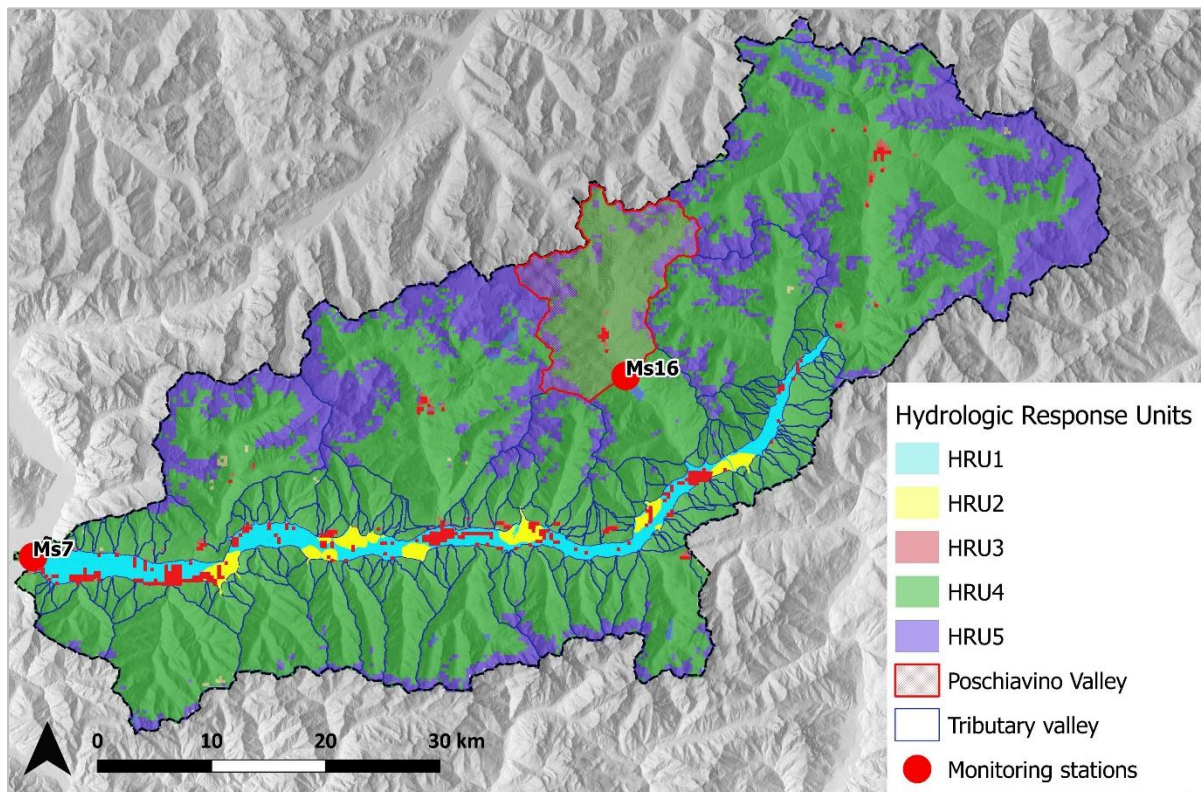


Figure 4.4: Division of the Valtellina catchment into hydrologic response units. The map shows the subdivision of the tributary valleys and the observation points used for the calibration of the hydrological model.

The implemented hydrological model, based on meteorological input from satellite data, enables the modelling of surface flows over large Alpine areas. The PCRaster Python environmental allows to manage and optimise the high computational load, maintaining the high spatial and temporal definition of the input data. The discharge was calculated at the tributaries and at the main river. The distribution of the tributary valley is shown in the **Figure 4.4**. The closing points were defined through the flow direction map and the resulting channel map. The calibration of the hydrographs was validated by considering the 2 available time series. The first one is located at station MS7, at closing point of the whole catchment, and second one at station MS16, at the monitoring station located inside the Poschiavino Valley (**Figure 4.4**). As shown in **Table 4.5**, the statistical comparison between the observed and the simulated time series indicate that the model can reproduce fluctuations in flow rates with

good efficiency and high correlation. Furthermore, considering the volumes involved in the two hydrological years, the PBIAS indicates an underestimation of volumes of less than 15%. This value is acceptable considering the uncertainty attributed to the inputs based on satellite data (Chapter 3). However, for the hydrological year 2018-2019, an underestimation of volumes can be observed (Figure 4.5). A visual qualitative comparison of the hydrographs (Figure 4.5) shows that the model is able to reproduce the seasonal recharge phases given by snowmelt, starting in March, and rainfall, between October and November. In addition, the hydrographs correctly simulate the extreme weather event of October 2018, with a rapid depletion peak related to saturated overland flow. For the comparison of the MS16 hydrographs, it is important to consider that the discrepancy between the observed and simulated data is also influenced by the monitoring data. In fact, the MS16 hydrograph shows truncations of peak recharge (e.g., January-February 2019) that may be due to water management in hydroelectric plants located in the tributary valleys (D'Agata et al., 2018). However, at the watershed scale, the total volumes should not be affected by anthropic discharge management.

Table 4.5: Statistical data related to the comparison between observed and simulated time series at the two monitoring stations Ms7 and Ms16).

	Ms7	Ms16
NSE	0.72	0.62
%VOL	27%	11%
R, p-value	0.73 (P-VALUE<0.01)	0.74 (P-VALUE<0.01)
nRMSE)	0.13	0.14
R <sup>2</sup>	0.53	0.55
pBias	13.59	11.40

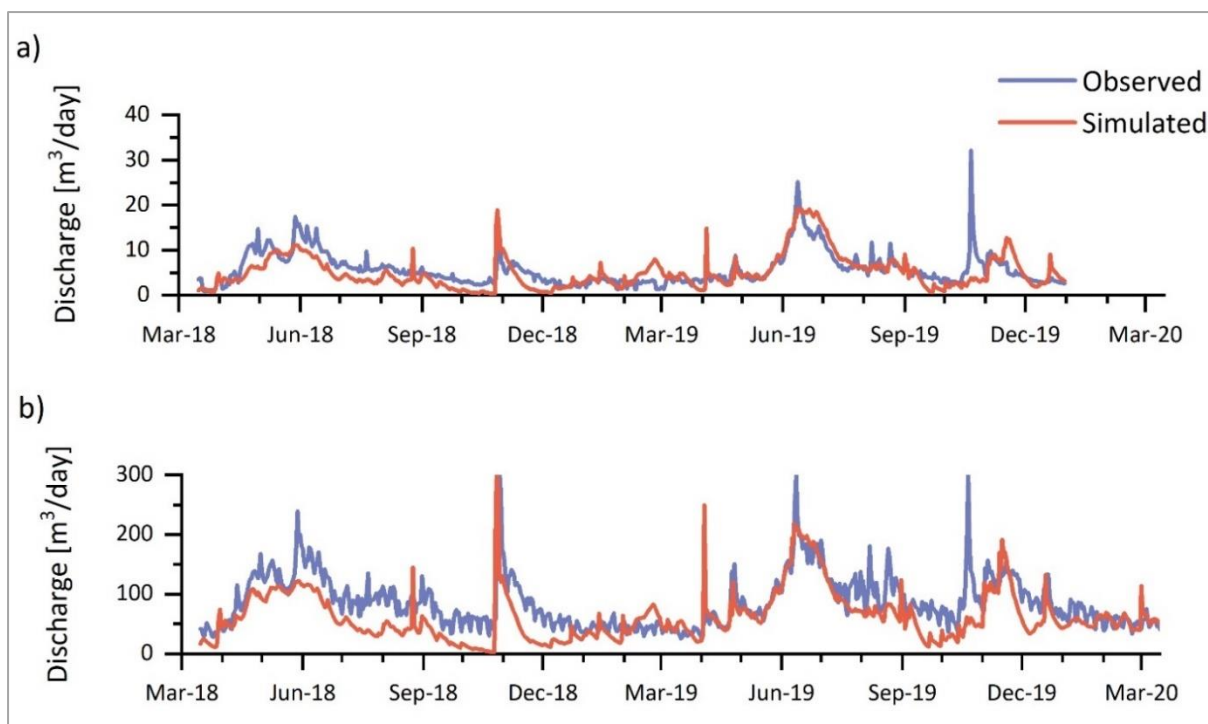


Figure 4.5: Comparison between discharges simulated versus observations at two gauging stations in terms of time series. a) MS16; b) MS7.

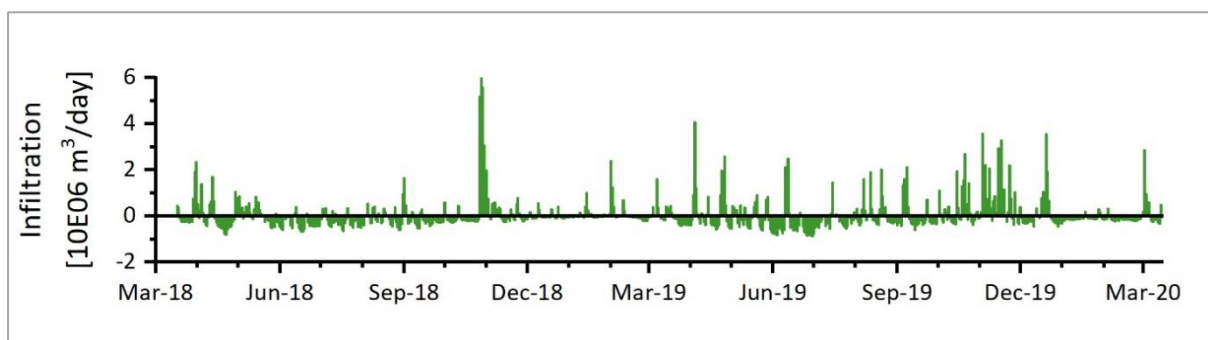


Figure 4.6: Time series of the infiltration volume in the Valtellina valley floor for the period 2018-2020.

After calibration, 732 daily saturated infiltration maps were extracted from the hydrological model. No field data were available for validation. However, the maps show infiltration values consistent with the annual trends in the area. In particular, along the flood plain, the infiltration volumes show an input into the saturated system of 1.24E06 in the 2018-2019 hydrologic year and 2.62E06 in the 2019-2020 hydrologic year. These values confirm that hydrological year 2018-2019 receives a lower volume of surface water. Moreover, seasonal fluctuations and fluctuations related to exceptional events are clearly represented (**Figure 4.6**). Furthermore, the infiltration data confirm the decision not to consider lateral flows in the consolidated-rock area between two different sub-catchments. In fact, the results show influxes of small volumes occurring only on a few days over the entire period.

### 4.3.2. Groundwater

The groundwater flow modelling was carried out on the floodplain of the Valtellina valley. The calibration of porosity was done by using PEST for the 4 hydrostratigraphic zones (**Chapter 2**) and for the period between May and June when the main recharge phase takes place. In addition, the second hydrological year was selected in order to have a larger number of time series to be used in the calculation of the objective function (**Table 4.6**).

Table 4.6: Calibrated specific yield for each hydro stratigraphical zone (see Figure 4. ).

	<i>Specific yield []</i>
Zone 1	0.17
Zone 2	0.1
Zone 3	0.1
Zone 4	0.2

Subsequently, the simulation of the two whole hydrological years was carried out. The time series obtained at the observation points returned results of different quality. For 3 of the 13 wells, no acceptable correlation was obtained between the observed and measured series, with non-comparable ranges of fluctuations (**Table 4.7**). These points are located in different hydrostratigraphic zones and are not subject to similar forcing. Instead, as can be seen in **Table 4.7**, for the other points there was an average correlation of 0.44 (p-value < 0.01). The simulation results generally reproduce seasonal trends and exceptional meteorological events, but do not perfectly match the depletion curves. In fact, a comparable range of fluctuations was detected, with an average annual fluctuation of 1.65 m compared to the 2.25 m observed in the measured time series. In the upstream area, defined as hydrostratigraphic zone 4, the correlation is lower. The reason may be related to the disregard of the lateral flux that in this area might have more influence due to the reduced width of the valley floor.

Table 4.7: Comparison between the observation time series and the simulated time series. For each observation point is shown the coefficient of correlation, the p-value, the range of the fluctuation ( $\Delta$ ) observed and simulated.

	<i>r</i>	<i>p-value</i>	$\Delta_{obs}$	$\Delta_{sim}$
GW01	0.44	<0.01	2.40	2.80
GW04	0.1	<0.01	5.90	1.89
GW08	0.36	<0.01	2.93	1.39
GW10	0.2	<0.01	1.59	0.80
GW27	0.81	<0.01	0.95	0.86
GW28	0.51	<0.01	2.62	2.18
GW30	0.67	<0.01	1.83	2.03
GW43	0.41	<0.01	1.16	1.19
GW45	0.58	<0.01	1.42	1.81
GW46	0.2	<0.01	1.60	1.96
GW57	0.57	<0.01	2.33	1.19

However, from a quantitative point of view, the volumes involved in the water balance (**Table 4.8**) reproduce the negative groundwater storage values for both hydrologic years. In addition, the relationships identified between surface water and groundwater are confirmed, with a positive contribution from rivers for both the year 2018-2019 and the year 2019-2020. This confirms the important role of tributaries (disconnected) and the main river for the aquifer recharge. Infiltration, on the other hand, is confirmed as playing a minor role in aquifer recharge, although the volumes are of the same orders of magnitude as river water volumes. In particular, a negative infiltration value was obtained in the first hydrological year. This is consistent with evapotranspiration data obtained with satellite methods (**Chapter 3**), through which the thermal anomaly of April 2018 (<https://www.ncdc.noaa.gov/temp-and-precip/global-maps>) can be captured. Finally, in both years there is a negative imbalance of the volumes involved in the model of about  $6,0E05 \text{ m}^3$ . This may be due to two factors. The first one concerns the uncertainty ( $\pm 38\%$ ) obtained from the use of satellite data for the reconstruction of the meteorological input data. The second may be due to the neglect of lateral fluxes. However, it is important to note that the imbalance is two orders of magnitude smaller than the volumes involved by rivers, infiltration and the resulting groundwater storage. Therefore, it does not affect the water balance significantly.

Table 4.8: Volumes involved in the water balance for the 2018-2019 and 2019-2020 hydrologic year.

	2018-2019	2019-2020
RIVER [M3]	2.43E+07	2.79E+07
INFLOW [M3]	-4.05E+06	1.54E+07
STORAGE [M3]	-2.36E+07	-4.12E+07
IMBALANCE [M3]	-6.23E+05	-6.24E+05

#### 4.3.3. Climate Change scenarios results

For the simulation of predictive climate scenarios, four steady-state models were developed. In accordance with Wegner et al. 2017, the scenarios chosen for simulation are as follows:

- SC01: Consider the climate prediction model CNRM-RM4.5, it presents the special case of stronger summer heating than winter heating. For this scenario, a null runoff change is predicted for the study area within 2050. Therefore, the simulation is represented by surface water values equal to the average of the two hydrological years considered.
- SC02: This scenario (C4IRCA3) is defined as "humid warm" as it presents a very humid and warm climate change signal (CCS) in both summer and winter. According to these forecasts, the Valtellina basin would present a 4% increase in surface resources in the next 30 years. Therefore, the surface inputs of the groundwater flow model were increased by 4% compared to the average of the two hydrological years considered.
- SC03: The KNMI-RACMO2 climate model represents the moderate scenario, for which there is a reduced reduction in surface resources of 8% in the Valtellina catchment area. For this simulation, hydrological inputs were reduced by 8% compared to the average volumes estimated for the hydrological years 2018-2019 and 2019-2020.
- SC04: It consists of very warm and dry climate change signal in summer, and mild conditions in winter (Meteo-HCHadRM3Q0). This scenario is the most extreme, predicting a 24 % reduction in runoff for the study area within 2050. The boundary conditions of the hydrological model were reduced by 24% compared to the average of the hydrological years analysed.

To assess the effect of the scenarios on the groundwater resource, a comparison was made between the SC01 scenario, equivalent to the current state, and the other three scenarios. The groundwater levels obtained at 48 observation points were considered for the quantitative assessment (**Figure 4.7**). From the SC02 simulation, it is observed that the increase in surface input generates an average groundwater increase of 0.10 m, with values ranging from 0.50 m to 0.001 m. The simulation of the SC03 scenario shows that the moderate prediction of the 8% reduction in surface resources would lead to an average decrease in the water table of 0.20 m, in a range between 1.00 m and 0.01 m. Finally, the extreme scenario SC04, simulates a 0.60 m lowering of the water table, with values ranging between 3.00 m and 0.03 m.

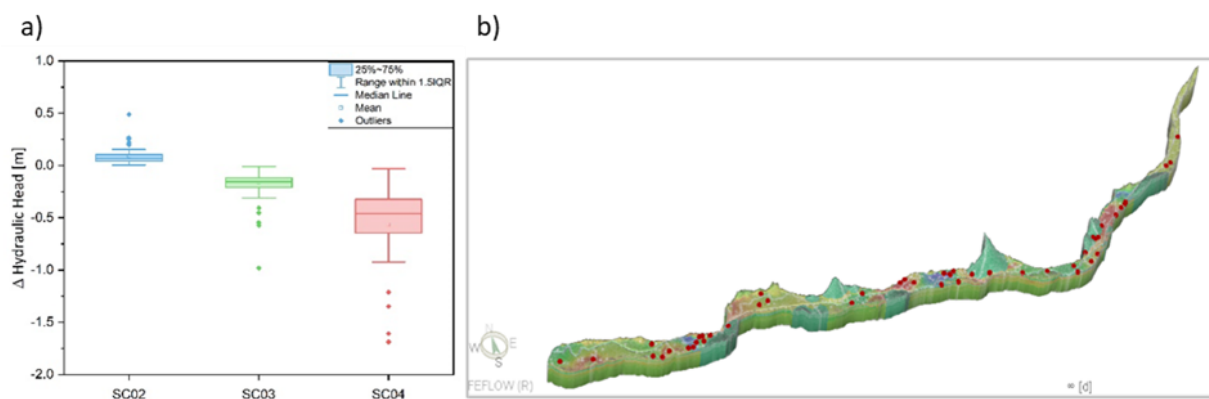


Figure 4.7: Groundwater level differences (a) obtained by comparing the SC01 (current state) scenario with three climate change scenarios at the observation points (red dots in the figure b).

From the point of view of water resource management, the reductions observed in simulations SC03 and SC04 could cause problems for water managers. Indeed, the lowering of the water table may require modifications of the shallowest extraction wells or the relocation of the abstraction pumping system.

## 4.4. Conclusion

In the last decades, numerous methods have been developed to understand the impact of surface resource variability on groundwater at the catchment scale. Due to advances in modelling capabilities, integrated modelling tools have been developed to simultaneously include SW (lakes, streams and wetlands) and GW (unsaturated and saturated) flow in a single hydrological modelling scheme. The problem associated with modelling the two different water systems is mainly given by the temporal and spatial resolution that is generally used. In this context, the present work provides a new modelling framework that can be used to integrate satellite data into the study of groundwater resources. A loose coupling of a simplified hydrological and hydrogeological model is proposed to analyse groundwater interactions and dynamics. The loose coupling has been selected to ensure a high spatial and temporal resolution while keeping the computational load low and, therefore, making it easier to manage data and results. In this type of coupled modelling system, the two models are applied iteratively so that the results of the former play the role of boundary conditions for the latter, while the results of the latter allow the calibration of the parameters of the former. The approach was applied to a large alpine mountain basin, the Valtellina valley. The hydrological model allowed flow fluctuations to be re-predicted with good efficiency and high correlation. For the groundwater flow model, the results showed a moderate correlation with the time series available. Furthermore, the simulations showed a negative groundwater storage for the two hydrological years considered. The applicability of this method made it possible to carry out an analysis of the effects of climate change. Considering existing predictive scenarios for surface resources, four scenarios were modelled that showed average changes in water table levels of less than one metre. The observed magnitude of changes may be problematic for water resource management by water utilities for at least two of the simulated climate change scenarios (SC03 and SC04).

## 4.5. Appendix 2

### Codex of the hydrological model implemented in the PCRaster Python language

---

```
from pcraster import *
from pcraster.framework import *

class RunoffModel(DynamicModel):
    def __init__(self, cloneMap):
        DynamicModel.__init__(self)

        setclone(cloneMap)

    def initial(self):
        # Add here the static maps that we need to read from disk
        landuse = self.readmap("landuse_cl")
        DEM = self.readmap("dem_cl")
        self.mask = self.readmap("mask_cl")
        self.flowdirection = self.readmap("ldd3")

        self.Ku = scalar(1.5)          # Recession constant of flow from unsaturated to saturated zone
        self.surface = scalar(0.0009) # surface of a gridcell (km2)
        self.ConvConst = scalar(0.000010416)
        self.rtg = scalar(5)          # Recession constant quick flow
        self.rts = scalar(10.0)       # Recession constant slow flow
        self.Su = scalar(50.0)        # storage unsaturated zone
        self.Ssmax = scalar(0.0)      # parameter controlling the groundwater flow to the river
        self.Ss = scalar(50.0)        # storage saturated zone

        # Add here the lookup tables
        self.InterceptionThreshold = lookupscalar("d.tbl",landuse) # interception threshold (mm)
        self.InterceptionThreshold = self.InterceptionThreshold
        self.report(self.InterceptionThreshold,"d")
```

```

self.SuMax = lookupscalar("smaxcomp.tbl",soil)      # maximum storage unsaturated zone (mm)
self.SuMax = self.SuMax
self.report(self.SuMax,"SuMax")

self.SeparationCoefficient = lookupscalar("cr.tbl",landuse) # separation coefficient (-)
self.report(self.SeparationCoefficient,"cr")

self.QuickFlowCoefficient = lookupscalar("qccomp.tbl",soil) # Quick flow coefficient (-)
self.QuickFlowCoefficient = self.QuickFlowCoefficient
self.report(self.QuickFlowCoefficient,"Qc")

self.MaxCapRise = lookupscalar("cp.tbl",landuse)    # potential capillary rise (mm)
self.report(self.MaxCapRise,"cmax")

# Minimum Capillary rise
self.MinCapRise = self.SuMax / 4.0

# initialise time series output
self.Measurements = self.readmap("outlet") # read map with measurement locations
DischargeAtMeasurementLocations = "Discharge.tss" # define the output timeseries file name
self.DischargeTSS = TimeoutputTimeseries(DischargeAtMeasurementLocations,
                                         self,
                                         self.Measurements,
                                         noHeader=False)

def dynamic(self):

#import maps from satellite data
Precipitation = self.readmap("pr")
Precipitation=ifthenelse(Precipitation<0, 0, Precipitation)
SWE = self.readmap("swe")
ET = self.readmap("etN")

#create map interception from landuse
Interception = min(Precipitation, self.InterceptionThreshold)
self.report(Interception,"int")

```

```

#Calculate Net Precipitation
NetPrecipitation = max(0,(Precipitation-Interception))
NetPrecipitation = NetPrecipitation-SWE
NetPrecipitation=ifthenelse(NetPrecipitation>0, NetPrecipitation, 0)
self.report(NetPrecipitation,"pn")

# Modelling of the unsaturated zone
self.Su = self.Su + NetPrecipitation

    ### Calculate the Saturated Overland Flow
SaturatedOverlandFlow = ifthenelse(self.Su > (self.SuMax*1.5), self.Su - (self.SuMax*1.5), 0)
self.Su = ifthenelse(SaturatedOverlandFlow >0,(self.SuMax*1.5),self.Su)
self.report(SaturatedOverlandFlow,"saof")

    ### Calculate the Infiltration

self.SuExcess = max(0, ((self.Su - self.SuMax) / self.Ku))
self.report(self.SuExcess,"Inflow")

    ### Calculate Su for day after (et act on the infiltration of the day after)
self.Su = self.Su - self.SuExcess
self.Su = self.Su - ET
self.report(self.Su,"su")

# Modelling of the saturated zone
self.Ss = self.Ss + self.SuExcess
self.report(self.Ss,"ss")

# Calculate quick flow
SsQuick = self.SsMax * self.QuickFlowCoefficient
QuickFlow = max((self.Ss - SsQuick), 0) / self.rtg
self.Ss = self.Ss - QuickFlow
self.report(QuickFlow, "qflo")

# Calculate slow flow
SlowFlow = max(self.Ss, 0) / self.rts
self.Ss = self.Ss - SlowFlow

```

```
self.report(SlowFlow,"sflo")

# Capillary rise
CapRise = ifthenelse(self.Ss > self.MinCapRise, min(self.MaxCapRise,ET,self.Ss), self.MinCapRise)
self.Ss = self.Ss - CapRise
self.Su = self.Su + CapRise
self.report(self.Su,"su")
self.report(self.Ss,"ss")

#Calculate total runoff and discharge
Runoff = SaturatedOverlandFlow + SlowFlow+ QuickFlow
Discharge = accuflux(self.flowdirection, Runoff) * self.ConvConst
self.report(Discharge,"q")

# Report discharge time series at measurement locations
self.DischargeTSS.sample(Discharge)

myModel = RunoffModel("mask_cl.map")
dynModelFw = DynamicFramework(myModel, lastTimeStep=732,firstTimestep=1)
dynModelFw.run()
```

---

## 4.6. References

- Aquanty Inc. (2013).: Hydrogeosphere Analytics. Retrieved from <http://www.aquanty.com/>.
- Ala-Aho, P., Rossi, P. M., Isokangas, E., & Kløve, B. (2015). Fully integrated surface–subsurface flow modelling of groundwater–lake interaction in an esker aquifer: Model verification with stable isotopes and airborne thermal imaging. *Journal of Hydrology*, 522, 391-406.
- Barthel, R., & Banzhaf, S. (2016). Groundwater and surface water interaction at the regional-scale—a review with focus on regional integrated models. *Water resources management*, 30(1), 1-32.
- Bixio, A., Gambolati, G., Paniconi, C., Putti, M., Shestopalov, V., Bublías, V., ... & Rudenko, Y. (2002). Modeling groundwater-surface water interactions including effects of morphogenetic depressions in the Chernobyl exclusion zone. *Environmental Geology*, 42(2), 162-177.
- Camporese, M., Paniconi, C., Putti, M., & McDonnell, J. J. (2019). Fill and spill hillslope runoff representation with a Richards equation-based model. *Water Resources Research*, 55(11), 8445-8462.
- Camporese, M., Paniconi, C., Putti, M., & Orlandini, S. (2010). Surface-subsurface flow modeling with path-based runoff routing, boundary condition-based coupling, and assimilation of multisource observation data. *Water Resources Research*, 46(2).
- Cochand, F., Brunner, P., Hunkeler, D., Rössler, O., & Holzkämper, A. (2021). Cross-sphere modelling to evaluate impacts of climate and land management changes on groundwater resources. *Science of The Total Environment*, 798, 148759.
- D'Agata, C., Bocchiola, D., Soncini, A., Maragno, D., Smiraglia, C., & Diolaiuti, G. A. (2018). Recent area and volume loss of Alpine glaciers in the Adda River of Italy and their contribution to hydropower production. *Cold Regions Science and Technology*, 148, 172-184.
- De Schepper, G., Therrien, R., Refsgaard, J. C., He, X., Kjaergaard, C., & Iversen, B. V. (2017). Simulating seasonal variations of tile drainage discharge in an agricultural catchment. *Water Resources Research*, 53(5), 3896-3920.
- Diersch, H. J. G. (2013). *FEFLOW: finite element modeling of flow, mass and heat transport in porous and fractured media*. Springer Science & Business Media.

Doherty, J. E., & Hunt, R. J. (2010). Approaches to highly parameterized inversion: a guide to using PEST for groundwater-model calibration (Vol. 2010). Reston: US Department of the Interior, US Geological Survey.

Harbaugh, A. W. (2005). MODFLOW-2005, the US Geological Survey modular ground-water model: the ground-water flow process (pp. 6-A16). Reston, VA: US Department of the Interior, US Geological Survey.

Hersbach, H., Bell, B., Berrisford, P., Hirahara, S., Horányi, A., Muñoz-Sabater, J., ... & Thépaut, J. N. (2020). The ERA5 global reanalysis. *Quarterly Journal of the Royal Meteorological Society*, 146(730), 1999-2049.

Leavesley, G. H., Lichty, R. W., Troutman, B. M., & Saindon, L. G. (1983). Precipitation-runoff modeling system: User's manual. *Water-resources investigations report*, 83(4238), 207.

Maxwell, R. M., Putti, M., Meyerhoff, S., Delfs, J. O., Ferguson, I. M., Ivanov, V., ... & Sulis, M. (2014). Surface-subsurface model intercomparison: A first set of benchmark results to diagnose integrated hydrology and feedbacks. *Water resources research*, 50(2), 1531-1549.

McDonald, M. G., & Harbaugh, A. W. (1988). A modular three-dimensional finite-difference ground-water flow model. US Geological Survey.

Nash, J. E., & Sutcliffe, J. V. (1970). River flow forecasting through conceptual models part I—A discussion of principles. *Journal of hydrology*, 10(3), 282-290.

Patro, E. R., De Michele, C., & Avanzi, F. (2018). Future perspectives of run-of-the-river hydropower and the impact of glaciers' shrinkage: The case of Italian Alps. *Applied Energy*, 231, 699-713.

PCRaster, 2008. PCRaster internet site. URL:<http://pcraster.geo.uu.nl>

Schmitz, O., Karssenbergh, D., van Deursen, W. P., & Wesseling, C. G. (2009). Linking external components to a spatio-temporal modelling framework: Coupling MODFLOW and PCRaster. *Environmental Modelling & Software*, 24(9), 1088-1099.

Staudinger, M., Stoelzle, M., Cochand, F., Seibert, J., Weiler, M., & Hunkeler, D. (2019). Your work is my boundary condition!: Challenges and approaches for a closer collaboration between hydrologists and hydrogeologists. *Journal of Hydrology*, 571, 235-243.

Sulis, M., Paniconi, C., Rivard, C., Harvey, R., & Chaumont, D. (2011). Assessment of climate change impacts at the catchment scale with a detailed hydrological model of surface-subsurface interactions and comparison with a land surface model. *Water Resources Research*, 47(1).

van der Linden, P., & Mitchell, J. E. (2009). ENSEMBLES: Climate Change and its Impacts: Summary of research and results from the ENSEMBLES project. Met Office Hadley Centre, FitzRoy Road, Exeter EX1 3PB, UK, 160.

Wagner, T., Themeßl, M., Schüppel, A., Gobiet, A., Stigler, H., & Birk, S. (2017). Impacts of climate change on stream flow and hydro power generation in the Alpine region. *Environmental Earth Sciences*, 76(1), 1-22.

# Chapter 5: Conclusions

## 5.1. Summary of main contributions

An integrated loosely-coupled model of the Valtellina catchment was developed with the aim of testing and developing a modelling strategy for studying the interaction between surface water and groundwater in mountainous alpine regions. Given the limited availability of data in these areas, I developed and adopted different strategies methods for the discretization of the systems and the characterization of the hydrological processes involved.

First, the groundwater system and surface water bodies in the study area were preliminary characterised from available data and previous studies. Subsequently, the heterogeneity of the hydraulic properties was attained by applying geostatistical analysis and numerical inversion methods (PEST). All this resulted in a calibrated groundwater flow model that is able to represent the spatial variability of the relationships between groundwater and surface water. In particular, the important role of tributaries was recognised. Indeed, even when disconnected from the aquifer, their input constitutes a fundamental contribution to the groundwater system of the valley floor. Unfortunately, it is important to note that tributary valleys and their rivers are scarcely monitored.

Then, given the difficulty of acquiring meteorological data and the limited presence of monitoring stations in Alpine terrain, satellite data were used to estimate the different components of the groundwater storage of two hydrologic years. In particular, evapotranspiration and snow water equivalent were estimated with the combined use of Sentinel data, at high spatial and temporal resolution. The results show that the methods based on the satellite data provide consistent and physically realistic values to describe groundwater storage dynamics, with an uncertainty of  $\pm 38\%$ . Furthermore, the estimation of groundwater storage at catchment scale enabled to draw some conclusion on the impact of global warming. In fact, a positive storage occurred only during the snowmelt period whereas the overall storage was negative.

Finally, a loosely-coupled surface water-groundwater flow model was developed on the basis of the results obtained in the previous phases of the study. The modelling strategy involved the iterative use of two models, where the results of the first one provide the of boundary conditions for the second one, and the results of the second allow the calibration of the parameters of the first one. The surface water model for the whole catchment was

implemented in the PCRaster Python language based on the runoff tank system modelling. A transient-state finite-element flow model of the valley floor aquifer was developed for the groundwater system using Feflow 7.2. The comparison with the available data showed different results in the simulation of the time series. The hydrological model was able to reproduce the fluctuations with good efficiency in the prediction and high correlation. On the other hand, the groundwater flow model provided acceptable results being able to represent the aquifer recharge phases and the instantaneous response to meteorological events. Therefore, the calibration of the models confirmed the negative groundwater storage for the hydrological years considered.

Given the applicability of the proposed approach in the simulation of surface water and groundwater regimes and of their interactions, an exploratory application to simulate consequence of climate scenarios was performed. Considering four possible scenarios of variation in the water resources within the next 30 years, steady-state changes in groundwater level were simulated. The results showed groundwater level variations of less than one metre. This information can be useful in management and planning by the integrated water service company.

## 5.2. Perspectives for future research

Based on the results and observations, some future research directions could be explored.

First, it would be useful to deepen the modelling of future scenarios due to climate change. Applying the changes in surface resources also on a daily scale, it would allow to assess how water supplies will change over the course of a hydrological year, evaluating possible shifts in recharge and depletion phases.

Moreover, it would be interesting to apply the proposed framework to investigate the interaction of surface and groundwater resources to other large Alpine catchments. This could allow a better understanding of advantages and limitations of the methods. In particular, this would be relevant for estimating uncertainty, as it would allow a more rigorous comparison of the factors influencing the quality of the spatial and temporal discretization of hydrological processes and environments considered. Test examples could include basins with different geomorphological and geological characteristics.

A further prospect for future research would be to implement the groundwater flow model for the entire basin, not limiting it to the valley floor. In this way, the lateral contribution of groundwater flows from the tributary valleys would be included in the recharge of the floodplain aquifers. Obviously, this would be possible only through the characterization of the heterogeneity and of the rock slopes aquifers of the tributary valleys.

Finally, the modelling of the whole catchment from the point of view of groundwater resources allows a further important research perspective. It would be interesting to convert the loosely-coupled integrated model into a fully-coupled integrated model. In fact, the software used for groundwater flow modelling (FeFlow 7.2) allows the implementation of plugin-ins in the Python programming language to solve external problems and the hydrological model of this thesis could be added.